ELECTRO-MAGNETIC MODELING AND DESIGN OPTIMIZATION OF SYNCHRONOUS RELUCTANCE MACHINES AND SINGLE-PHASE INDUCTION MACHINES

A Dissertation
Presented to
The Academic Faculty

by

Hang Shao

In Partial Fulfillment
of the Requirements for the Degree
Doctor of Philosophy in the
School of Electrical and Computer Engineering

Georgia Institute of Technology
December 2019

ELECTRO-MAGNETIC MODELING AND DESIGN OPTIMIZATION OF SYNCHRONOUS RELUCTANCE MACHINES AND SINGLE-PHASE INDUCTION MACHINES

Approved by:

Dr. Thomas G. Habetler, Advisor
School of Electrical and Computer Engineering
Georgia Institute of Technology

Dr. J. Rhett Mayor
The George W. Woodruff School of Mechanical Engineering
Georgia Institute of Technology

Dr. Daniel Molzahn
School of Electrical and Computer Engineering
Georgia Institute of Technology

Dr. Lijun He
GE Global Research
General Electric Company (GE)

Dr. Maryam Saeedifard
School of Electrical and Computer Engineering
Georgia Institute of Technology

Date Approved: 07/29/2019

To

my father, Yuzhen Shao,

my mother, Guilian Dong,

for their support and love.

ACKNOWLEDGEMENTS

The doctoral study in the past years is a precious and unforgettable experience in my life, during which lots of inspiration and encouragement have been offered to me toward my research, leading to the completion of this dissertation.

First of all, I would like to extend my sincerest gratitude to my advisor, Dr. Thomas G. Habetler for his generous guidance. Taking charge of the big picture and the direction of my research, he always has confidence in me and fully trusts me on completing the detailed tasks, which provides me abundant chances and freedom to put my own steps on the undiscovered lands, learning and gaining experience in the meantime. The ability to conduct research is the most invaluable skill I gained from my doctoral study, and I would give all the credit to Dr. Habetler for the trust and instructions he provided.

I would also like to express my thanks to Dr. Maryam Saeedifard, Dr. Daniel K. Molzahn, Dr. J. Rhett Mayor and Dr. Lijun He for serving as the committee members for my final defense. The advice they provided on my research definitely broadens my horizon and perfects this dissertation.

I am indebted to Dr. Lukas Graber, who served on my Ph.D. proposal committee. His insightful suggestions on my research work gave me the ideas to improve my dissertation.

I would like to specially thank Dr. J. Rhett Mayor and Dr. Andrew Semidey for the hands-on experience I gained during the collaboration with them. Such experience in the

motor industry helps me find the connections between my knowledge and the industrial applications, and I have learned a lot through the teamwork.

I have always been grateful to Dr. Joyelle J. Harris, Dr. David R. Hertling and Dr. Benjamin Klein for their support.

It was delightful to work with many exceptional colleagues in my research group. I would like to thank Dr. Nan Liu, Dr. Hao Chen, Dr. Chen Jiang, Dr. Heng Yang for their advice as senior Ph.D. students at the start of my doctoral study. I would also like to pay my gratitude to Dr. Chanyeop Park, Dr. Liyao Wu, Dr. Qichen Yang, Dr. Sufei Li, Dr. Shen Zhang, Dr. Cheng Gong, Genyi Luo, Jingfan Sun, Xiangyu Han, Qianxue Xia, Chiyang Zhong, Boqi Xie, Jiahao Xie, Kaiyu Liu, Liran Zheng, Zheng An, Xiwei Zheng, Chunmeng Xu and Jia Wei for the support and friendship. I am thankful to Morteza Rezaee, Mahmoud Mehrabankhomartash and Abdulaziz M. Qwbaiban for the friendly help they provided. I owe my greatest thanks to Dr. Sufei Li, whose help tremendously expedited my research.

All the other friends and acquaintances of mine are important to me during my growth in the past four years. They supported and encouraged me to overcome the difficulties and made me who I am.

Most of all, I owe my gratitude to my parents for their tremendous love throughout my life. Though living far from them now, I consider my continuous hard work as my act of love toward them, and I hope I can make them proud by earning the Ph.D. degree.

TABLE OF CONTENTS

LIST OF TABLES

LIST OF FIGURES

SUMMARY

With high efficiency, low noise and independence of fossil fuel, electric machines are widely adopted as energy conversion devices, consuming a majority amount of energy available from the power grid, and are widely applied in the industrial systems and house appliances. The synchronous reluctance machines (SynRMs) have attracted a significant amount of attention in the recent decades among other types of electric machines due to its independence from permanent magnets (PMs). The PM-free rotor brings down the cost of the SynRM, while a normal drive designed for use with synchronous machines can be utilized. The single-phase induction machines (IMs), on the other hand, have long been applied in household appliances due to their low cost and ability to work under the one-phase power supply. Consequently, finding the optimal designs of the two types of machines is of great importance for saving energy, reducing the production costs, as well as improving the machine performance.

The objective of this dissertation is to develop the analytical electro-magnetic (EM) models for SynRMs and single-phase IMs, so as to generate the optimal designs to improve their performance. For the SynRM, a universal analytical model is proposed based on the Maxwell's equations and the conformal mapping technique. The saturation effect in the iron region is modeled with the help of the magnetic equivalent circuit (MEC) model. For the single-phase IM, the equivalent circuit model is adopted in order to analyze the machine performance from the design parameters. The analytical models are able to calculate the machine performance indices (PIs) from the machine design parameters with significantly reduced time consumption compared with the finite element analysis (FEA) method. Such

time efficiency is desired during the design optimization process, when hundreds or thousands of designs need to be evaluated during the iterations.

The evolutionary algorithms such as particle swarm optimization (PSO) and differential evolution (DE) are adopted as optimizers for finding the optimal machine designs based on the analytical models. Multi-objective design optimization is conducted on both the SynRM design problem, where the algorithms converge to the Pareto front, and the single-phase IM design problem, where a weighted-sum of the PIs is chosen as the objective function. The PIs of the solved optimal designs are validated through FEA simulations, proving the accuracy of the analytical models and the effectiveness of the proposed design optimization method.

CHAPTER 1. INTRODUCTION

1.1 Background

With high efficiency, low noise and independence of fossil fuel, electric machines are widely adopted as energy conversion devices, consuming a majority amount of energy available from the power grid, and are widely applied in transportation systems, robots, house appliances and cooling systems [1]. Born about 200 years ago, electric machines have experienced tremendous development in the recent 30-40 years, yielding higher efficiency, higher torque density and lower costs, as well as faster and more accurate control techniques [2].

1.1.1 Development of Electrical Machine Technology

Researchers and engineers have achieved advances in electrical machine technology via majorly the following two paths: better control methods and more advanced designs. Field-oriented control [3] and direct torque control [4] are currently the most widely adopted control techniques for AC machines. With the help of modern power electronics, PI controllers, as well as accurate sensors, these two control methods are generally able to provide accurate and fast control on torque output, speed and position of common AC machines. Sensorless control [5] is another popular research area in the literature, due to its independence from sensors which reduces cost and improves reliability. For the high-speed machines, special control techniques [6-8] are required due to the mechanical limit of the sensors. In addition, optimal control methods are proposed with the objective of maximizing the torque density [9], reducing the torque ripple [10],

improving the efficiency [11], etc., with the purpose of improving one specific performance index of the machine.

New designs have been emerging rapidly since the birth of electrical machines. Design innovations include invention of new types of machines, new topologies based on the existing type, as well as application of new materials. Among all the types of machines, AC induction machines and synchronous machines are currently the most widely applied ones [2], whose design optimization on topologies are extensively discussed. Better materials are meanwhile available thanks to the development of material science and production techniques, bringing us the cold-rolled electrical steel, permendur alloy [12] such as Hiperco 50, rare-earth magnet [13] such as NdFeB, as well as super-conductors [14]. Such new materials provide lower iron loss, higher saturation point, more energy density and lower copper loss, thus are coveted by the machine design industry when the product to be designed is less cost-sensitive and aims more at better performance.

1.1.2 Common Types of Electrical Machines and Their Applications

The most widely applied machines in the industry nowadays can be roughly categorized into the following types: DC machines, induction machines (IMs), synchronous machines and switched reluctance machines (SRMs).

A DC machine can be excited by either permanent magnets (PMs) or field windings. The magnetic field produced is orthogonal with the field generated by the armature winding, making the control of DC machines much more benign. Furthermore, the DC machine has a linear torque-speed curve, and the torque does not drop too much when the speed increases, which is a major advantage in most industrial applications. DC

machines are adopted widely in paper mills, steel mills and trains, where sufficient starting torque and accurate control are desired. However, the existence of brushes limits the speed and lifespan of the DC machine, as well as increasing its mechanical complexity, leading to reduced reliability. Consequently, brushless DC machines are invented in order to get rid of the brushes. The brushless DC machine relies on power electronics appliances to provide the commutation, thus replaces the brush and commutator in a traditional DC machine. Such technique makes the machine more similar to a synchronous machine fed by a DC line through a multi-phase inverter, resulting in the complexity of control, and introduces other problems such as torque ripple and harmonics [15].

The induction machine may have either a caged rotor or a wound rotor with the windings shorted. The squirrel-cage induction machine is the most produced type of machine in industry due to its low cost and easiness of manufacturing. Common induction machines can be either three-phase, mostly applied in industry, or single-phase, ubiquitous in household appliances such as fans. The wound-rotor induction machine can also be designed as a generator, whose stator and rotor are both fed, thus named doubly fed induction generator, and are generally applied on wind turbines [16]. Control of induction machines, however, can be tricky due to the coupling of stator and rotor windings. Field-oriented control [17] or direct torque control [4] is usually adopted to achieve accurate control of induction machines, requiring reliable power electronics devices and inverters.

The most common type of synchronous machine is the permanent magnet synchronous machine (PMSM). Rare-earth permanent magnet materials such as NdFeB provide high energy density, which is desired in transportation applications such as electric vehicles [18]. Such materials are subject to high cost, making the permanent magnet-free

version of synchronous machine stand out. The synchronous reluctance machine (SynRM) is the most common type of magnet-free synchronous machine. The stator of an induction machine can be directly applied to the SynRM, while the SynRM rotor needs to be punctiliously optimized and engineered in order to achieve better performance such as higher torque density and lower torque ripple [19]. The SynRM is capable of achieving higher efficiency than the induction machine since there is no copper loss on the rotor, while the torque density of the SynRM is not as high as synchronous machines with permanent magnets. As a consequence, small volumes of permanent magnets can be added in the rotor flux barriers of the SynRM, making it a permanent magnet-assisted synchronous reluctance machine, which lies in the middle of SynRM and PMSM in both cost and torque density.

The switched reluctance machine (SRM) [20] is another prevalent type of magnet-free machine. Advantages of the SRM include rigid structure, high reliability, fast dynamic response and low cost [21-24]. Disadvantages such as high noise level, large torque ripple are all substantial and cannot be ignored. Dependence on a specifically designed drive further limits the application of the SRMs.

1.1.3 Design Procedures of Electrical Machines

A typical machine design process includes the following steps [25]: electrical design, magnetic design, thermal design and mechanical design.

The rated voltage, frequency, and number of phases are typically specified in the machine design requirements for the electrical design. The designer needs to choose the proper values of number of poles and slots, winding layouts, as well wire gauges.

The magnetic design is usually conducted along with the electrical design, since the magnetizing current in the winding creates magnetic field in the machine. Magnetic equivalent circuit (MEC) model is a handy tool for electro-magnetic modeling, while the finite element analysis (FEA) provides a more accurate solution. Flux densities in the iron parts and air-gap should be specified during magnetic design by choosing the proper geometries of rotor and stator, as well as the air-gap length.

A proper thermal design is crucial since cooling of the machine affects its performance and lifespan. Better cooling can be achieved by optimizing geometry of the machine so that air circulation can be improved. Water cooling or oil cooling techniques can also be applied to obtain outstanding performance.

The mechanical stress field of the machine should also be analyzed during the design procedure in order to ensure the mechanical stability and robustness. A better mechanical design can also lead to reduced noise and vibration, which is desired in most cases. Proper bearings should be chosen according to the design requirements and working conditions of the machine.

1.1.4 Design Optimization of Electrical Machines

With all the electro-magnetic, thermal and mechanical problems included, designing a new machine from scratch takes a considerable amount of time. Modern designers usually develop machines based on previous designs by making adjustments and optimizations according to specific design requirements. A novice designer may utilize the FEA tools to conduct design optimization, which is generally intuitive and time-consuming. Optimizing the design parameters based on an analytical model is capable of saving large

amount of time and is able to provide a good starting point for further FEA analysis, which fine-tunes the parameters for a more optimized design.

1.2 Problem Statement

As stated in the previous section, design optimization of electrical machines is commonly conducted in order to obtain a desired design. This research focuses on developing general optimization methods for synchronous reluctance machines (SynRMs) and single-phase induction machines (IMs), since the SynRM is proved to have the potential of replacing the mass-produced three-phase induction machine [19] with the advantage of higher efficiency, and the single-phase IM is the mostly produced type of machine and is commonly found in major house appliances.

The objective of the proposed research is to develop the analytical electro-magnetic (EM) models for SynRMs and single-phase IMs, so as to generate the optimal designs to improve their performances. For the SynRM, a universal analytical model is proposed based on Maxwell's equations and conformal mapping. Saturation effect is modeled with the help of the MEC model. For the single-phase IM, the equivalent circuit model is adopted in order to analyze the machine performance from the design parameters.

Evolutionary algorithms are used to conduct the multi-objective optimization (MOO) for the SynRM and single-phase IM. The optimal designs show improved performance compared with the original designs, and the time consumed is acceptable due to the time efficiency of the analytical model.

The ultimate goal of this research is to create a computationally efficient design tool that has the ability to rapidly locate an optimal design candidate which satisfies the design specifications and objectives. Once the optimal design candidate is located, a final design can be easily completed by further refinement using the commercially available FEA software.

1.3 Dissertation Outline

The dissertation is organized as follows:

Chapter 2 presents a comprehensive review of the literature on the modeling and design optimization of SynRMs and single-phase induction machines.

Chapter 3 introduces a generalized and time-efficient EM model that solves the performance indices of the SynRM such as torque, efficiency and weight, which are the cornerstones of a fast optimization process.

Chapter 4 synthesizes the proposed EM model with evolutionary optimization algorithms so as to develop MOO of the SynRM, and generates the optimal designs under different design objectives.

Chapter 5 presents the equivalent circuit model of the single-phase induction machine. MOO is developed based on the model, yielding better performance compared with the original design.

Chapter 6 summarizes the conclusions, the contributions, and the recommendations for future work.

CHAPTER 2. LITERATURE REVIEW

This chapter presents a comprehensive literature survey to summarize the electromagnetic (EM) modeling and design optimization methods of synchronous reluctance machines (SynRMs) and single-phase induction machines (IMs). For the SynRM, existing modeling methods are primarily based on either Finite Element Analysis (FEA), which is time consuming, or the magnetic equivalent circuit (MEC) models, which are subject to uncertainty. For the single-phase IM, existing design methods require a considerable number of heuristic rules established decades ago, which are mostly based on past experience and are not scientific. The review of literature leads to a conclusion that novel modeling methods and design approaches are essential for modern optimal designs of SynRMs and single-phase induction machines.

2.1 Electromagnetic Modeling of Synchronous Reluctance Machines

A proper EM model of the SynRM is crucial during the optimization process. The EM model should equip the designer with abilities of accurately calculating the machine performance indices, such as torque, efficiency and weight, in a short period of time from the machine design parameters, such as geometrical parameters and electrical parameters. It is thus obvious that the accuracy and rapidity of the EM model are both desired, and in most cases a compromise has to be made between the two qualities.

2.1.1 Numerical Methods

Finite element analysis is the most popular numerical analysis tool, since it offers trustworthy results for EM fields within SynRMs with complex geometries and nonlinear

properties. The FEA is based on subdividing the entire solution domain into small parts called finite elements. Each element is modeled separately, after which the equations are assembled, and the solutions are approximated. The subdivision creates small solving areas, which is substantial for accurately solving the EM field within the SynRM, since the EM field variation is subject to impact of various aspects such as saturation and anisotropy of the material. Furthermore, size of the meshes can be adjusted based on the complexity of the solution domain. A fine mesh is necessary for the areas with complicated geometrical shapes or rapid field changes, while a rough mesh is adequate for the less complicated areas in order to reduce the complexity. Consequently, the FEA generally yields accurate EM field solutions that match well with experimental results. Figure 2.1 [26] indicates a typical mesh when analyzing the SynRM with FEA tool. It can be observed that denser meshes are applied at the air-gap region, since accurate calculation of machine performance requires precise and trustworthy solutions of the air-gap magnetic field. Fine meshes are also operated at the tips of the teeth, due to the complexity of the saturation level at these parts. Since saturation is generally not severe in rotor and stator yokes, sparser meshes are observed in these areas of the machine.

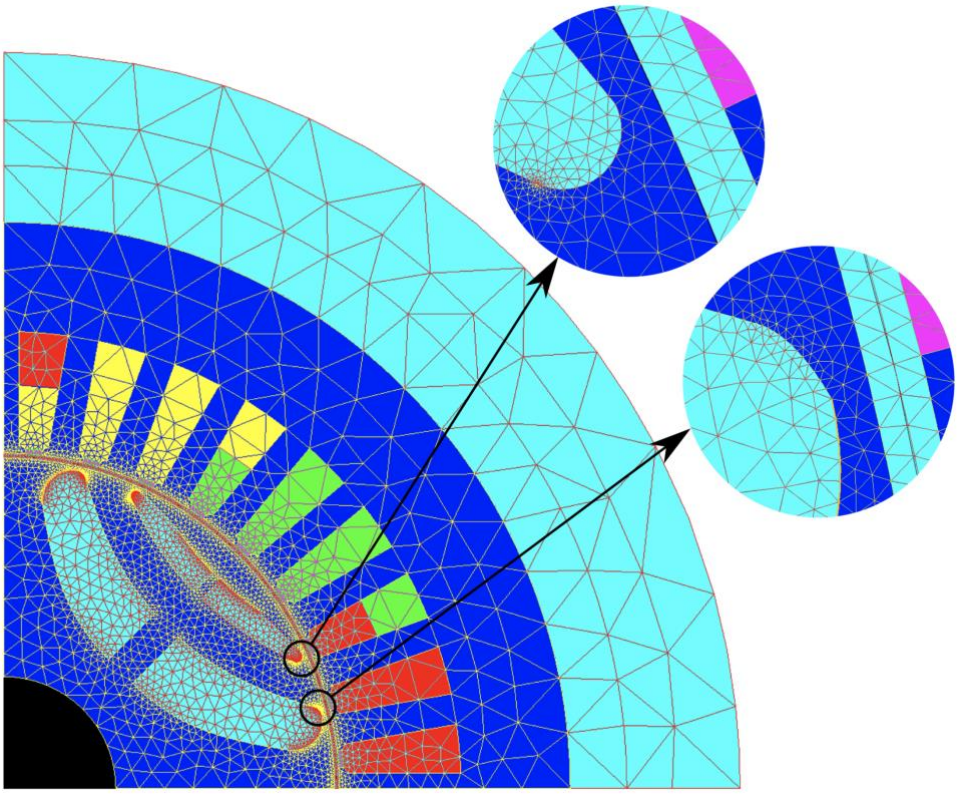

Figure 2.1 Meshing of the SynRM [26].

Researchers have been analyzing various SynRM performance indices (PIs) including efficiency, torque density, power factor, torque ripple, weight and volume with the help of the FEA tool. Reference [26] adopts the FEA method in order to analyze rotor iron losses of the SynRM. The interaction between the rotor iron losses and several machine geometrical parameters is discussed. The rotor shape and the number of flux barriers for a 15kW SynRM are optimized to achieve the highest efficiency in [27]. Coupled FEA and Preisach modeling is used in [28] in order to evaluate the efficiency of a SynRM under the effect of saturation and hysteresis loss. The FEA tool is also utilized in [29] in order to study the effects of the rotor design parameters of a permanent-magnet-assisted SynRM.

The FEA is also an efficient tool in research with the purpose of improving the torque density and power factor of the SynRM. The p-pair, two barrier rotor is focused in [30], and the optimal distribution of air and iron for the maximum torque is given with the help of FEA approach. Saturation effects and other nonlinearities are also included by FEA simulations in order to determine the best rotor design parameters for better torque density performance. In [31], the torque density is optimized by adjusting the rotor geometric design function from an existing machine or a preliminary design. Reference [32] analyzes the effect of the number of flux barriers in order to achieve maximum saliency ratio, and reveals the optimum ratio of flux guide/flux barrier thicknesses. In addition, the appropriate value of saliency ratio is investigated to maintain a power factor competitive with an induction machine [33].

Approaches for reducing the torque ripple of the SynRM have been extensively proposed, with the help of FEA tools. Asymmetric flux barrier arrangement is adopted in [34], so that the relative positions between the outer edges of the flux barriers and the stator teeth do not correspond. The effect of the torque-ripple reduction is then examined by FEA, showing satisfying results. Reference [35] examines the relation between the torque ripple and the width of the slit in stator slots using FEA, and it is indicated the torque ripple is minimized when there is no slit. Geometry of rotor flux barrier is chosen in [36, 37] so as to reduce torque ripple, and it is verified that the position of the outer edges of the flux barriers have a large impact on the torque ripple.

The FEA tool is arguably the most accurate modeling tool for analyzing the EM field of electrical machines. One fatal and perhaps the only disadvantage, is the computational complexity and time consumption, which limits the FEA as a modeling and

verification tool rather than a design tool under the limited computing capability of current PCs and servers used by most designers. Such complexity originates from the effort of solving the equations from each individual finite element, and is further increased when sophisticated meshes are made due to the need of a better resolution in the final solution. Three-dimensional (3D) problems [38, 39] complicates the FEA calculation to a higher level with the addition of a new dimension, which requires larger numbers of 3D meshes in either tetrahedrons or triangular prisms. Consequently, great effort has been made in literature and industry in order to reduce the computational complexity of the FEA.

The domain decomposition method is one of the popular efficient FEA techniques. Such method is based on decomposing the original solution area into several sub-domains, and solves each sub-domains simultaneously by taking advantage of the parallel computing method. Reference [40] proposes the dual-primal finite-element tearing and interconnecting method that improves the efficiency of 3D FEA for solving EM field in electric machines. Such method is based on the sub-domain method while adopting higher order hierarchical basis functions in order to solve the low-frequency breakdown problem. Similarly, the numerous time steps in a time-stepped FEA can be grouped in several domains and be computed concurrently, thus forming the time decomposition method [41]. Both a steady-state simulation of a periodic physical problem and a general simulation of a non-periodic transient model are introduced in [41], so as to illustrate the effectiveness of the time decomposition method. Combining the FEA method with analytical models is another idea for conducting fast simulations. Reference [42] proposes the finite-element surrogate model that employs the FEA for only limited number of times with the purpose

of calculating the preliminary values such as the magnetic vector potential in the coils, while the machine performance is then calculated from the analytical model.

2.1.2 Magnetic Equivalent Circuit Models

Pure analytical models outweigh the FEA method in terms of computational efficiency thanks to the fewer numbers of equations involved in the model. The accuracy of the results, however, is usually on the lower end of the spectrum. The magnetic equivalent circuit (MEC) model has been a popular analytical model among machine designers for decades due to its similarity with electrical circuits, which makes the modelling process intuitive. The MEC models the magnetic field within the machine in a similar way as the electrical circuit models the electrical field within the conductors. The air and iron region in the machine are segmented arbitrarily and modeled as reluctance in the MEC, similar to the resistance in electric circuits. The amp-turns produced by the stator windings in a SynRM is modeled as magnetomotive force (MMF) in the MEC, similar to the voltage source or electromotive force (EMF) in an electric circuit. The similar components in the MEC and the electrical circuit are presented for comparison in Table 2.1.

Table 2.1 Comparison of the MEC and Electrical Circuit Elements.

MEC Element	Electrical Circuit Element
MMF: F (Amp-turns)	EMF: e (V)
Flux: Φ (Wb)	Current: i (A)
Reluctance: R_m (H^{-1})	Resistance: R (Ω)

Table 2.1 continued

Magnetic potential drop: $Hl = \Phi R_m$	Electric potential drop: $u = iR$
Ohm's Law: $\Phi = \frac{F}{R_m}$	Ohm's Law: $i = \frac{u}{R}$

The MEC model schematic for a two-pole SynRM is shown in Figure 2.2. It can be observed that the SynRM is divided arbitrarily into eight regions, making it easier to be represented by a circuit model. The magnetic fluxes are assumed to flow at the certain directions, thus forming a magnetic circuit. The MMF generated by stator windings are modeled as MMF sources in the MEC, while the air regions are represented by reluctances. Reluctances of the iron parts are neglected in this model since infinite permeability is assumed on the iron.

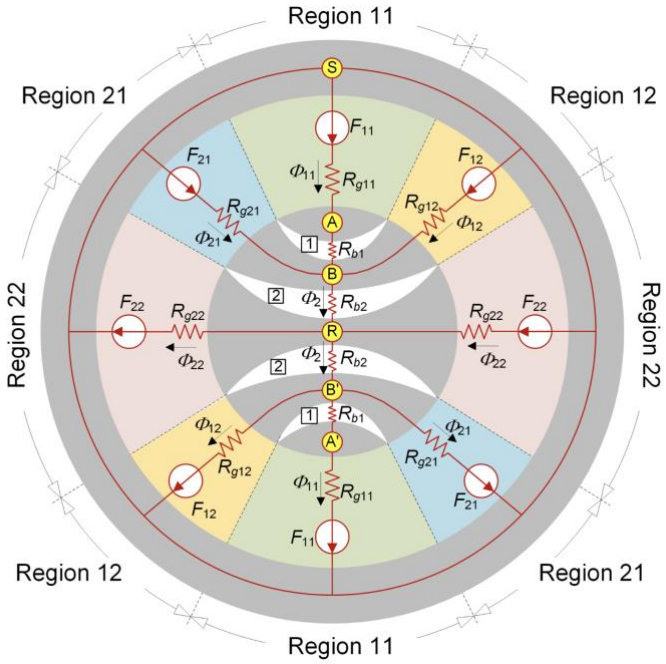

Figure 2.2 MEC model for a two-pole SynRM [43].

The magnetic circuit can then be analyzed with similar approach as analyzing the electrical circuits, yielding calculated results of the magnetic potentials on the MEC nodes and the flux values in the MEC branches. The flux densities in each section of the SynRM, which is crucial for calculating the machine performance, can be derived directly from the magnetic flux values.

The MEC model has been widely adopted by researchers in order to roughly analyze SynRMs in a dramatically faster way than the more accurate FEA approach. A standard MEC model is applied and simplified in [44] to relate the machine design parameters to its performance indices. References [45] and [46] applied an MEC model to analyze performance of the SynRM with single and multiple flux barriers per pole when eccentricity happens. Conformal mapping technique is applied in [43, 47, 48] in order to provide an accurate calculation of the magnetic reluctance in flux barriers of SynRM due to their complex geometries, yielding convincing results of the calculated air-gap flux densities when compared with FEA simulation.

While most MEC models proposed for SynRMs are built as linear circuits without considering the saturation effect, there are some recent works focused on building a nonlinear MEC based on B-H curves of rotor and stator steel. Local saturation factors are defined so as to adjust the flux-density distribution in [49], where slot effects are also taken into account. Such model is then improved in [50] with rotor eccentricity considered. Relations of both average and torque harmonics to the rotor geometry are derived in [51], where the maps showing the torque harmonics as a function of the rotor barrier angles are also derived.

2.1.3 Models Based on Maxwell's Equations

It can be discovered from the previous discussion that the MEC model depends on assumption of the flux paths, leading to inevitable uncertainty and inaccuracy. Figure 2.3 [52] is an example of the assumed flux distribution in the air-gap of a permanent-magnet synchronous machine (PMSM). The arrows are mimicking the flux distribution, but may never match with the real case. Similar problem can also be observed in Figure 2.2, where all flux paths are assumed to flow in radial directions, while the circumferential components are neglected.

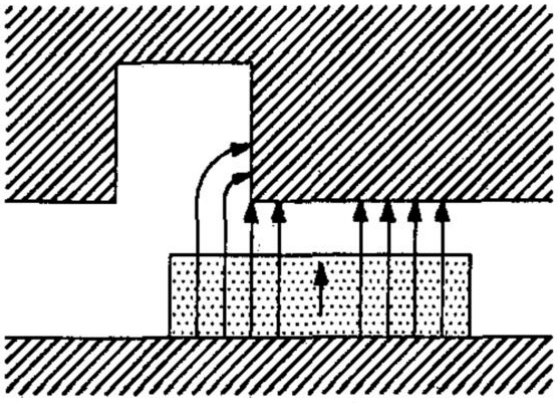

Figure 2.3 Assumed flux distribution in the air-gap of a PMSM [52].

Therefore, analytical model based on Maxwell's equations is proposed, since the equations are universal for EM field problems, and are capable of providing EM field solutions at any spatial positions. Drawback of the Maxwell's equations majorly lies in their complication to solve, which require complicated mathematical derivations and skills. Nevertheless, such complication does not affect the computational speed of such models, as they are also analytical models described by closed-form expressions, and are fast to be solved by normal desktop computers.

Maxwell's equations have been well adopted for modelling electrical machines with relatively simple geometries, such as PMSMs and switched reluctance machines (SRMs). Reference [53] is one of the earliest works adopting Maxwell's equations in machine analysis. It utilizes the concepts of permeance and MMF, and involves the solution of the Poissonian field in the airgap/magnet region in order to taking slot effect into account. The cogging torque in surface PM machines is analyzed by utilizing conformal mapping method as well as Maxwell's equations in [54], where the principle of complex relative air-gap permeance derived from conformal transformation of the slot geometry is proposed. Reference [55] applied similar approaches, but focused more on calculation of the magnetic field distribution in the slotted air-gap of PMSMs, while [56] calculates the electromagnetic torque from the Maxwell stress tensor.

Researchers have also tried to adopt Maxwell's equations as a more accurate substitute for MEC models in SRM analysis and optimization applications. Radun's two sequential papers [57, 58] present analytical equations to calculate the inductances at both unaligned position and the positions when the stator and rotor poles overlap. Unsaturated phase inductance of 4/2 and 6/4 SRMs are accurately calculated in [59-61] by adopting partial differential equations and magnetic potentials.

However, modelling with Maxwell's equations in SynRMs is more challenging because of the complicated structure of the SynRM rotor. Reference [43, 47, 48] apply conformal mapping and solve a basic potential equation to obtain the magnetic field in flux barriers, but then calculate the reluctances of flux barriers and build an MEC model, rather than keep solving the magnetic field distribution in the machine with Maxwell's equations.

Overall, modelling SynRMs with Maxwell's equations is of great importance to providing an accurate field solution, while still mostly uncultivated in the existing works.

2.2 Electromagnetic Modeling of Single-Phase Induction Machines

Requirements for the EM model of the single-phase IMs is similar to that for the SynRMs. The desired model should solve fast, without sacrificing too much accuracy. FEA tools and analytical models are the predominant approaches in the literature.

2.2.1 FEA Modeling of Single-Phase Induction Machines

The FEA mesh of a typical single-phase IM is shown in Figure 2.4 [62]. Similar to the meshes for the SynRM shown in Figure 2.1, tinier meshes are observed at the air-gap region and tooth tips, while coarse meshes are applied at stator and rotor yokes.

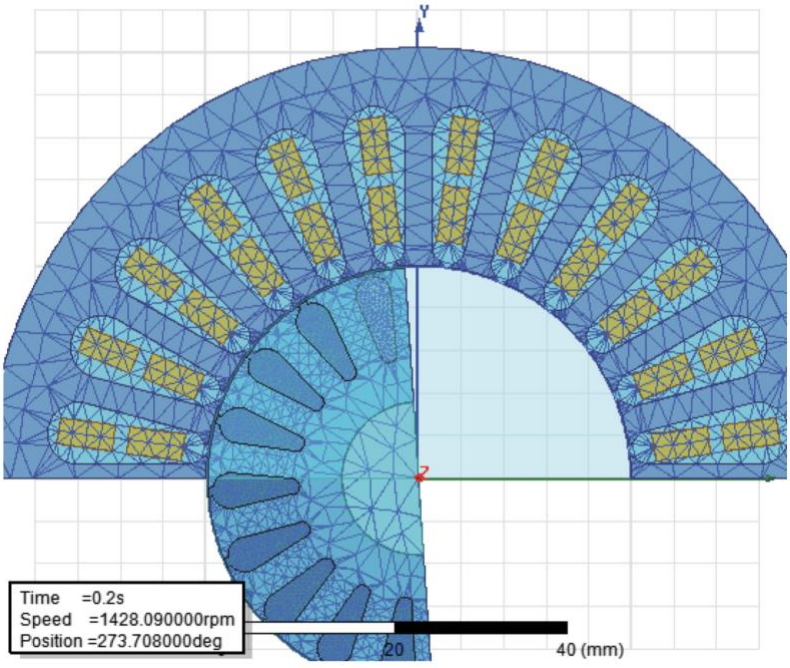

Figure 2.4 FEA mesh of a typical single-phase IM [62].

Due to the accuracy of the FEA method and the well-developed FEA software, the FEA tool is popular among modern designers aiming at improving the performance of the single-phase IMs. With the help of FEA, efficiency of the single-phase IM is optimized in the design in [63] by analyzing the impact of the design parameters such as stator diameter, air-gap length, lamination thickness, steel type and the run capacitor value. A copper-bar single-phase IM is designed in [64] using the Opera 2D software. It is then verified that copper rotor bars increase the machine efficiency and conduct a lower value of flux density in the machine. Impact of the slot opening on the performance of a single-phase IM is analyzed in [65] based on the time-stepping FEA and the Maxwell stress tensor. It concludes that controlling the slot openings will lead to higher efficiency of the single-phase IM. Reference [66] trains a neural network based on data generated from numerous FEA simulation of the single-phase IM. The neural network is verified to be capable of estimating the efficiency of the single-phase IM from the desired output power and the number of stator/rotor slots.

Due to the inherent computational complexity of the FEA method, the time-efficiency of the FEA is always desired to be improved. This is usually implemented by combining the FEA analysis with the equivalent circuit model of the single-phase IM. Parameters of the equivalent circuit is calculated from the voltage source complex FEA in the method proposed in [67]. The machine performance is then derived from the equivalent circuit, showing accurate results compared with tested data. Similar technique is applied in [68], where a different type of equivalent circuit is coupled with FEA simulation in order to reduce the computational complexity of the FEA. However, the simulation speed of such

combined model is still outweighed by the analytical models, introduced in the following section.

2.2.2 Analytical Model of Single-Phase Induction Machines

The equivalent circuit model of the single-phase IM was proposed decades ago. Similar to the equivalent circuit of the three-phase IM, the circuit model conducts various assumptions, making it not as accurate as the FEA analysis. However, the parameters in the equivalent circuit are calculated from machine design parameters based on physical laws, thus physically makes more sense than the FEA-based numerical calculation. Typical equivalent circuits of the three-phase IM and the main winding of the single-phase IM are shown in Figure 2.5(a) [69] and Figure 2.5(b) [70] respectively for comparison.

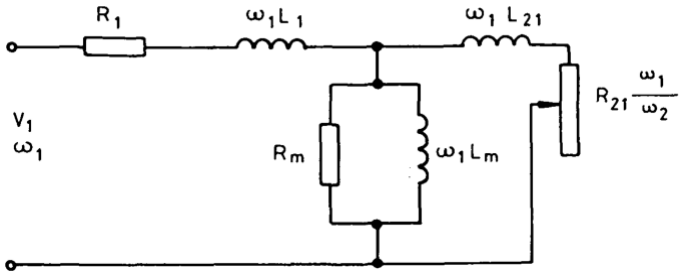

(a)

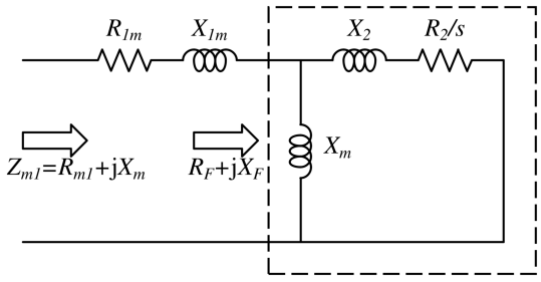

(b)

Figure 2.5 (a) Equivalent circuit of the three-phase IM [69]; (b) Equivalent circuit of the main winding of the single-phase IM [70].

Various design optimizations based on the single-phase IM equivalent circuit model have been conducted in the literature with the purpose of improving different performance indices. The impact of negative sequence magnetic field on machine efficiency is investigated in [71], where a new design is proposed with a special stator winding layout. With the help of the equivalent circuit model, such innovative design is derived scientifically based on mathematical calculations, instead of being intuitively designed based on trials and errors through FEA. The placement of the run capacitor is discussed in [72], showing that placing the run capacitor on the main winding and on the auxiliary winding will make different impacts on machine performance. Reference [73] proposes the 4-8 pole common winding for the single-phase IM. Such winding allows two different pole numbers on a same machine by simply reconnecting the windings. Both the starting winding and the starting capacitor are optimized in [70], with the goal of optimizing the starting performance. The optimal design of a single-phase IM with two-value capacitor is proposed in [62], where important design parameters such as air-gap length, frame size as well as number of rotor/stator slots are all taken into account. Improved efficiency and torque are achieved on a single-phase IM in [74], which focuses on optimal design of the stator/rotor slots, stator winding, as well as choosing the proper core material. Design of a concentrated winding single-phase IM is improved in [75] by focusing on optimizing the skew of rotor slots and stator winding turns. Commercial design software based on the equivalent circuit model, such as Ansys Maxwell Rmxprt, is also available for single-phase IM design. Reference [76] introduces the design optimization of a single-phase IM based on the Rmxprt package in the Ansys Maxwell software.

Additionally, there is also research focusing mainly on the equivalent circuit model itself. Three different methods are introduced and compared in [77] with the goal of determining the parameters in the equivalent circuit model of the single-phase IM. Such methods are clear paths for building the equivalent circuit model, making analytical analysis of the single-phase RM more approachable.

Generally, design optimization of the single-phase IM requires a fast and accurate analytical equivalent circuit model, while the FEA simulation is usually conducted for verification and refinement purposes.

2.3 Design Optimization Algorithms

Due to the non-linear characteristic and complicated geometries of electric machines, there is no simple expression that is able to link the machine design parameters with machine performance while maintaining accuracy of the model. Therefore, evolutionary algorithms have been widely applied for optimal design problems of both SynRMs and single-phase IMs based on either the FEA model or the much faster analytical model.

2.3.1 Design Optimization of Synchronous Reluctance Machines

Optimal design of the SynRM has been studied extensively in the literature. Most of the research focuses on improving the SynRM performance with the help of the FEA method. The average torque of the SynRM is improved by optimizing the rotor design, as conducted in [78], where genetic algorithm (GA) is applied based on FEA simulation of the torque performance. Reference [79] focuses on reducing the torque ripple of the

SynRMs with four flux barriers per pole, and presented three different scenarios of ripples. Torque ripple reduction is also accomplished in [80] by optimizing the rotor geometry based on the frequency domain FEA method. The average torque of a high speed solid rotor SynRM is maximized in [81], where a simple cyclic algorithm is coupled with the FEA simulation in order to reiterate the performance calculation under different rotor designs. Average torque improvement is achieved on a SynRM by increasing the saliency ratio of the rotor, as presented in [82]. A single-phase SynRM suitable for household appliances is investigated in [83], where machine efficiency is improved by optimizing the rotor design and creating a higher saliency ratio.

While the achievements listed above mainly focus on optimizing only one performance index of the SynRM, such as torque, torque ripple and efficiency, multi-objective optimization (MOO) is also conducted in the literature, creating the optimal SynRM designs that have good performance in various aspects. The objective function of the MOO can be constructed from the weighted sum of the interested performance indices. By choosing the proper weight factors, designers have the freedom to emphasize one or two most important performance indices without losing control of the other indices. The weighted sum is applied as the objective function in [84], which takes the average torque, torque ripple and power factor into account. The Python-based optimization suite, PyOpt, is then applied to solve the optimization problem. Apart from the weighted-sum technique, the Pareto front is also widely adopted to evaluate the optimal designs generated in the MOO. The Pareto front is generally a multi-dimensional region, whose dimension equals to the number of performance indices to be optimized. For each design in the Pareto front, no performance index can be further improved without weakening one or more of the other

indices. A three-dimensional Pareto front is marked by the ellipse in Figure 2.6 [85],where each individual dot represents one SynRM design. The torque ripple, the changed sign (CS) power factor, and the 'badness' calculated from the torque and total loss of the SynRM are the three performance indices. All designs in the Pareto front can be considered as optimal, while only one or two are chosen for further refinement in a typical design optimization process. An improved computationally efficient FEA method is applied in [85] in order to calculate the SynRM performance. The differential evolution (DE) algorithm is modified to better conduct the MOO for the SynRM [85].

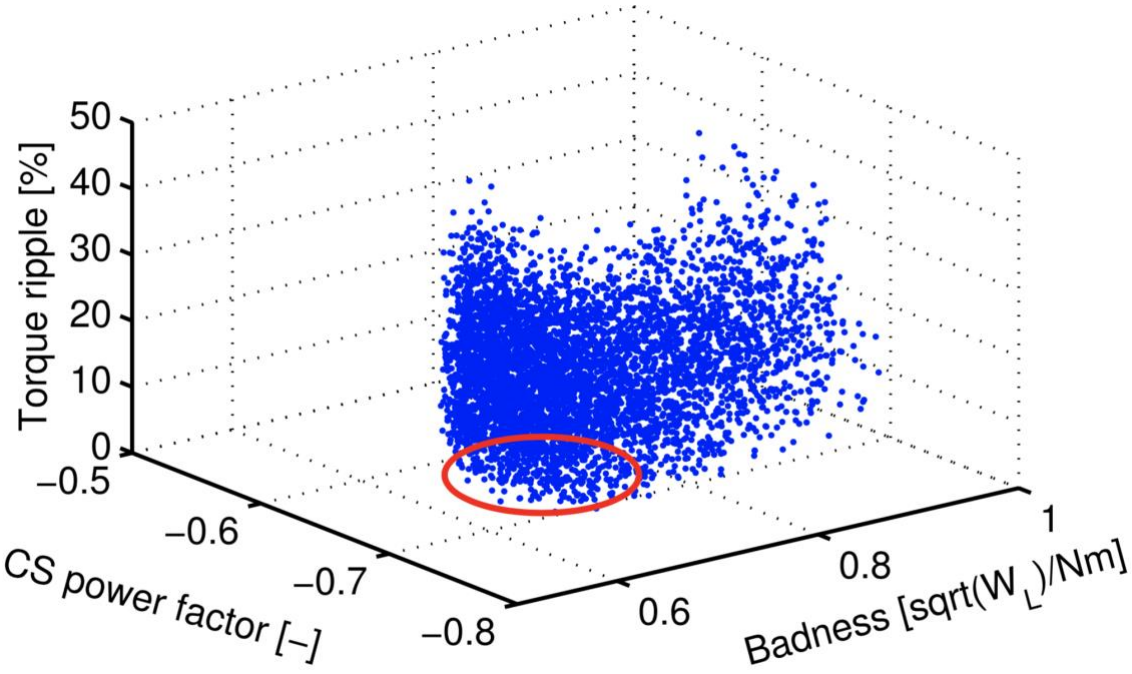

Figure 2.6 Scatter plot and the Pareto front representing numerous SynRM designs [85].

Analytical models, due to their computational efficiency, have also been widely adopted in optimal design problems of the SynRM. The average torque is maximized in [86] based on analytical derivations and the level set method. Multiple objectives can also

be achieved as discussed in [87], where the iron loss, average torque and torque ripple are all optimized in the final design based on analytical machine models and the NSGA-II optimization algorithm.

2.3.2 Design Optimization of Single-Phase Induction Machines

Single-phase IMs have been mass-produced for decades and are widely installed in house appliances due to their low cost and high reliability. However, most designs of the single-phase IMs are created decades ago, with a lot of design parameters chosen based on past experience. Consequently, more scientific design optimization approaches are proposed in the recent years due to the advance of computing technology. Similar to the design optimization of the SynRMs, design parameters of the single-phase IMs can be optimized in order to improve one or more performance indices, based on either the FEA modeling tool or the analytical models.

With the help of the FEA method, efficiency level of the single-phase IM is improved in [63] by adjusting the design parameters such as stator diameter, air-gap length, and the run capacitor value. The MOO is conducted in [62] by building the objective function from the weighted sum of the performance indices including energy cost and material cost. The generic algorithm (GA) is then adopted in [62] to solve the optimization problem.

An accurate analytical model solves much faster than the FEA simulation, and is also widely adopted in the optimal design problems of the single-phase IMs. The starting winding of the single-phase IM is optimized to improve the starting torque in [70] based on the circle diagram, which is obtained from the equivalent circuit model of the machine.

Commercially available software, such as the Rmxprt package in Ansys Maxwell, can also analyze the machine performance analytically, which allows designers to conduct the MOO for the single-phase IM in a more convenient way [74, 76].

2.4 Chapter Summary

This chapter summarizes the current literature focusing on the modeling and design optimization methods for SynRMs and single-phase IMs.

For the two types of machines, both the numerical FEA modeling method and the analytical models are presented. It can be concluded that although the FEA method can provide accurate calculation of machine performance, the analytical model is more suitable during the optimization process due to its computational efficiency. Approaches to solve the optimization problem are also summarized. The design optimization problem can focus on one or more performance indices with various algorithms such as genetic algorithm (GA), differential evolution (DE) and their modified versions.

The literature review indicates the necessity of developing fast and accurate analytical models for both the SynRM and the single-phase IM, after which the MOO can be conducted with proper algorithms. Detailed approaches will be illustrated in the following chapters.

CHAPTER 3. GENERALIZED ELECTRO-MAGNETIC MODEL OF SYNCHRONOUS RELUCTANCE MACHINES

It has been demonstrated in Chapters 1 and 2 that a fast and accurate model for the synchronous reluctance machine (SynRM) is indispensable for the machine design optimization process. The finite element analysis (FEA) tool is convenient, accurate and commercially available, while consumes large amount of time and is thus undesired during design optimization of the SynRM, where numerous simulations for the machine performance are conducted in order to finally converge to the optimal design. Consequently, analytical models, based on either the magnetic equivalent circuit (MEC) or the Maxwell's equations, are ideal for the optimization problem due to their computational efficiency. This chapter starts with an introduction of the basic principles of the SynRMs, followed by detailed derivation of the novel analytical model based on the Maxwell's equations and conformal mapping technique. Calculation results of the model is verified with FEA simulation, proving the accuracy and reliability of the proposed SynRM analytical model.

3.1 Basic Principles of the Synchronous Reluctance Machines

The SynRM is a special type of the well-known synchronous machine, whose rotor rotates in the same speed as the rotating magnetic field in the machine air-gap. The two-dimensional (2D) geometry of a typical three-phase four-pole SynRM [88] is presented in Figure 3.1. The gray regions indicate the iron laminations while the white parts represent the air. The rotor shaft is omitted and is thus replaced by air in the figure.

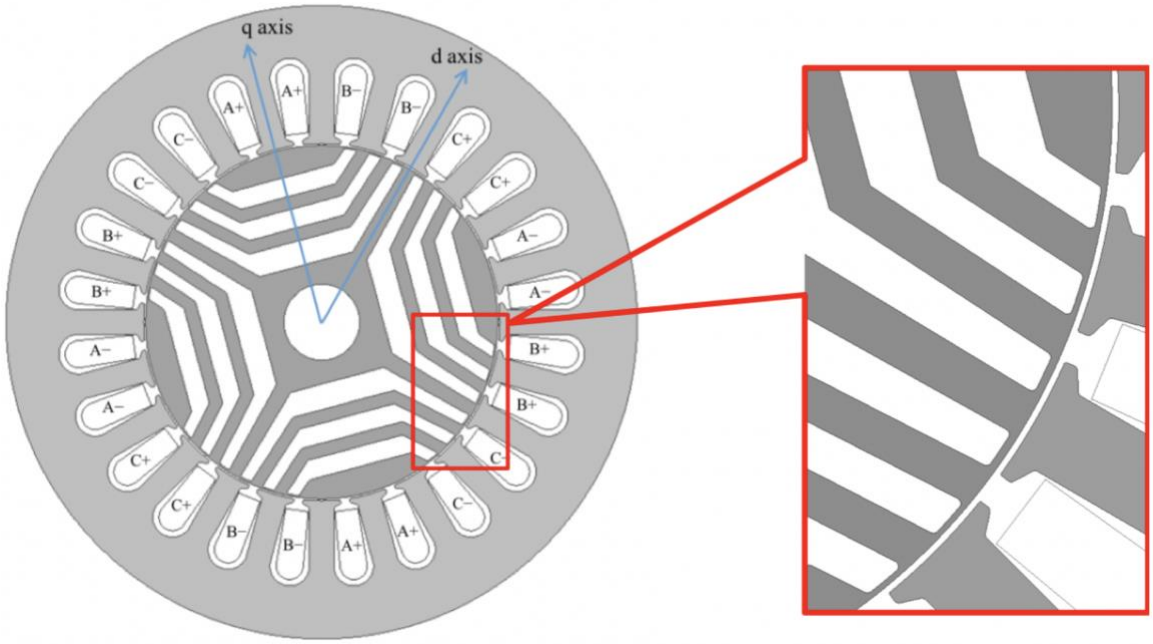

Figure 3.1 2D geometry of a typical SynRM.

It can be observed that the stator of the SynRM is almost the same as the induction machine (IM) stator. For the 24-slot three-phase SynRM presented in Figure 3.1, the phases allocated to each slot are market by letters A, B, and C, while the '+' and '−' signs indicate the directions of current. The rotor, however, is uniquely hollowed, with the iron segments connected by the tiny thin bridges on the edge of the rotor, which are named as the flux bridges. The hollowed air regions are called the flux barriers, creating tremendous anisotropy for the machine inductances. The Park Transformation [89] is also applicable to the SynRM, making the analysis and control techniques of the SynRM quite similar to that of a normal permanent-magnet synchronous machine (PMSM). Conventionally, the direction with smaller reluctance and consequently larger inductance is defined as the direct axis, or the *d* axis, while the direction leading the *d* axis by 45 electrical degrees and having smaller inductance is defined as the quadrature axis, or the *q* axis. Both axes are

marked in Figure 3.1, and the electro-magnetic (EM) torque of the SynRM can be calculated as(3.1):

$$T_{em} = \frac{3}{2} P\left(L_d - L_q\right) i_d i_q \tag{3.1}$$

where P is the number of pole pairs, L_d and L_q are the inductances of d and q axes, i_d and i_q are the amplitudes of the d and q current vectors.

It can be noticed from (3.1) that increasing the discrepancy between the inductance values on the d and q directions will yield to higher EM torque of the machine. Various rotor topologies of the SynRMs are thus proposed with the same purpose of increasing such discrepancy called the salient ratio. The shape of the flux barriers on each rotor pole can be either C-shaped, as shown in Figure 3.1, or circular, as presented in Figure 3.2 [43]. Iron ribs can be added in the center of the flux barriers, shown in Figure 3.3 [90], in order to increase the mechanical strength of the rotor, while decreases the saliency ratio due to the added permeance on the q axis. The number of flux barriers in each pole may vary from one to near ten [91] in the literature, while the most common number is between two and four.

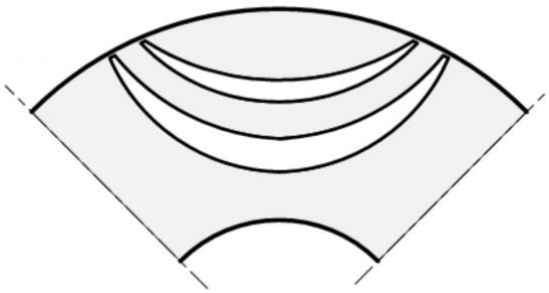

Figure 3.2 A quarter of the SynRM rotor with circular flux barriers [43].

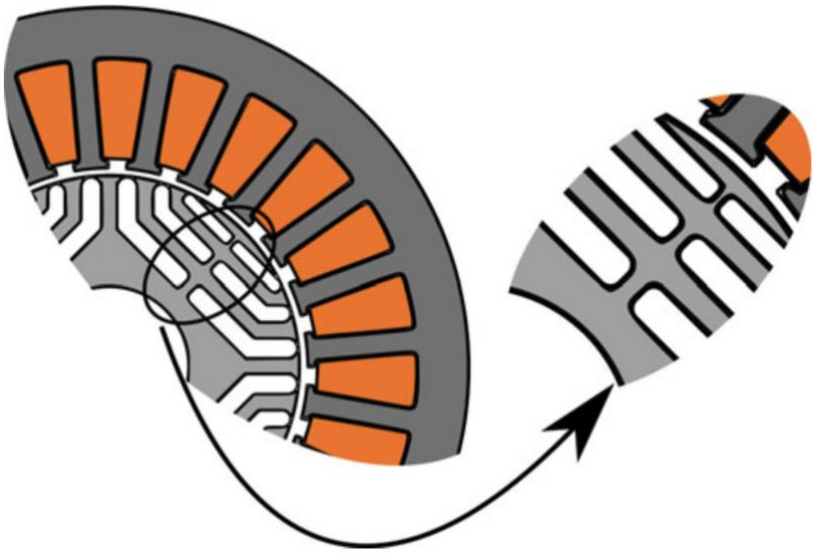

Figure 3.3 A SynRM with iron ribs added in the rotor flux barriers [90].

3.2 Derivation of the Analytical Model

This section introduces the novel analytical model based on Maxwell's equations that is able to compute the air-gap flux density of the SynRM. The proposed model is capable of determining the electromagnetic performance of a SynRM in a few seconds, much faster than a single FEA run, which typically takes 1-2 minutes on an ordinary desktop computer. Such time efficiency further ensures the fast speed during the optimization process, where hundreds of designs need to be simulated.

The proposed analytical model starts from calculating the air-gap flux density of the SynRM by taking advantage of conformal mapping technique and Maxwell's equations. Both stator and rotor slot effects are taken into consideration by conformal mapping, so that the potential equations can be solved under complicated geometric boundaries. A nonlinear MEC model is built to take the saturation effect into consideration by solving iteratively, and finally yields magnetic potentials on the rotor. Such magnetic

potentials are then used as boundary conditions to solve the potential equations and calculate the air-gap flux density, from which the *d* and *q* axes magnetizing inductance and the machine EM torque can be computed. The flux density values in the SynRM iron are derived from the MEC model, after which the machine iron loss can be calculated.

The SynRM presented in Figure 3.1 is adopted for illustrating the derivations of the model, while the proposed analytical model is capable of analyzing all the SynRMs with typical rotor geometries. Figure 3.4 shows the flowchart for calculating the SynRM air-gap flux density, which is a crucial part for machine performance calculation.

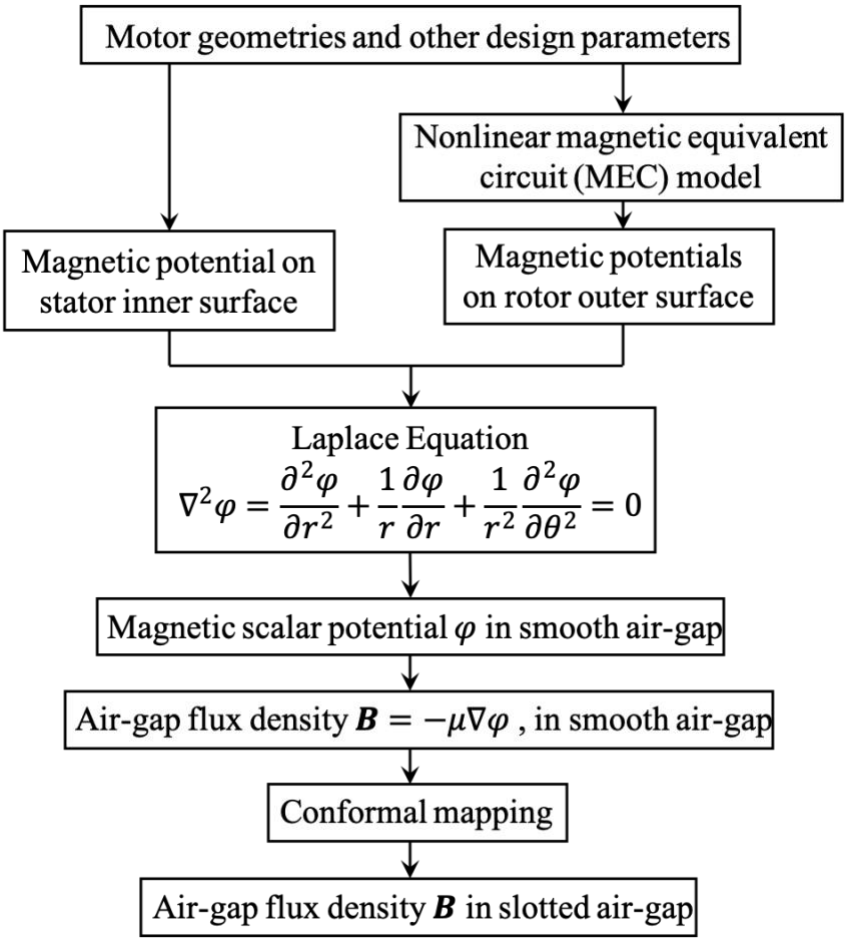

Figure 3.4 Flowchart of the calculation procedure for the air-gap flux density.

3.2.1 Magnetic Equivalent Circuit Model of Synchronous Reluctance Machines

The nonlinear MEC model is adopted in order to analyze the saturation effect. The following assumptions are made when building the MEC model of the SynRM:

- The cross section of the SynRM remains constant along the axial direction.
- The leakage flux and fringing flux in the machine end region is neglected.
- As the iron bridges on the rotor are highly saturated under the normal working conditions of a SynRM, the relative permeability in these parts is very low. So, the regions of the iron bridges on the rotor are considered vacuums, so a slotted rotor is analyzed [92].

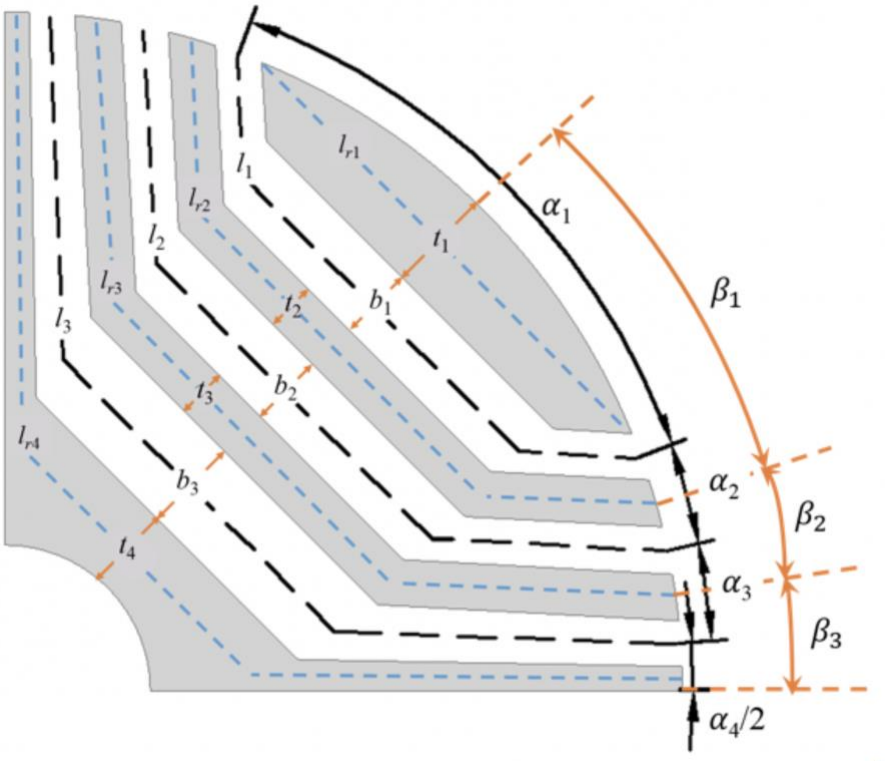

Figure 3.5 Rotor geometric parameters.

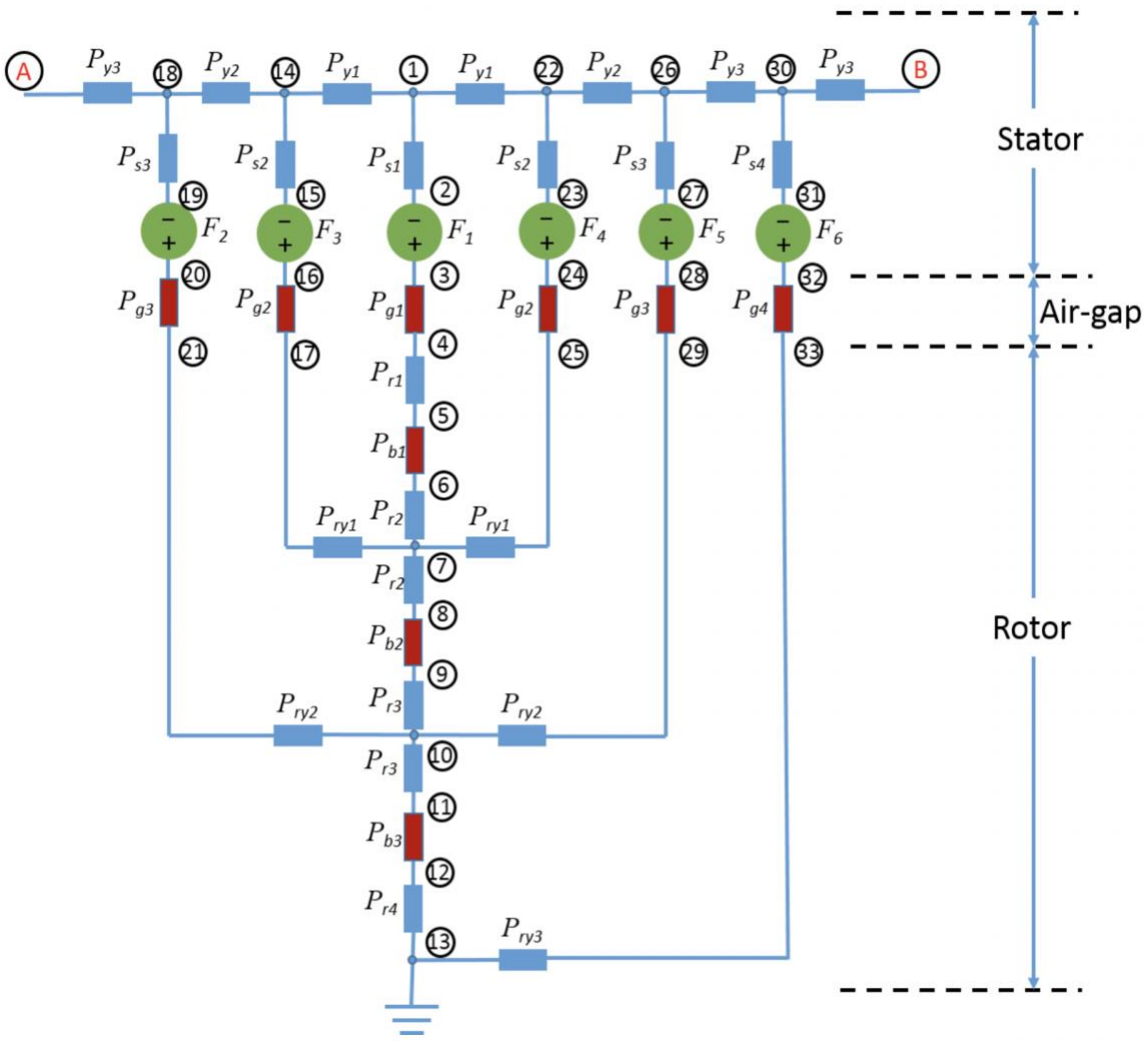

Figure 3.6 The MEC model.

Only a quarter (one pole) of the SynRM is analyzed due to its symmetrical geometry. Figure 3.5 indicates the geometric parameters of the SynRM. The magnetic circuit network is shown in Figure 3.6, where the blue permeances represent the nonlinear elements, and the red permeances represent the linear air-region permeances. The values of the magnetomotive force (MMF) sources can be calculated from the stator MMF as follows:

$$F_1 = \frac{1}{P\alpha_1}\int_{\theta_r-\frac{1}{2}\alpha_1 P}^{\theta_r+\frac{1}{2}\alpha_1 P} F(t,\theta)\, d\theta \tag{3.2}$$

$$F_2 = \frac{1}{P\alpha_3}\int_{\theta_r+P(\frac{1}{2}\alpha_1+\alpha_2)}^{\theta_r+P(\frac{1}{2}\alpha_1+\alpha_2+\alpha_3)} F(t,\theta)\, d\theta \tag{3.3}$$

$$F_3 = \frac{1}{P\alpha_2}\int_{\theta_r+\frac{1}{2}\alpha_1 P}^{\theta_r+P(\frac{1}{2}\alpha_1+\alpha_2)} F(t,\theta)\, d\theta \tag{3.4}$$

$$F_4 = \frac{1}{P\alpha_2}\int_{\theta_r-P(\frac{1}{2}\alpha_1+\alpha_2)}^{\theta_r-\frac{1}{2}\alpha_1 P} F(t,\theta)\, d\theta \tag{3.5}$$

$$F_5 = \frac{1}{P\alpha_3}\int_{\theta_r-P(\frac{1}{2}\alpha_1+\alpha_2+\alpha_3)}^{\theta_r-P(\frac{1}{2}\alpha_1+\alpha_2)} F(t,\theta)\, d\theta \tag{3.6}$$

$$F_6 = \frac{1}{P\alpha_4}\int_{\theta_r-P\left(\frac{1}{2}\alpha_1+\alpha_2+\alpha_3+\alpha_4\right)}^{\theta_r-P\left(\frac{1}{2}\alpha_1+\alpha_2+\alpha_3\right)} F(t,\theta)\, d\theta \tag{3.7}$$

where P is the number of pole pairs of the machine, θ_r is the electrical angle (in radians) between the winding phase *a* symmetry axis and the rotor *q* axis, θ is the angular position measured by taking the phase *a* symmetry axis as a zero reference, *t* represents time and $F(t,\theta)$ refers to the stator MMF, computed by [43]:

$$F(t,\theta) = \sum_{n=0,1,2} w_n(\theta)\cdot i_n(t) \tag{3.8}$$

where n is the phase index, ranging from 0 to 2 (0 stands for phase *a*, 1 for phase *b*, and 2 for phase *c*); $i_n(t)$ is the current in phase *n* at time *t*, and is defined in such a way that the current in phase *a* reaches its maximum value when time *t* equals zero:

$$i_n(t) = I_0 \cos(\omega t - \frac{2}{3}\pi n) \tag{3.9}$$

$w_n(\theta)$ is the winding function of phase *n* [43]:

$$w_n(\theta) = \sum_{k=1,3,5,..} W_k \cdot \cos\left[k(\theta - \frac{2}{3}\pi n)\right] \tag{3.10}$$

$$W_k = \frac{2}{\pi} \cdot N_s \cdot \frac{\sin(\pi k/2)}{k} \frac{\sin(\alpha_s q k/2)}{\sin(\alpha_s k/2)} \tag{3.11}$$

where I_0 is the peak value of the phase current, N_s is the number of turns per coil, q is the number of slots per pole per phase, and $\alpha_s = \pi/(3q)$ is the electrical angle of the slot pitch.

The MEC shown in Figure 3.6 has 33 nodes, and *node 13* has been chosen as the ground point whose magnetic scalar potential is zero. As a consequence, 32 nodal equations are needed to solve the circuit network. For a normal node adjacent to only the permeances, such as *node 22*, the nodal equation can be written as:

$$(V_{26} - V_{22})P_{y2} + (V_1 - V_{22})P_{y1} + (V_{23} - V_{22})P_{s2} = 0 \tag{3.12}$$

where V_x stands for the magnetic scalar potential of *node x*. A total of 18 nodal equations can be obtained with the similar technique.

As for *node 18* and *node 30*, which are located on the border of the network shown in Figure 2.3, we note that the machine has a symmetric geometry so that the magnetic scalar potentials of *nodes A* and *B* are equal to -V_{30} and -V_{18}, respectively. So, the nodal equations on *nodes 18* and *30* are listed as:

$$(-V_{30} - V_{18})P_{y3} + (V_{14} - V_{18})P_{y2} + (V_{19} - V_{18})P_{s3} = 0 \tag{3.13}$$

$$(-V_{18} - V_{30})P_{y3} + (V_{26} - V_{30})P_{y3} + (V_{31} - V_{30})P_{s4} = 0 \tag{3.14}$$

For nodes that are adjacent to the MMF sources, such as *nodes 2* and *3*, two equations can be obtained for each pair of nodes:

$$V_3 - V_2 = F_1 \tag{3.15}$$

$$(V_1 - V_2)P_{s1} + (V_4 - V_3)P_{g1} = 0 \tag{3.16}$$

There are 12 nodes adjacent to the 6 MMF sources, so we can obtain 12 more equations following such scheme.

The combination of the nodal equations can be integrated into the matrix form:

$$\mathbf{P} \cdot \mathbf{V} = \mathbf{f} \tag{3.17}$$

where **P** is the matrix related to the permeances, **V** is the vector of the potentials at the nodes in the magnetic circuit, and **f** is the vector associated with the MMF sources in the node equations.

Each individual permeance in the MEC model presented in Figure 3.6 is calculated from the following equation:

$$P = \frac{\mu_0 \mu_r A}{l} \tag{3.18}$$

where μ_0 is the permeability of free space, μ_r is the relative permeability of the corresponding material, A is the cross-sectional area of the segment in the MEC orthogonal to the flux lines , and l is the length of the segment in the MEC along the direction of the flux lines.

Since the relative permeability of air can be considered as 1, μ_r is counted to have a constant value of 1 when calculating the permeances for the air regions, which are marked red in Figure 3.6. As the relative permeability of the rotor and stator steel is not constant due to saturation effects, an iterative method is desired to solve the nonlinear equations based on the manufacturer provided **B-H** curve of stator/rotor laminations. The initial relative permeability of all iron parts should be arbitrarily chosen before the first iteration. After solving the nodal equations based on the chosen permeability, the magnetic potential on each node can be obtained, which leads to the solutions of the flux densities in each iron segment. Then, the relative permeability can be updated based on the solved flux densities and the **B-H** curve, so that the next iteration can be conducted. The iterative procedure terminates when $\|\boldsymbol{\mu}_{\mathbf{rc}} - \boldsymbol{\mu}_{\mathbf{rp}}\| \leq \delta$, where $\boldsymbol{\mu}_{\mathbf{rc}}$ and $\boldsymbol{\mu}_{\mathbf{rp}}$ are the relative permeability vector $\boldsymbol{\mu}_{\mathbf{r}}$ at the current iteration and the previous iteration respectively, and δ is the threshold. The final $\boldsymbol{\mu}_{\mathbf{rc}}$ will be used as $\boldsymbol{\mu}_{\mathbf{r}}$ in order to calculate the permeances in the steel regions, marked in blue in Figure 3.6. The vector of the magnetic potentials on the nodes, **V**, can

then be calculated from the node equations. The flowchart for solving the nonlinear nodal equations is presented in Figure 3.7.

Once the solution is obtained, the magnetic potentials of the nodes on the rotor surface are utilized as boundary conditions to compute the air-gap flux densities, as introduced in the succeeding section. As the values of the MMF sources in the MEC are functions of time according to (3.2)-(3.7), the solved magnetic potentials also vary with time, which obeys the theory of the rotating magnetic field in the synchronous machine.

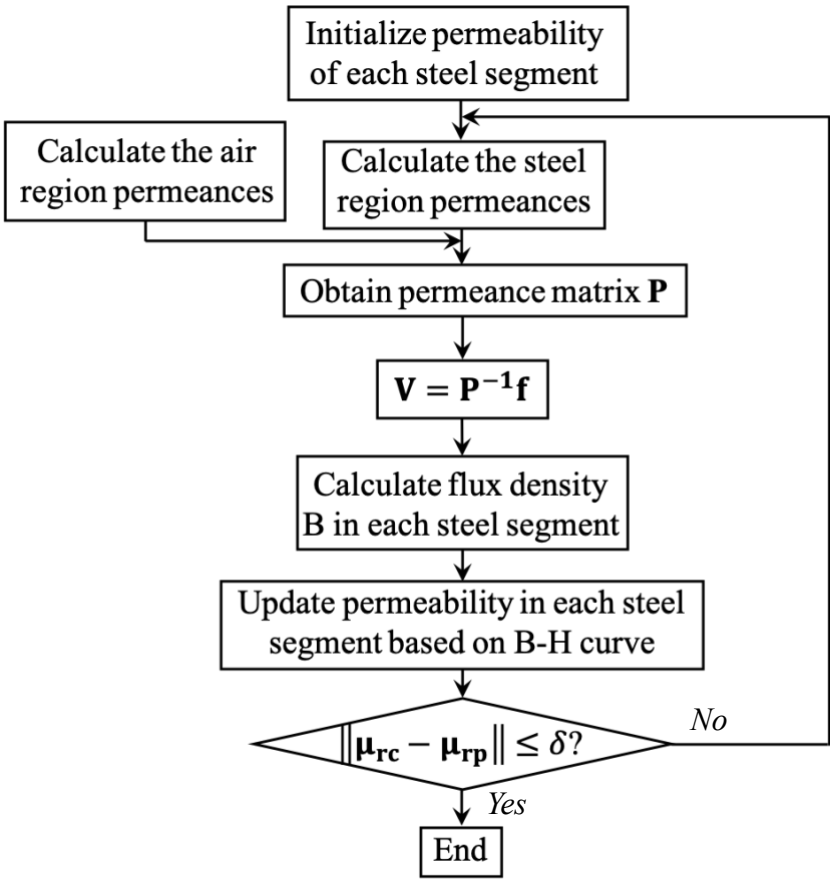

Figure 3.7 Flowchart for solving the nonlinear magnetic circuit.

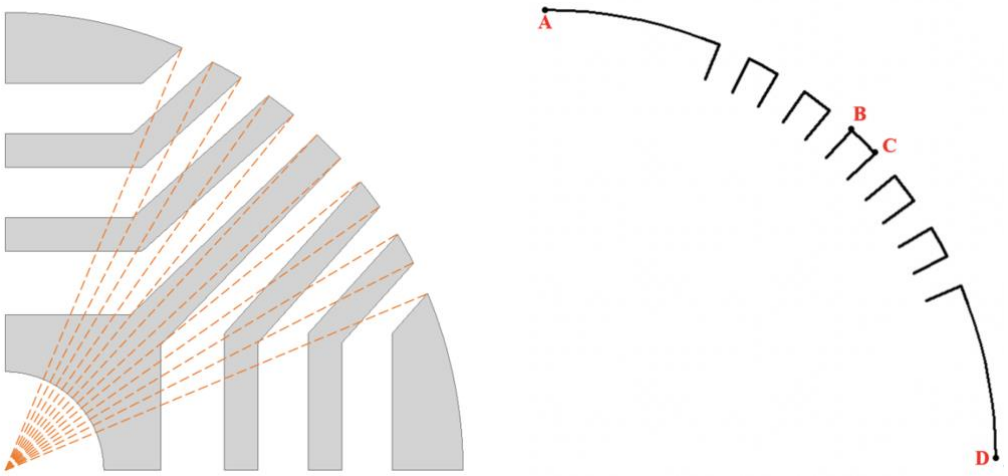

(a) (b)

Figure 3.8 Simplified rotor geometry: (a) Modeling the rotor slots by sectors indicated by the dashed lines; (b) Rotor geometry in the *S* plane.

3.2.2 Calculation of the Air-gap Flux Density

3.2.2.1 Conformal Mapping of the Air-gap Region

The air-gap region with the rotor and stator slots can be transformed into a slot-less air-gap through conformal mapping. Figure 3.8(a) shows the real rotor geometry, and Figure 3.8(b) shows the rotor geometry in the *S* plane, where the coordinates are represented as complex numbers under the polar coordinate system as: $s = re^{j\theta}$. The rotor slots are modeled as sectors, with the slot openings at their original locations, as shown in Figure 3.8. The procedure to transform the geometry into a slot-less air-gap region is shown in Figure 3.9, and the mappings between the different planes can be expressed as follows:

From the *S* plane to the *Z* plane:

$$z = \ln(s) \tag{3.19}$$

where s and z are the coordinates in the *S* plane and the *Z* plane, respectively.

From the *Z* plane to the *W* plane:

$$w = f(z) \tag{3.20}$$

where w is the coordinate in the W plane, and f is a nonlinear function which can be realized by the S-C mapping toolbox in MATLAB [93].

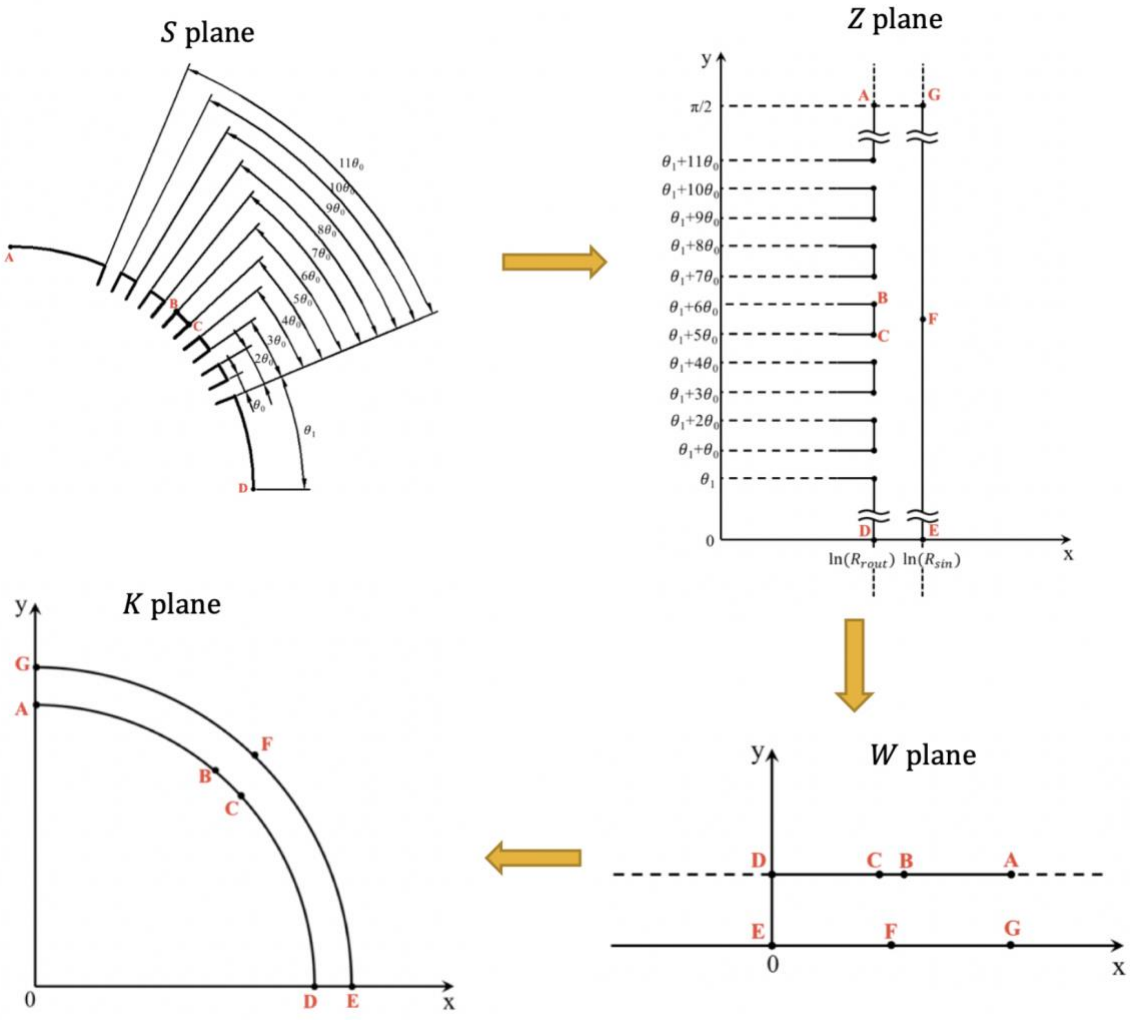

Figure 3.9 Conformal mappings that transform the geometry from the *S* plane to the *K* plane.

The S-C mapping that transforms a polygon into the upper half plane is stated as follows [94]: *Let P be the interior of a polygon Γ having n vertices $w_1, \dots w_n$, and interior angles $\alpha_1\pi, \dots \alpha_n\pi$, in counterclockwise order. Let f be any conformal map from the upper half-plane H^+ to P with $f(\infty) = w_n$. Then, for some complex constants A_0 and C_0, where $w_k = f(z_k)$ for $k = 1, \dots, n-1$*

$$w = f(z) = A_0 + C_0 \int_{z_0}^{z} \prod_{k=1}^{n-1} (\xi - z_k)^{\alpha_k - 1} \mathrm{d}\xi \tag{3.21}$$

where $z = x + jy$ and $w = u + jv$ denote complex numbers in the Z and W planes, respectively.

From the *W* plane to the *K* plane:

$$k = \left(\frac{R_{sin}}{R_{rout}}\right)^{wj} \cdot R_{sin} \tag{3.22}$$

where R_{sin} is the stator inner radius, and R_{rout} is the rotor outer radius.

The relationship between the air-gap flux density in the *K* plane and the *S* plane can be expressed as:

$$\boldsymbol{B_s} = \boldsymbol{B_k}\lambda^*_{r\_slot} = \boldsymbol{B_k}\left(\frac{\partial k}{\partial s}\right)^* = \boldsymbol{B_k}\left(\frac{\partial k}{\partial w}\frac{\partial w}{\partial z}\frac{\partial z}{\partial s}\right)^* \tag{3.23}$$

where $\partial w/\partial z$ can be obtained from the S-C transformation toolbox, $\lambda^*_{r\_slot}$ is defined as the complex air-gap permeance considering the effect of slotted rotor, and $\boldsymbol{B_s}$ and $\boldsymbol{B_k}$ represent the flux density solution in the *S* and *K* planes respectively, denoted as:

$$\boldsymbol{B_s} = B_{sr} + jB_{s\theta} \tag{3.24}$$

$$\boldsymbol{B_k} = B_r + jB_\theta \tag{3.25}$$

Following steps similar to those stated above, the complex air-gap permeance considering only the effect of slotted stator can be obtained, and is denoted as $\lambda^*_{s\_slot}$. The complex permeances $\lambda^*_{r\_slot}$ and $\lambda^*_{s\_slot}$ can then be represented as:

$$\lambda^*_{r\_slot} = \lambda_{ar} - j\lambda_{br} \tag{3.26}$$

$$\lambda^*_{s\_slot} = \lambda_{as} - j\lambda_{bs} \tag{3.27}$$

Then, the radial component of the flux density under S plane can be computed as:

$$\begin{aligned} B_{sr} &= \mathrm{Re}\left(\boldsymbol{B_k}\lambda^*_{r_{slot}}\lambda^*_{s_{slot}}\right) \\ &= B_r(\lambda_{ar}\lambda_{as} - \lambda_{br}\lambda_{bs}) + B_\theta(\lambda_{ar}\lambda_{bs} + \lambda_{br}\lambda_{as}) \end{aligned} \tag{3.28}$$

It is now obvious that solving for $\boldsymbol{B_k}$, which is the flux density of the slotless air-gap in the *K* plane, is essential in obtaining the flux density solution of the slotted air-gap. The following part shows the method of solving $\boldsymbol{B_k}$.

3.2.2.2 Magnetic Field Solution in the Air-gap

The Laplace's equation of magnetic scalar potential under a polar coordinate system is written as:

$$\nabla^2\varphi = \frac{\partial^2\varphi}{\partial r^2} + \frac{1}{r}\frac{\partial\varphi}{\partial r} + \frac{1}{r^2}\frac{\partial^2\varphi}{\partial\theta^2} = 0 \tag{3.29}$$

where $\varphi(r,\theta)$ is the magnetic scalar potential. The homogeneous solution of (3.29) is in the form of:

$$\varphi(r,\theta) = \sum_{n=1}^{\infty}[(A_n r^n + B_n r^{-n})\cos(n\theta) + (C_n r^n + D_n r^{-n})\sin(n\theta)] \tag{3.30}$$

where A_n, B_n, C_n, D_n and m_n are coefficients to be determined by the boundary conditions.

With the slot-less rotor and stator, the boundary conditions can be listed as follows:

- On the stator's inner surface, the magnetic scalar potential is equal to the MMF produced by the stator windings, as derived in (3.2)-(3.11). It can be formulated in the following form:

$$\begin{aligned} F(t,\theta) = I_0\cos(\omega t)\cdot\sum_{k=1,3,5,..} W_k\left[1-\cos\left(\frac{2k\pi}{3}\right)\right]\cos(k\theta) \\ + \sqrt{3}I_0\sin(\omega t)\cdot\sum_{k=1,3,5,..} W_k\sin\left(\frac{2k\pi}{3}\right)\sin(k\theta) \\ = \sum_{k=1,3,5,..} F_{k1}\cos(k\theta) + \sum_{k=1,3,5,..} F_{k2}\sin(k\theta) \end{aligned} \tag{3.31}$$

where the derivation of W_k has been shown in (3.11).

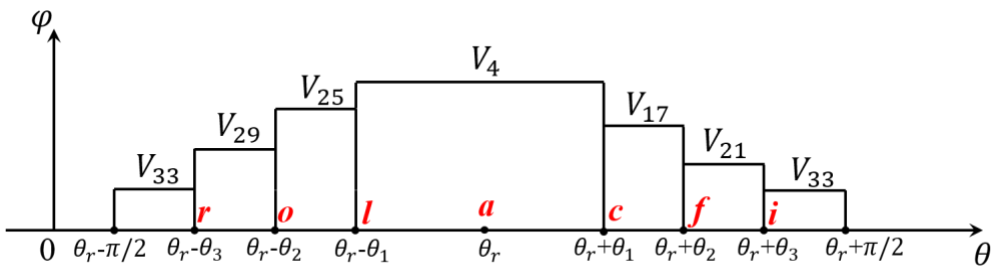

(a)

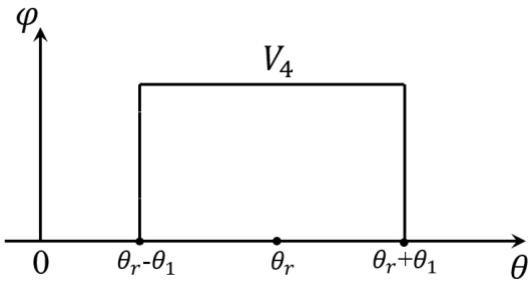

(b)

Figure 3.10 (a) Magnetic potential on the rotor surface; (b) The decomposed wave.

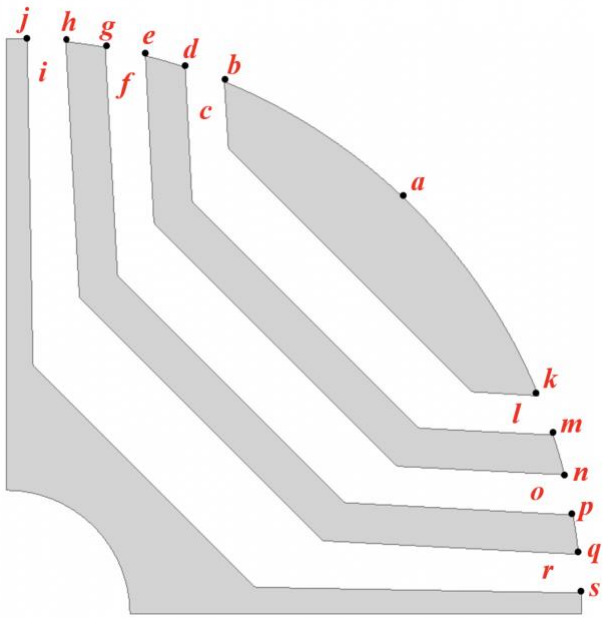

Figure 3.11 Vertices on the rotor.

- On the rotor's outer surface, the magnetic scalar potential has been computed by the MEC model in Section 3.2.1, and is plotted in Figure 3.10(a). It has a stepped waveform, and the amplitudes in the steps V_x stands for the magnetic scalar potentials of *node x* in the MEC, as presented in Figure 3.6. The nodes marked on the horizontal axis correspond to the vertices marked on the slotted rotor shown in Figure 3.11, and are related to the vertices in Figure 3.11 by the conformal mapping technique introduced in Section 3.2.2.1. Consequently, the values of θ_1, θ_2 and θ_3 are obtained from the rotor geometry and conformal mapping, while θ_r refers to the electrical angle (in radians) between the winding phase *a* symmetry axis and the rotor *q* axis, and can be calculated by:

$$\theta_r = \theta_0 + \omega t \tag{3.32}$$

where θ_0 is the electrical angle (in radians) between the winding phase *a* symmetry axis and the rotor *q* axis when time *t* equals zero. The waveform plotted in Figure 3.10(a) can be decomposed into multiple waves in the form shown in Figure 3.10(b), whose Fourier series can be written as:

$$\begin{aligned} F'_{partial}(t,\theta) = {} & \frac{4V_4}{\pi} \sum_{k=1,3,5,..} \frac{\sin(k\theta_1)}{k} \cos(k\theta_r) \cos(k\theta) \\ & + \frac{4V_4}{\pi} \sum_{k=1,3,5,..} \frac{\sin(k\theta_1)}{k} \sin(k\theta_r) \sin(k\theta) \end{aligned} \tag{3.33}$$

The Fourier series of the other decomposed waves can be obtained with the same method, and then superimposed upon the other to get the Fourier series of the

magnetic scalar potential on the rotor's outer surface, which obeys the following form:

$$F'(t,\theta) = \sum_{k=1,3,5,..} F'_{k1}\cos(k\theta) + \sum_{k=1,3,5,..} F'_{k2}\sin(k\theta) \tag{3.34}$$

where

$$\begin{aligned} F'_{k1} = {} & \frac{4V_4}{\pi}\frac{\sin(k\theta_1)}{k}\cos(k\theta_r) \\ & + \frac{4V_{17}}{\pi}\frac{\sin[k(\theta_2-\theta_1)/2]}{k}\cos[k(\theta_r+\frac{\theta_1+\theta_2}{2})] \\ & + \frac{4V_{21}}{\pi}\frac{\sin[k(\theta_3-\theta_2)/2]}{k}\cos[k(\theta_r+\frac{\theta_2+\theta_3}{2})] \\ & + \frac{4V_{33}}{\pi}\frac{\sin[k(\frac{\pi}{2}-\theta_3)/2]}{k}\cos[k(\theta_r+\frac{\theta_3+\frac{\pi}{2}}{2})] \\ & + \frac{4V_{25}}{\pi}\frac{\sin[k(\theta_2-\theta_1)/2]}{k}\cos[k(\theta_r-\frac{\theta_1+\theta_2}{2})] \\ & + \frac{4V_{29}}{\pi}\frac{\sin[k(\theta_3-\theta_2)/2]}{k}\cos[k(\theta_r-\frac{\theta_2+\theta_3}{2})] \\ & + \frac{4V_{33}}{\pi}\frac{\sin[k(\frac{\pi}{2}-\theta_3)/2]}{k}\cos[k(\theta_r-\frac{\theta_3+\frac{\pi}{2}}{2})] \end{aligned} \tag{3.35}$$

$$
\begin{aligned}
F'_{k2} = \frac{4V_4}{\pi}\frac{\sin(k\theta_1)}{k}\sin(k\theta_r) \\
&+ \frac{4V_{17}}{\pi}\frac{\sin[k(\theta_2-\theta_1)/2]}{k}\sin[k(\theta_r+\frac{\theta_1+\theta_2}{2})] \\
&+ \frac{4V_{21}}{\pi}\frac{\sin[k(\theta_3-\theta_2)/2]}{k}\sin[k(\theta_r+\frac{\theta_2+\theta_3}{2})] \\
&+ \frac{4V_{33}}{\pi}\frac{\sin[k(\frac{\pi}{2}-\theta_3)/2]}{k}\sin[k(\theta_r+\frac{\theta_3+\frac{\pi}{2}}{2})] \\
&+ \frac{4V_{25}}{\pi}\frac{\sin[k(\theta_2-\theta_1)/2]}{k}\sin[k(\theta_r-\frac{\theta_1+\theta_2}{2})] \\
&+ \frac{4V_{29}}{\pi}\frac{\sin[k(\theta_3-\theta_2)/2]}{k}\sin[k(\theta_r-\frac{\theta_2+\theta_3}{2})] \\
&+ \frac{4V_{33}}{\pi}\frac{\sin[k(\frac{\pi}{2}-\theta_3)/2]}{k}\sin[k(\theta_r-\frac{\theta_3+\frac{\pi}{2}}{2})]
\end{aligned}
\tag{3.36}
$$

When one substitutes the boundary conditions into (3.30), it yields:

$$
\begin{cases}
A_n R_{sin}^n + B_n R_{sin}^{-n} = F_{k1} \\
C_n R_{sin}^n + D_n R_{sin}^{-n} = F_{k2} \\
A_n R_{rout}^n + B_n R_{rout}^{-n} = F'_{k1} \\
C_n R_{rout}^n + D_n R_{rout}^{-n} = F'_{k2}
\end{cases}
\tag{3.37}
$$

where F'_{k1} and F'_{k2} are formulated in (3.35) and (3.36), while F_{k1} and F_{k2} are defined following (3.31):

$$
F_{k1} = I_0 \cos(\omega t)\cdot W_k\left[1-\cos\left(\frac{2k\pi}{3}\right)\right] \tag{3.38}
$$

$$
F_{k2} = \sqrt{3} I_0 \sin(\omega t)\cdot W_k \sin\left(\frac{2k\pi}{3}\right) \tag{3.39}
$$

Solving (3.37) and plugging in the sovled A_n, B_n, C_n and D_n into (3.30) gives the expression of the magnetic scalar potential in the air-gap:

$$\begin{aligned}\varphi(r,\theta,t) = \sum_{n=1,3,5,..}\Bigg[& F_{k1}\frac{\left(\frac{r}{R_{rout}}\right)^{n}-\left(\frac{r}{R_{rout}}\right)^{-n}}{\left(\frac{R_{sin}}{R_{rout}}\right)^{n}-\left(\frac{R_{sin}}{R_{rout}}\right)^{-n}} \\ & + F'_{k1}\frac{\left(\frac{r}{R_{sin}}\right)^{n}-\left(\frac{r}{R_{sin}}\right)^{-n}}{\left(\frac{R_{rout}}{R_{sin}}\right)^{n}-\left(\frac{R_{rout}}{R_{sin}}\right)^{-n}}\Bigg]\cos(n\theta) \\ + \sum_{n=1,3,5,..}\Bigg[& F_{k2}\frac{\left(\frac{r}{R_{rout}}\right)^{n}-\left(\frac{r}{R_{rout}}\right)^{-n}}{\left(\frac{R_{sin}}{R_{rout}}\right)^{n}-\left(\frac{R_{sin}}{R_{rout}}\right)^{-n}} \\ & + F'_{k2}\frac{\left(\frac{r}{R_{sin}}\right)^{n}-\left(\frac{r}{R_{sin}}\right)^{-n}}{\left(\frac{R_{rout}}{R_{sin}}\right)^{n}-\left(\frac{R_{rout}}{R_{sin}}\right)^{-n}}\Bigg]\sin(n\theta)\end{aligned} \tag{3.40}$$

The air-gap flux density $\boldsymbol{B_k}$ can then be solved from the air-gap magnetic potential, following:

$$B_r = -\mu_0\frac{\partial\varphi(r,\theta,t)}{\partial r} \tag{3.41}$$

$$B_\theta = -\mu_0\frac{1}{r}\frac{\partial\varphi(r,\theta,t)}{\partial\theta} \tag{3.42}$$

$$\boldsymbol{B_k} = B_r + jB_\theta \tag{3.43}$$

The radial flux density of the slotted airgap, B_{sr}, can be solved from $\boldsymbol{B_k}$, following (3.28). It is a function of the time *t*, radial position *r*, and circumferential angle θ, and thus can be expressed as $B_{sr}(r, \theta, t)$.

3.2.3 Perforamnce Calculations for Synchronous Reluctance Machines

Calculation of the SynRM performance indices, including the average torque, losses, efficiency, weight and torque density, are illustrated in this section.

The average torque of the SynRM can be calculated from the magnetizing inductances of the *d* and *q* axes following (3.1), while the following equation can be adopted by negleting the leakage inductances of the *d* and *q* axes:

$$T = \frac{3}{2} P (L_{md} - L_{mq}) i_d i_q \tag{3.44}$$

where P is the number of pole pairs, i_d and i_q are the amplitudes of the *d* and *q* current vectors, L_{md} and L_{mq} are the magnetizing inductances of the *d* and *q* axes.

The magnetizing inductance L_{md} can be calculated from the air-gap flux density by making θ_0 equal to $\pi/2$, under which condition the *q* axis leads the stator winding phase *a* symmetry axis by 90 electrical degrees when the time *t* equals to zero following (3.32). Since the current in the stator winding phase *a* is defined to be at the peak level when the time equals to zero, the stator winding MMF vector coincides with the phase *a* symmetry axis at this time point, and rotates in the same speed as the rotor as the time changes. Consequently, the stator winding MMF vector is always led by the rotor *q* axis for 90 electrical degrees, thus always coincides with the rotor *d* axis at any given time point. The

flux lines when the stator MMF vector coincides with the rotor *d* axis when the time *t* equals to zero is presented in Figure 3.12.

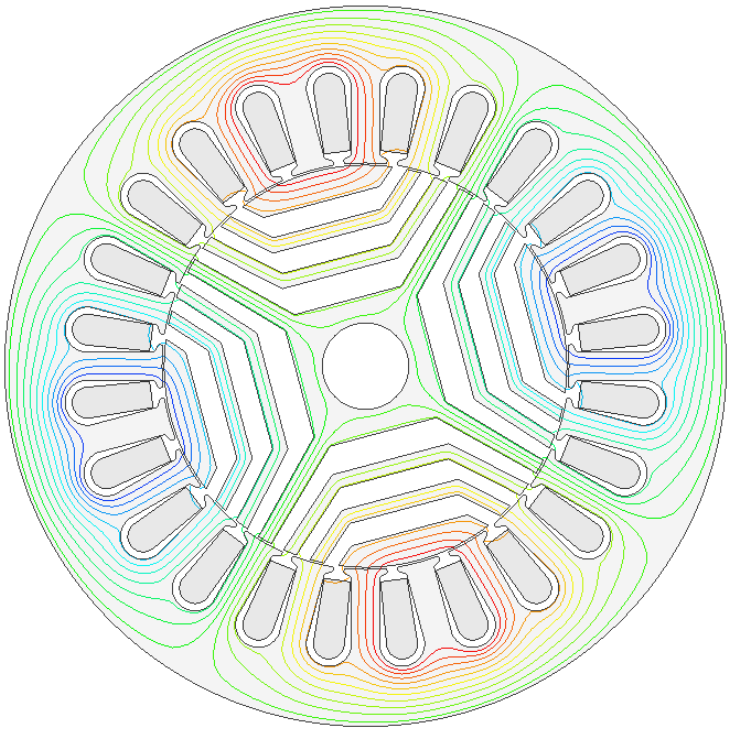

Figure 3.12 The flux lines when the stator MMF vector coincides with the rotor d axis.

Once the value of θ_0 is chosen, the SynRM air-gap flux density value on the radial direction, $B_{sr}(r,\theta,t)$, can be calculated following the procedure introduced in Section 3.2.2. The magnetizing flux linkage of the virtual *d* axis winding can be obtained by:

$$\lambda_{md}(t) = PqN_s l_{stack} r_{middle} \int_{-\frac{\pi}{2}+\omega t}^{\frac{\pi}{2}+\omega t} B_{sr}(r_{middle},\theta,t)\mathrm{d}\theta \tag{3.45}$$

where P is the number of pole pairs, q is the number of slots per pole per phase, N_s is the number of turns per coil, l_{stack} is the machine stack length, and r_{middle} is the radius of the

circumference in the middle of the air-gap. The magnetizing inductance of the *d* axis, L_{md}, can then be calculated by:

$$L_{md}(t) = \frac{\lambda_{md}(t)}{I_0} \tag{3.46}$$

where I_0 is the peak value of the phase current.

Similarly, the magnetizing inductance of the q axis, L_{mq}, can be calculated by solving $B_{sr}(r, \theta, t)$ with θ_0 equal to 0, and can be obtained by:

$$\lambda_{mq}(t) = PqN_s l_{stack} r_{middle} \int_{-\frac{\pi}{2}+\omega t}^{\frac{\pi}{2}+\omega t} B_{sr}(r_{middle}, \theta, t)\mathrm{d}\theta \tag{3.47}$$

$$L_{mq}(t) = \frac{\lambda_{mq}(t)}{I_0} \tag{3.48}$$

The electromagnetic torque of the SynRM can then be calculated from the solved L_{md} and L_{mq} values following (3.44).

The loss of the SynRM is primarily comprised of the copper loss and the iron loss. The copper loss is calculated by:

$$P_{Cu} = {I_{rms}}^2 R = {I_{rms}}^2 \cdot \frac{1}{\sigma_{Cu}} \cdot \frac{2N_s N(w_t + l_{stack})}{A_{Cu}} \tag{3.49}$$

where I_{rms} is the RMS value of the phase current, σ_{Cu} is the conductivity of copper windings, N is the total number of coils in the stator windings, w_t is the stator pole width, and A_{Cu} is the cross-sectional area of the copper wire used in the windings.

The iron losses of the machine are categorized into the hysterisis loss, caused by the hysteritic effect of the iron B-H curve, and the eddy current loss, generated by the eddy current induced from the alternating magnetic field. The losses can be calculated based on the method introduced in [95], formulated as:

$$P_{hys}(t) = \sum \left\{ \left| H_x \frac{dB_x}{dt} \right|^{\frac{2}{\beta}} + \left| H_y \frac{dB_y}{dt} \right|^{\frac{2}{\beta}} + \left| H_z \frac{dB_z}{dt} \right|^{\frac{2}{\beta}} \right\}^{\frac{\beta}{2}} \cdot V_i \tag{3.50}$$

$$P_{eddy}(t) = \sum \frac{1}{2\pi^2} k_c \left\{ \left(\frac{dB_x}{dt} \right)^2 + \left(\frac{dB_y}{dt} \right)^2 + \left(\frac{dB_z}{dt} \right)^2 \right\} \cdot V_i \tag{3.51}$$

where B_x, B_y and B_z are functions of the time *t* and represent the flux density values on the *x*, *y*, and *z* directions in the iron regions under the three-dimensional (3D) rectangular coordinate system, while V_i represents the volume of each of the segmented iron parts of the SynRM. k_c and β are empirical parameters obtained from experimental measurements. k_c is called as the eddy current loss coefficient, and β is called as the hysterisis loss parameter.

The values of H_x, H_y and H_z are calculated following:

$$H_x = \frac{1}{\pi} k_{hys} \cdot B_{xm} \tag{3.52}$$

$$H_y = \frac{1}{\pi} k_{hys} \cdot B_{ym} \tag{3.53}$$

$$H_z = \frac{1}{\pi} k_{hys} \cdot B_{zm} \tag{3.54}$$

where B_{xm}, B_{ym} and B_{zm} are the maximum values of B_x, B_y and B_z, and k_{hys} is another empirical parameter called as the hysterisis loss coefficient.

Iron-region flux density values, B_x, B_y and B_z, are calculated from the MEC model introduced in Section 3.2.1. The MEC model yields solutions of the magnetic potentials on all the nodes of the circuit shown in Figure 3.6, from which the flux values on different segments of the circuit can be calculated as:

$$\varphi_{ab} = (V_a - V_b) \cdot P \tag{3.55}$$

where φ_{ab} represents the flux value flowing from node *a* to node *b* in the MEC, *P* is the permeance calculated as in (3.18), while V_a and V_b represent the magnetic potentials on nodes *a* and *b*.

Each permeance presented in Figure 3.6 is considered as representing one segment of the SynRM iron. The volume V_i adopted in (3.50) and (3.51) can be calculated based on such segmentation.

After all the losses of the SynRM are computed, the efficiency can be estimated as:

$$eff = \frac{P_{em}}{P_{em} + P_{Cu} + P_{hys} + P_{eddy}} \tag{3.56}$$

where P_{em} is the electromagnetic power of the SynRM, derived by:

$$P_{em} = T_{em} \cdot \omega_m \tag{3.57}$$

where T_{em} is the electromagnetic torque calculated previously, and ω_m is the mechanical angular speed of the rotor.

The weight of the SynRM is the sum of the weights of the stator core, rotor core and the windings. Mass of the iron parts can be calculated as:

$$M_{Fe} = \sum \rho_{Fe} \cdot V_i \tag{3.58}$$

where ρ_{Fe} is the density of the stator/rotor iron, and V_i represents the volume of each machine segment as introduced previously.

Mass of the windings can be estimated by:

$$M_{Cu} = 2N_s N(w_t + l_{stack}) \cdot A_{Cu} \cdot \rho_{Cu} \tag{3.59}$$

where ρ_{Cu} is the density of the stator winding wires, and all the other parameters are denoted in the same way as in (3.49).

Torque density of the machine is usually defined as $\frac{T_{em}}{V_{motor}}$, where V_{motor} represents the volume of the machine. However, the torque density of the SynRM is defined as $\frac{T_{em}}{M_{Fe}+M_{Cu}}$ in the proposed model, as the machine volume is fixed in the proposed design optimization process, which is to be introduced in the coming chapter.

3.3 Verification of the Analytical Model of Synchronous Reluctance Machines

The accuracy and credability of the proposed analytical SynRM model is verified in this section with 2D FEA simulations. Both a SynRM with C-shaped flux barriers and another SynRM with circular flux barriers are analyzed with the proposed analytical model and the FEA approach. These two types of flux barriers are the most common designs in the prevailing SynRM geometries, thus are adequate to verify the analytical model when one compares the calculation results with the FEA simulation results, which are arguably the most accurate results achievable by simulations. The SynRM with the C-shaped flux barriers is presented in Figure 3.13, while the other one with the circular flux barriers is shown in Figure 3.14.

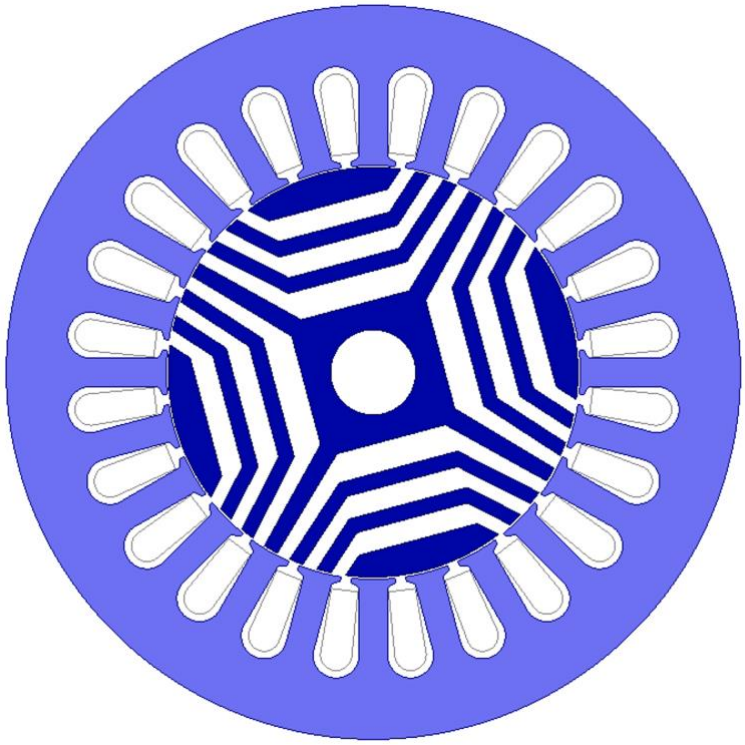

Figure 3.13 The SynRM geometry with C-shaped flux barriers.

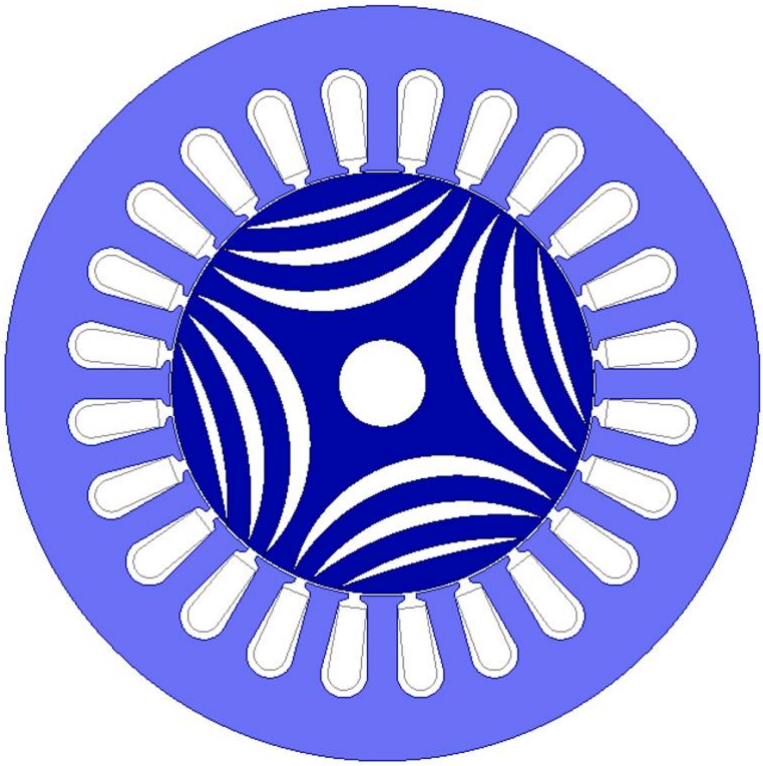

Figure 3.14 The SynRM geometry with circular flux barriers.

Both the sample SynRMs have three flux barriers on each pole, due to the conclusion that the best performance can be achieved with three flux barriers per pole for a 4-pole SynRM [96]. It is notable that both of the rotor geometries shown in Figure 3.13 and Figure 3.14 are ignoring the flux barriers, following the assumption made at the very beginning in Section 3.2.1. Such assumption simplifies the analytical model and makes it solve faster, without weakening the accuracy of the performance calculation.

3.3.1 Simulations with C-Shaped Flux Barriers

The SynRM whose geometry is presented in Figure 3.13 is analyzed in this section with both the proposed analytical model and the FEA simulation. The design parameters of the 4-pole SynRM are listed in Table 3.1.

Table 3.1 Parameters of the SynRM with C-shaped flux barriers.

Parameters	**Value**	**Parameters**	**Value**
Stator outer radius R_{sout}	100mm	l_{r1} indicated in Figure 3.5	50.55mm
Stator inner radius R_{sin}	56.4mm	l_{r2} indicated in Figure 3.5	58.54mm
Rotor outer radius R_{rout}	55.8mm	l_{r3} indicated in Figure 3.5	74.59mm
Stack length l_{stack}	68mm	l_{r4} indicated in Figure 3.5	88mm
α_1 indicated in Figure 3.5	48.5°	t_1 indicated in Figure 3.5	8.63mm
α_2 indicated in Figure 3.5	8.4°	t_2 indicated in Figure 3.5	4.09mm
α_3 indicated in Figure 3.5	8.1°	t_3 indicated in Figure 3.5	4.09mm
α_4 indicated in Figure 3.5	8.4°	t_4 indicated in Figure 3.5	9.1mm
β_1 indicated in Figure 3.5	28.45°	Stator yoke thickness	16mm
β_2 indicated in Figure 3.5	8.25°	Stator tooth width	7.85mm
β_3 indicated in Figure 3.5	8.25°	Stator slot opening	3.1°
b_1 indicated in Figure 3.5	6.1mm	Phase current peak value	4A
b_2 indicated in Figure 3.5	6.1mm	Slots per pole per phase q	2
b_3 indicated in Figure 3.5	7.8mm	Number of turns per coil	105
l_1 indicated in Figure 3.5	51mm	Rotational speed	1000 rpm
l_2 indicated in Figure 3.5	69.5mm	Electrical angular speed	$200\pi/3$
l_3 indicated in Figure 3.5	86.6mm	Copper wire area	$\sqrt{2}/2\text{mm}^2$

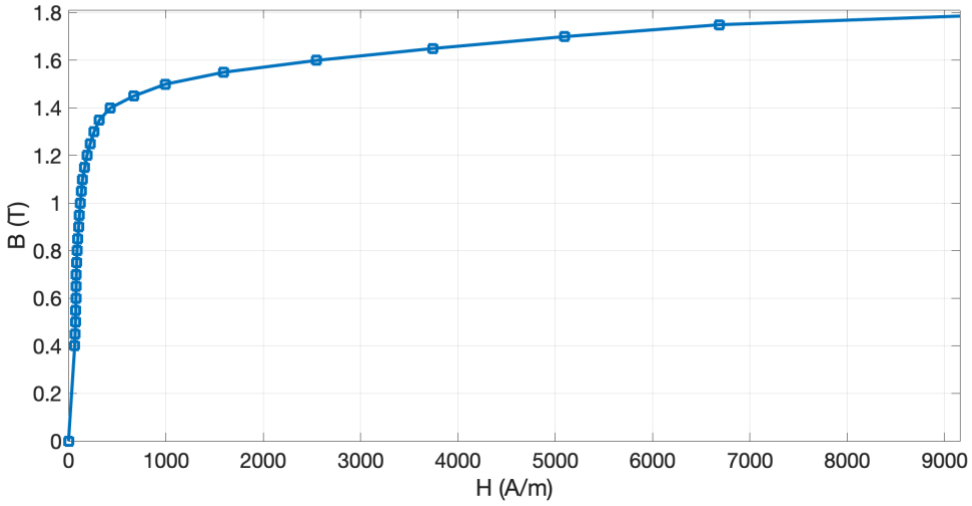

Figure 3.15 The B-H curve of the steel.

The B-H curve of the laminations used in this SynRM is presented in Figure 3.15. The air-gap flux density of the SynRM can thus be calculated by the analytical model from the given design parameters and the B-H curve of the stator/rotor iron. Figure 3.16 shows the radial flux density profiles at the middle of the air-gap calculated by the analytical model and FEA simulation at the time $t = 0$. The rotor angle θ_0, which is the electrical angle (in radians) between the winding phase *a* symmetry axis and the rotor *q* axis when time *t* equals zero, is set to be zero.

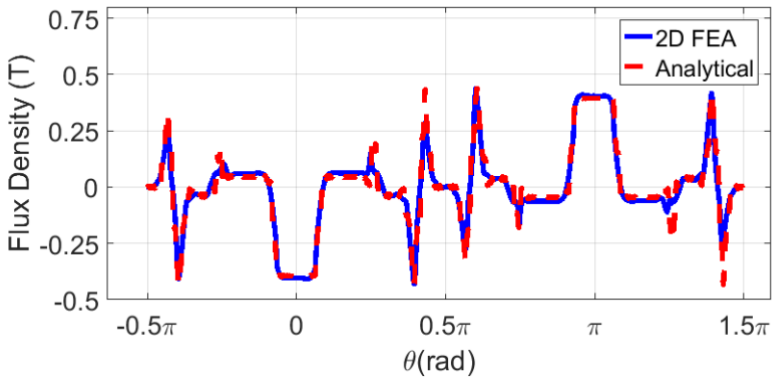

Figure 3.16 The flux density profile with $\theta_0 = 0$ and $t = 0$.

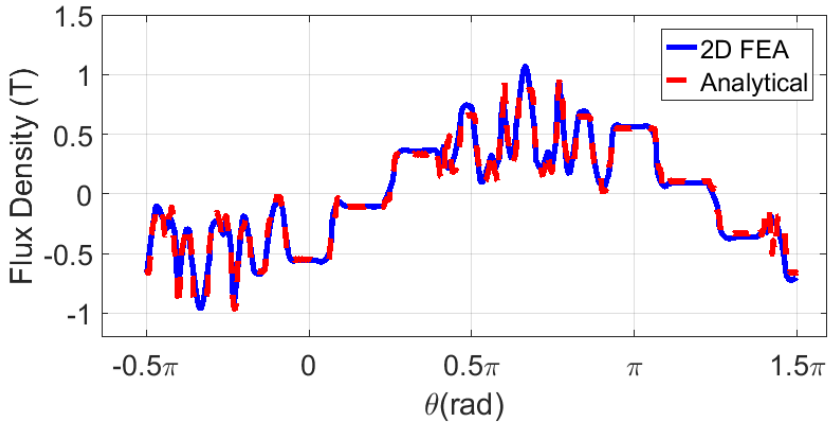

Figure 3.17 The flux density profile with $\theta_0 = \pi/6$ and $t = 0$.

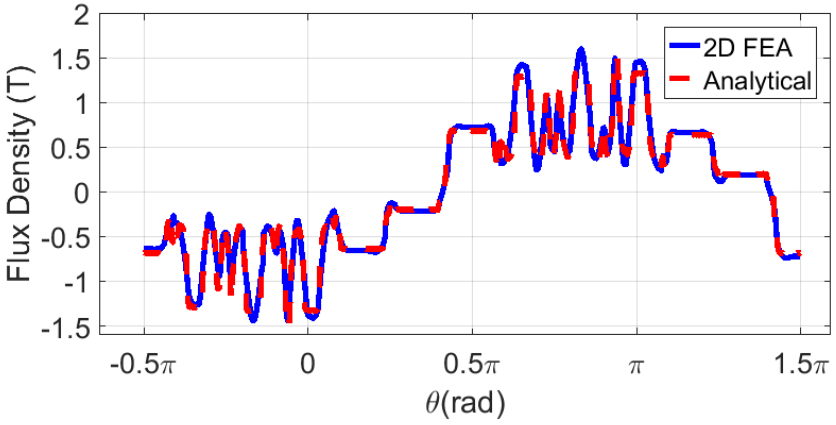

Figure 3.18 The flux density profile with $\theta_0 = \pi/3$ and $t = 0$.

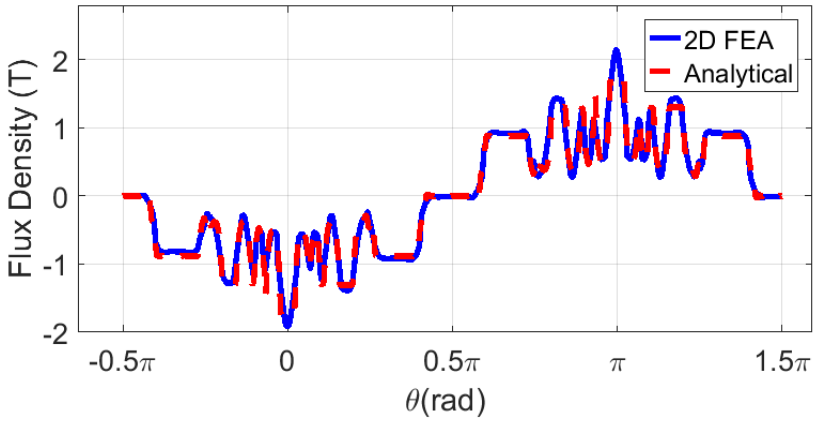

Figure 3.19 The flux density profile with $\theta_0 = \pi/2$ and $t = 0$.

The flux density profiles calcualted from the analytical model and the FEA simulation under other different rotor angle θ_0 values are presented in Figure 3.17 through Figure 3.19. It is shown that satisfactory level of agreement is achieved between the results obtained by the proposed analytical model and the FEA tool. With the FEA simulation results chosen as the reference data, the mean square error (MSE) of the results calculated by the analytical model are listed in Table 3.2. The small MSEs further prove the accuracy of the proposed analytical method.

Table 3.2 The mean square errors of the flux density values calculated by the analytical model at different rotor angles.

Rotor Angle θ_0	**Mean Square Error**
0	0.0016
$\pi/6$	0.0048
$\pi/3$	0.0083
$\pi/2$	0.0107

The time t value is then adjusted in order to prove that the analytical model can calculate the air-gap flux density values correctly at different time points as the rotor rotates. The value of the rotor angle θ_0 is fixed at $\pi/4$, where maximum torque is achieved on the SynRM. The flux density profiles calcualted from the analytical model and the FEA simulation are presented in Figure 3.20 through Figure 3.25, and the MSE of the results calculated by the analytical model are listed in Table 3.3.

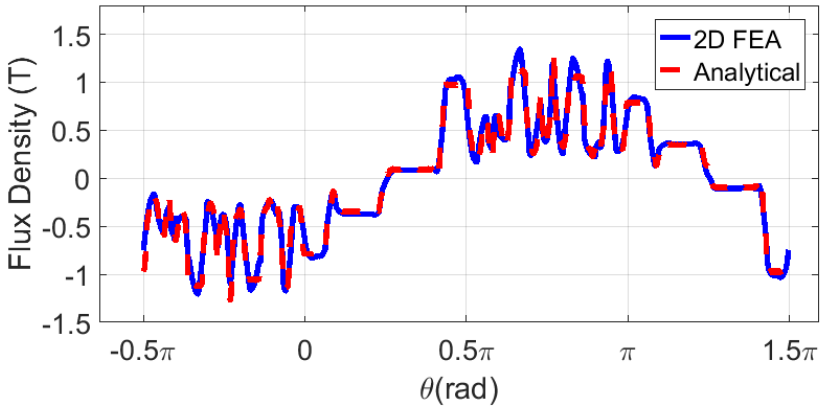

Figure 3.20 The flux density profile with $\theta_0 = \pi/4$ and $t = 0$ms.

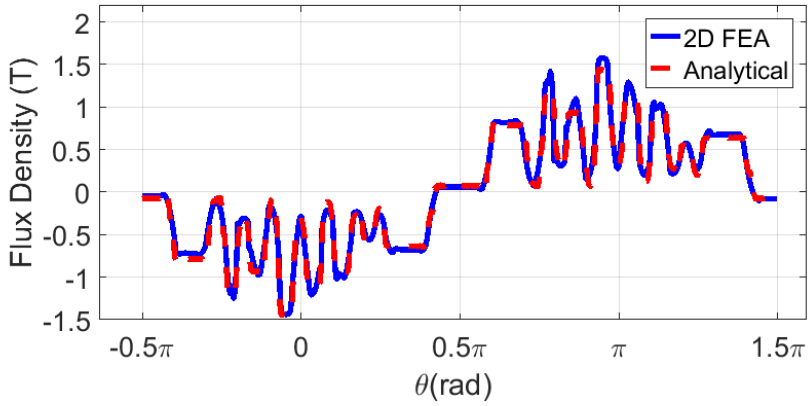

Figure 3.21 The flux density profile with $\theta_0 = \pi/4$ and $t = 3$ms.

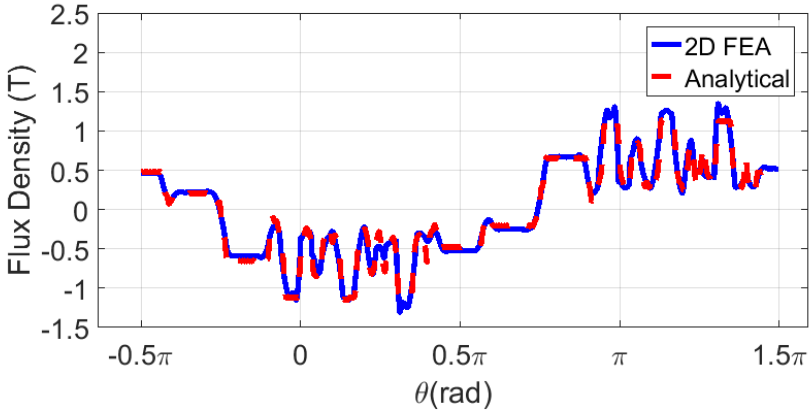

Figure 3.22 The flux density profile with $\theta_0 = \pi/4$ and $t = 6$ms.

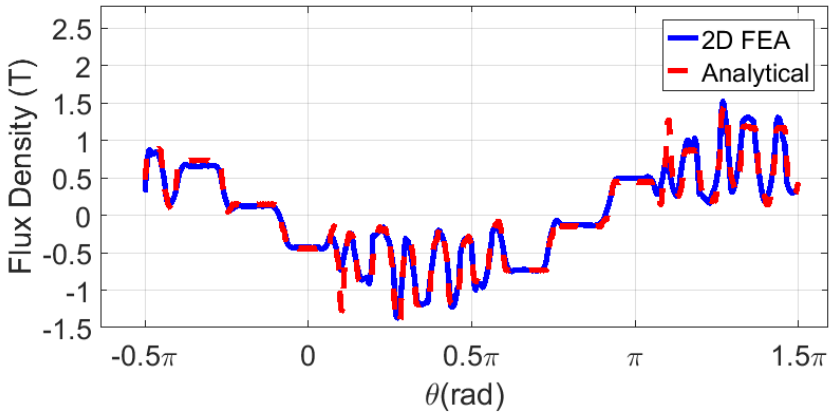

Figure 3.23 The flux density profile with $\theta_0 = \pi/4$ and $t = 9$ms.

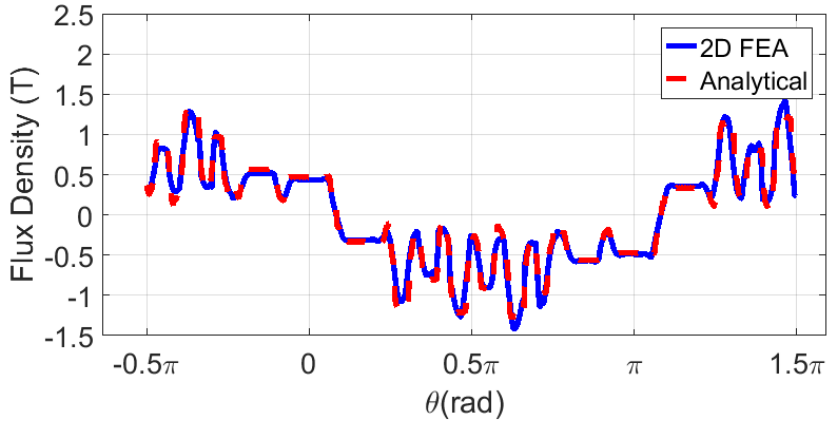

Figure 3.24 The flux density profile with $\theta_0 = \pi/4$ and $t = 12$ms.

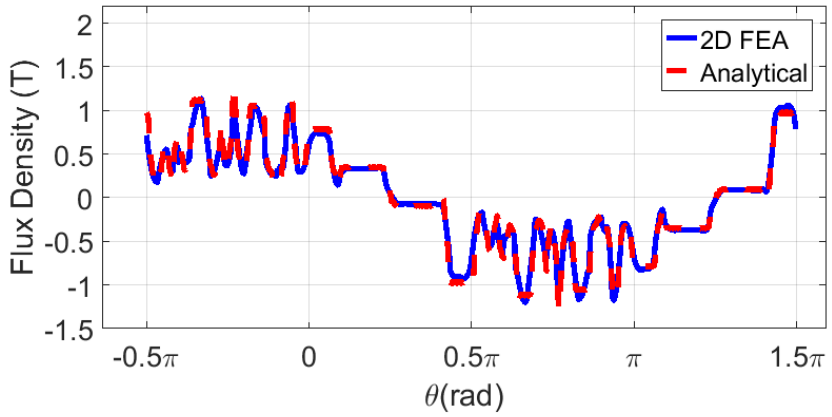

Figure 3.25 The flux density profile with $\theta_0 = \pi/4$ and $t = 15$ms.

Table 3.3 The mean square errors of the flux density values calculated by the analytical model at different time points.

Time point *t*	**Mean Square Error**
0ms	0.0055
3ms	0.0076
6ms	0.0074
9ms	0.0106
12ms	0.0085
15ms	0.0073

Table 3.4 Performance indices of the SynRM calculated by the analytical model and the FEA simulation.

	Analytical Model	**FEA Simulation**	**Error**
Average Torque	9.14Nm	9.58Nm	4.6%
Eddy Current Loss	3.4W	3.1W	9.7%
Hysteresis Loss	6.8W	6.1W	11.5%
Copper Loss	81.1W		N.A.
Weight	14.4kg		N.A.
Efficiency	91.2%	91.7%	0.5%

The performance indices of the SynRM when the rotor angle $\theta_0 = \pi/4$, including the average torque, the iron losses and the efficiency, can also be calculated by the analytical model following the methods introduced in Section 3.2.3. The calculated values are listed and compared with the FEA simulation results in Table 3.4, where the copper loss and the weight are simply calculated with analytical approaches. It can be observed that the average torque is showing satisfactory agreement, while larger errors exist in the eddy current loss and hysteresis loss calculations. It is notable that the iron losses are hard to predict since they are influenced by the temperature variations as well as other complicated effects of the steel laminations. Consequently, even the FEA calculation is usually showing some discrepancies with the real tested results. Moreover, since the copper loss is the major type of the losses, some errors in the iron loss prediction will only have a minor effect on the accuracy of the efficiency calculation, as shown in the last row of Table 3.4.

Overall, the calculation results of the proposed analytial model are showing good agreement with the FEA simulation results on the SynRMs with C-shaped flux barriers.

3.3.2 Simulations with Circular Flux Barriers

Comparisons similar to those conducted in Section 3.3.1 are presented in this section on the other type of SynRM with C-shaped flux barriers, as presented in Figure 3.14. The geometric parameters of the rotor are marked in Figure 3.26, and the design parameters of the SynRM are listed in Table 3.5.

Table 3.5 Parameters of the SynRM with circular flux barriers.

Parameters	Value	Parameters	Value
Stator outer radius R_{sout}	100mm	l_{r1} indicated in Figure 3.26	40.45mm
Stator inner radius R_{sin}	56.4mm	l_{r2} indicated in Figure 3.26	58.98mm
Rotor outer radius R_{rout}	55.8mm	l_{r3} indicated in Figure 3.26	75.1mm
Stack length l_{stack}	68mm	l_{r4} indicated in Figure 3.26	93.1mm
α_1 indicated in Figure 3.26	54.3°	t_1 indicated in Figure 3.26	7.59mm
α_2 indicated in Figure 3.26	7.8°	t_2 indicated in Figure 3.26	6.24mm
α_3 indicated in Figure 3.26	5.4°	t_3 indicated in Figure 3.26	6.84mm
α_4 indicated in Figure 3.26	9.3°	t_4 indicated in Figure 3.26	9.53mm
β_1 indicated in Figure 3.26	31.33°	Stator yoke thickness	16mm
β_2 indicated in Figure 3.26	6.54°	Stator tooth width	7.85mm
β_3 indicated in Figure 3.26	7.33°	Stator slot opening	3.1°
b_1 indicated in Figure 3.26	3.0mm	Phase current peak value I_0	4A
b_2 indicated in Figure 3.26	5.0mm	Slots per pole per phase q	2
b_3 indicated in Figure 3.26	6.0mm	Number of turns per coil N_s	105
l_1 indicated in Figure 3.26	51.58mm	Rotational speed	1000 rpm
l_2 indicated in Figure 3.26	67.48mm	Electrical angular speed	$200\pi/3$
l_3 indicated in Figure 3.26	84.15mm	Copper wire area	$\sqrt{2}/2\text{mm}^2$

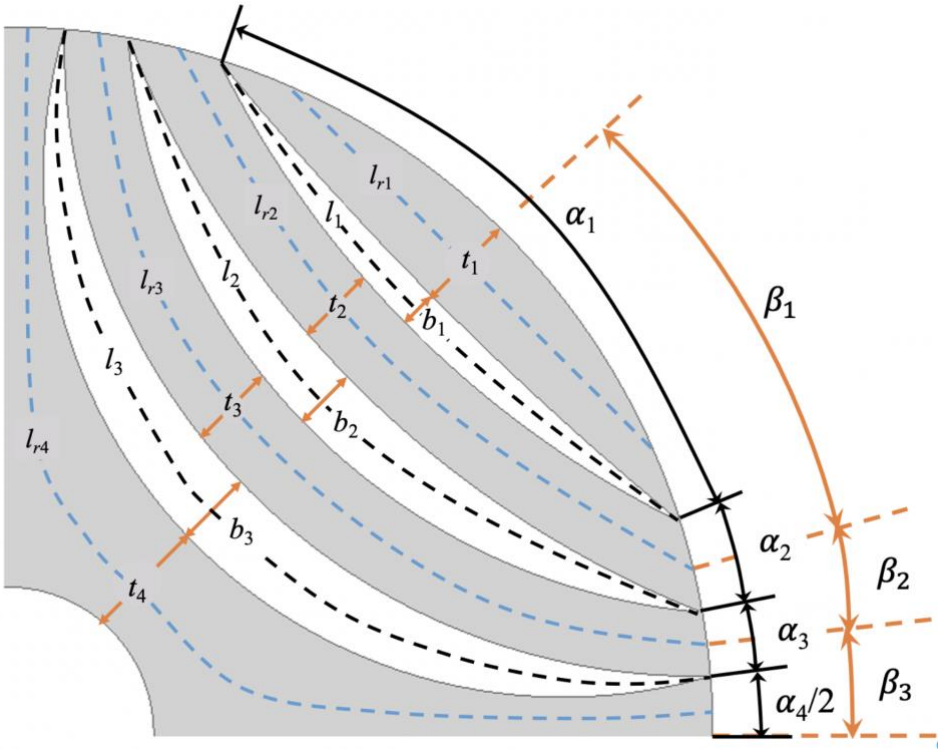

Figure 3.26 Geometric parameters of the rotor with circular flux barriers.

The B-H curve of the lamination steel is presented in Figure 3.15. Figure 3.27 shows the radial flux density profiles at the middle of the air-gap calculated by the analytical model and the FEA simulation at the time $t = 0$, with the rotor angle $\theta_0 = 0$. Flux density profiles with the time $t = 0$ and the rotor angle $\theta_0 = \pi/2$ are presented in the following Figure 3.28. The MSE of the analytical model calculation results are also listed in Table 3.6, with the FEA simulation results set as the reference data. It can be observed from the plots and the MSEs that the analytical results are showing good match with the FEA results on the SynRM with circular flux barriers, but are not as accurate as the calculations on the SynRM with the C-shaped flux barriers. This is majorly due to the existence of the large rotor surface area marked by angle α_1 in Figure 3.26. Such large region leads to magnetic potential variations on this rotor surface segment, while the

magnetic potential is assumed to be a constant value in the MEC model. The saturation effect is another reason for such inaccuracy. Even though the saturation effect is analyzed by the nonlinear MEC model, the extent of saturation varies a lot at different locations of the machine iron and cannot be precisely analyzed by the proposed segmentation used to build the MEC. However, such minor discrepancy does not affect the accuracy of the performance calculations of the analytical model. The performance indices calculated by the analytical model and the FEA simulation at $\theta_0 = \pi/4$ are compared in Table 3.7 in the same way as in Table 3.4. It is shown that the average torque calculation of the analytical model is having an acceptable error (around 5%) compared with FEA results, while the eddy current loss and the hysteresis loss are showing larger errors. Such larger rates of errors in core loss calculation are still considered to be acceptable due to the reason explained previously in Section 3.3.1. The machine efficiency estimated by the analytical model is very close to the value calculated by the FEA simulation.

The analytical model can be more accurate in calculating the flux density profile by segmenting the machine in smaller parts and building an MEC with more vertices. However, this will make the model more time-consuming to solve, and is not necessary since the originally proposed analytical model already shows its credibility in performance calculation of the SynRM.

Overall, it has been proven that the calculation results of the proposed analytial model are showing good agreement with the FEA simulation results on the SynRM with circular flux barriers.

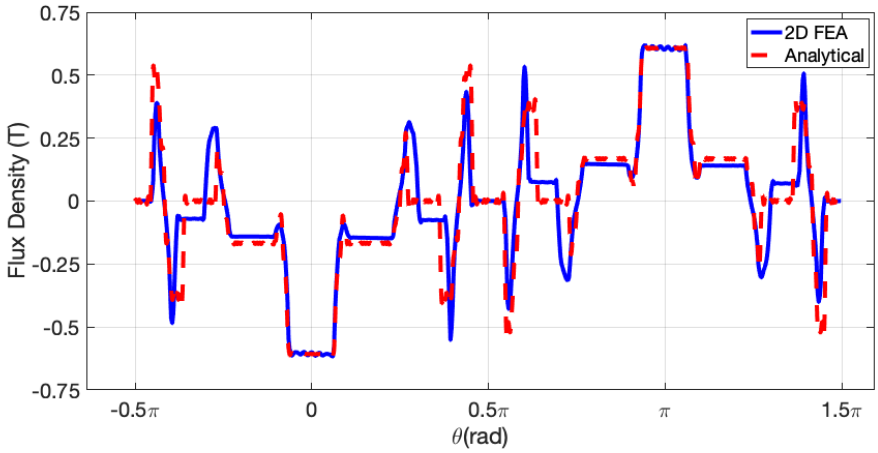

Figure 3.27 The flux density profile with $\theta_0 = 0$ and $t = 0$ for the SynRM with circular flux barriers.

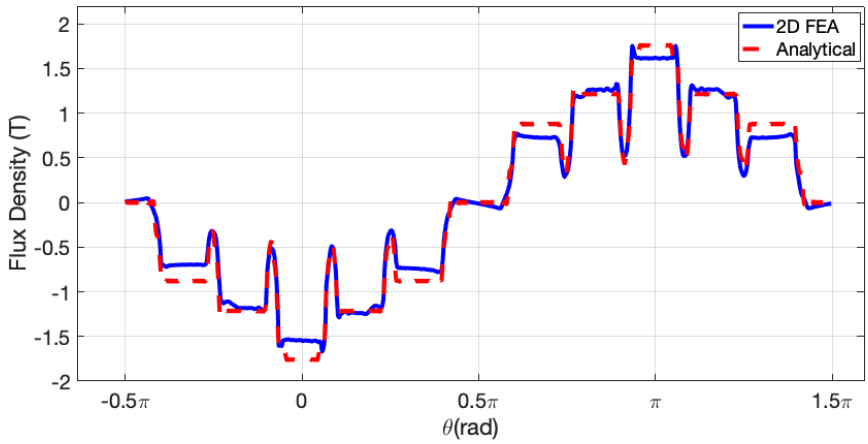

Figure 3.28 The flux density profile with $\theta_0 = \pi/2$ and $t = 0$ for the SynRM with circular flux barriers.

Table 3.6 The mean square errors of the flux density values calculated by the analytical model at different rotor angles for the SynRM with circular flux barriers.

Rotor Angle θ_0	**Mean Square Error**
0	0.0125
$\pi/2$	0.0128

Table 3.7 Performance indices of the SynRM with circular flux barriers calculated by the analytical model and the FEA simulation.

	Analytical Model	**FEA Simulation**	**Error**
Average Torque	8.74Nm	9.23Nm	5.3%
Eddy Current Loss	3.5W	3.3W	6.1%
Hysteresis Loss	7.1W	6.6W	7.6%
Copper Loss	81.1W		N.A.
Weight	15.3kg		N.A.
Efficiency	91.0%	91.4%	0.4%

3.4 Chapter Summary

This chapter introduces the basic principles of the SynRM, and presents the common topologies of the state-of-the-art SynRM designs. The proposed analytical modeling method of the SynRMs is then illustrated. The Maxwell's equations are adopted in order to solve the air-gap flux density of the SynRM, from which the average torque can be calculated. The conformal mapping technique is applied to simplify the complicated boundaries of the air-gap region, so that the boundary conditions are easier to be found. A nonlinear MEC model is proposed with the purpose of calculating the boundary condition (magnetic potential values) on the rotor surface, while the boundary condition on the stator surface is the MMF created by the stator windings.

Other performance indices such as the eddy current loss and hysteresis loss in the iron can also be calculated by the proposed analytical model. The calculation results of the analytical model, including the air-gap flux density profile, the average torque, the iron losses and the efficiency are verified by the FEA simulations on two SynRMs with different rotor designs. It is shown that the proposed analytical model can provide accurate calculation results of the performance indices for the SynRMs with common topoloties, thus is capable of serving as a SynRM design tool which is less time-consuming than the FEA simulations during the design optimization process.

CHAPTER 4. MULTI-OBJECTIVE DESIGN OPTIMIZATION OF THE SYNCHRONOUS RELUCTANCE MACHINES

The proposed analytical electro-magnetic (EM) model of the SynRM introduced in CHAPTER 3 can be synthesized with the evolutionary algorithms in order to conduct design optimization of the SynRM. With machine design parameters as inputs, the proposed analytical model is able to provide the essential performance indices (PIs) for optimization purposes, including the average torque, torque density and efficiency. Due to the mathematical complexity of the analytical model, the optimization problem is not differentiable and the classic optimization methods such as gradient descent is not applicable for such problem. Consequently, the evolutionary algorithms such as the particle swarm optimization (PSO), differential evolution (DE) and genetic algorithm (GA) are very effective candidates for finding the optimal designs based on the analytical model of the SynRM.

In order to form a multi-objective optimization (MOO) problem, one can either build the objective function by a weighted sum of various machine PIs or make the final optimal solutions converge to the Pareto front. The weighted-sum objective function provides the designer of the freedom to adjust the weights of different PIs, while the Pareto front ensures that each design on the front cannot be changed to improve one of the PIs without weakening the other PIs.

Among the most common rotor designs of the SynRMs shown in Figure 3.1, Figure 3.2 and Figure 3.3, the rotor geometry with the C-shaped flux barriers, presented in Figure

3.1, has the potential of adding permanent magnets (PMs) in the flux barriers for better performance, and is thus chosen for design optimization in this chapter.

This chapter adopts both the PSO and the DE algorithms to perform the MOO on the SynRM based on the proposed analytical model of the machine. Both algorithms converge to the Pareto front, and the Pareto fronts generated by the two algorithms are compared. One optimal SynRM design is chosen from the Pareto front for further analysis conducted by the FEA simulation. The FEA simulation results of the chosen optimal design show consistency with the analytical calculations, thus proving the effectiveness of the proposed optimal design procedure of the SynRM.

4.1 Specification of the Design Variables

Design of the SynRMs requires selections of numerous values that may include stator bore diameter, stack length, slot/pole combination, stator winding turns and wire diameter, as well as various geometry parameters. However, not all design parameters have to be optimized during the design process due to the similarity rules of machines. A new SynRM can inherit lots of specifications from an existing design, since such specifications are already proven to be feasible and optimal from the past experience. For the SynRM shown in Figure 3.1, the stator core and windings are adopted from an existing induction machine, thus are all kept unchanged during further design optimization with the purpose of reusing the existing stator laminations, coils, and machine chassis. Consequently, the number of poles is also fixed at four, and the outer diameter of the rotor remains unchanged.

Furthermore, the optimal number of flux barriers per pole is discussed in [96], yielding the conclusion that the best performance can be achieved with three flux barriers

per pole for a 4-pole SynRM. The number of rotor flux barriers per pole is thus fixed at three during the design optimization process. Centerlines of the flux barriers are also kept at the same positions as shown in Figure 3.1 and Figure 3.5, so that the flux barriers are evenly distributed along the radial direction. Moreover, the flux barriers should be parallel with each other in a typical SynRM design, which results in the situation that choosing the angle α_1 in Figure 3.5 will also determine the values of α_2 through α_4 and β_1 through β_3. Consequently, the thicknesses of the flux barriers (b_1, b_2, and b_3 marked in Figure 3.5) and the angle α_1 in Figure 3.5 are chosen as the design variables for the SynRM design optimization.

Due to the rotor geometry constraints, the upper and lower limits of the design variables have to be chosen during the design optimization. Table 4.1 lists the geometrical limits of the design variables. The upcoming sections will focus on optimizing the SynRM performance by choosing the proper values of the design variables which should be within the geometrical limits.

Table 4.1 Geometrical limits of the SynRM design variables.

Design Variables	**Limits**
b_1 in Figure 3.5	3.13mm~9.13mm
b_2 in Figure 3.5	3.13mm~9.13mm
b_3 in Figure 3.5	4.82mm~10.82mm
α_1 in Figure 3.5	34.5°~52.5°

4.2 Design Optimization Algorithms

The average torque, efficiency, and torque density (defined here as torque divided by rotor weight) are chosen as the design objectives in the multi-objective optimization process. The evolutionary algorithms have the priority in solving such problem due to the complication of the machine model. The optimal results should converge to the Pareto front, which is a set of multiple designs rather than a single optimal design. Both PSO and DE algorithms can be adopted to find the Pareto front, and the procedures of the two algorithms are introduced in this section.

4.2.1 Particle Swarm Optimization Procedure

The PSO finds the optimal solutions by mimicking each design candidate with a particle, whose location indicates the corresponding design parameters. A swarm of particles are evaluated in each iteration, and the velocities of the particles are calculated from the optimal designs in the current iteration. The swarm of particles then moves to the new locations for a certain length of time with the calculated velocities, starting a new iteration. The iterative process terminates until a clear Pareto front has been reached and none of the particles can move beyond the Pareto front.

The PSO is effective in solving problems with complicated local minima and discontinuities [97]. The procedure of the multi-objective PSO can be summarized as follows:

1）Select the parameters that need to be optimized, which are the thicknesses of the flux barriers (b_1, b_2, and b_3 marked in Figure 3.5) and the angle α_1 in Figure 3.5.

2）Select the number of particles, as well as the random initial positions and velocities of the particles.

3）Choose the dominating particles and store their positions into the repository, thus generate the Pareto front at the current iteration.

4）Randomly pick one particle from the repository as "global best" (*gbest*).

5）Systematically "fly" the particles through the solution space [97]:

a) Evaluate particle fitness: Compare to "global best" (*gbest*) and "personal best" (*pbest*);

b) Update each particle's velocity according to the relative values of *gbest* and *pbest* by the following equation:

$$v_n = \omega v_n + c_1 rand() \cdot \left(p_{best,n} - x_n\right) + c_2 rand() \cdot \left(g_{best,n} - x_n\right) \quad (4.1)$$

6）Move each particle by applying the velocity for a given time step Δt, and the position is updated to:

$$x_n = x_n + \Delta t \cdot v_n \quad (4.2)$$

7）Update the repository by eliminating dominated positions and adding dominating positions.

Steps 4) to 7) are repeated until the termination criteria are met.

During the procedure stated above, it is notable that each particle represents one possible SynRM design candidate, and the position of each particle represents the values of the design variables. Also, a dominating particle is identified if none of the other existing particles outweighs this particle in all of the three PIs, which are the torque, torque density, and efficiency in this problem. A dominated particle is then identified if there exists at least one particle that outweighs this individual in all of the three PIs.

4.2.2 The Differential Evolution Algorithm

The DE algorithm is another evolutionary optimizer which has been proved effective and is widely adopted as a reliable and fast search algorithm [98]. DE mimics the evolution of creatures, starting from a random initial population with each individual representing a specific SynRM design. Each individual in the initial population then goes through the mutation and crossover operations of DE, which finally creates a new generation of offspring. Each design in the new generation is evaluated and compared with the corresponding individual in the initial population, after which only the superior individual survives in order to remain the total population unchanged. The surviving individuals form the new population and keep going the aforementioned process until no superior individual in the offspring can be found. A multi-objective DE optimizer is developed in this research as described below:

1) Select the parameters that need to be optimized, which are the thicknesses of the flux barriers (b_1, b_2, and b_3 marked in Figure 3.5) and the angle α_1 in Figure 3.5.

2) Select the number of candidate solutions in the population, as well as the random positions of the candidates that indicate the values of the design parameters.

3) Conduct mutation and crossover operations for each individual in the initial population in order to calculate the individual's potentially new position. For the i^{th} individual with position x_i, do the following as introduced in [99]:

   a) Mutation: calculate the mutant vector by combining three different, randomly chosen agents from the population following:

$$y_i = x_a + F \cdot (x_b - x_c) \tag{4.3}$$

   where y_i is the mutant vector, x_a, x_b and x_c are the positions of the three randomly chosen agents, and F is the scale factor that controls the rate at which the population evolves.

   b) Crossover: pick a random index $k_i \in \{1, \dots, n\}$, where n is the number of the design variables, then calculate the potentially new position of the individual following:

$$z_i(j) = \begin{cases} y_i(j), & \text{if rand}(0,1) \le pCR \text{ or } j = k_i \\ x_i(j), & \text{otherwise} \end{cases} \tag{4.4}$$

where $j \in \{1, \ldots, n\}$, indicating the j^{th} element in the position coordinate, and $pCR \in [0,1]$, which is called the crossover probability.

4) Evaluate the positions z_i and x_i, and make the dominating position survive. Domination is identified if the performance of one position outweighs the other one in all the three different PIs.

Repeat steps 3) and 4) until the termination criteria are met.

4.3 Optimization Results

Both the multi-objective PSO and the multi-objective DE are conducted in this section following the procedures introduced before. The proposed analytical model of the SynRM is used to evaluate the PIs from the design variables.

The PSO is performed with a swarm of 20 particles, and 30 iterations are conducted to find the final Pareto front. The personal learning coefficient c_1 and the global learning coefficient c_2 in (4.1) are given the values of 1.5 and 2.0 respectively. The 600 designs are collected in Figure 4.1 as colored dots, and the color is indicating the current number of iterations of the corresponding design. The Pareto front obtained after the 30 iterations is plotted in Figure 4.2. The whole process takes only 14 minutes and 53 seconds on a MacBook with 2.8GHz Intel Core i7 processor and 16GB memory, thanks to the proposed fast-solving analytical model of the SynRM. Such optimization process could take hours or even days if the FEA tool is applied for evaluating the 600 designs.

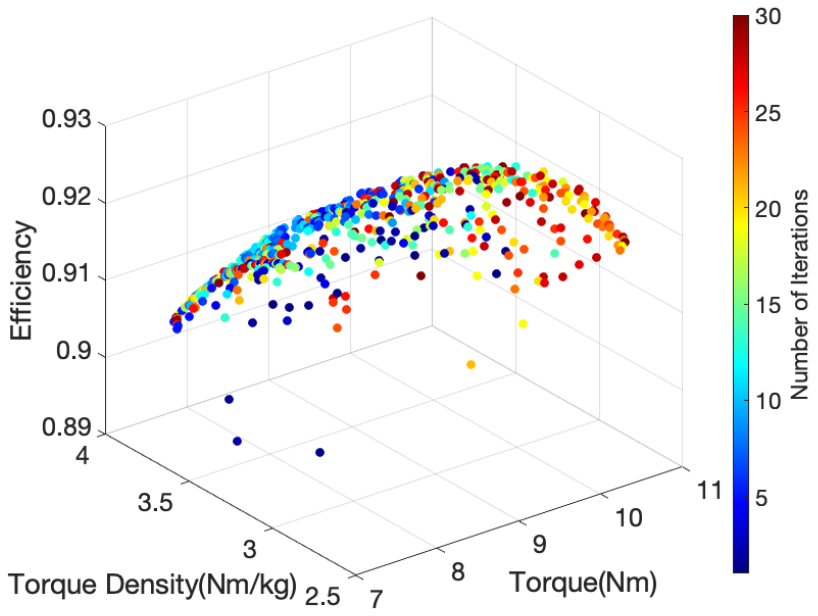

Figure 4.1 Collection of the designs emerged during the multi-objective PSO.

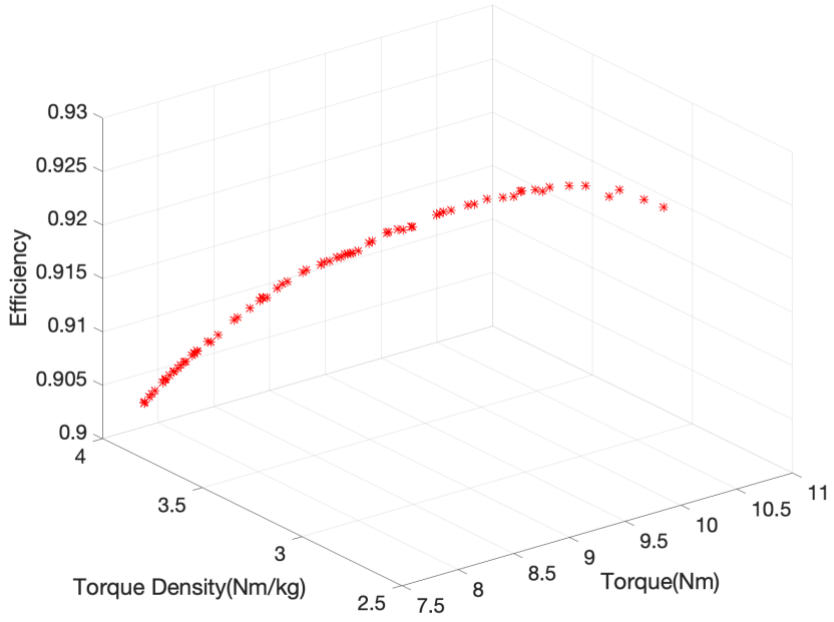

Figure 4.2 The Pareto front found by the multi-objective PSO.

The multi-objective DE is also performed based on the proposed analytical model of the SynRM. The population size is fixed at 40, and 30 iterations are conducted. The scale factor F in (4.3) is randomly chosen in the range of 0.2 to 0.8, and the crossover probability pCR in (4.4) has the value of 0.2. A collection of all the analyzed designs is presented in Figure 4.3, where the color of each dot indicates the current number of the evaluated design. Figure 4.3 plots the Pareto front, which consists of the dominating designs in the last generation. Figure 4.5 compares the Pareto fronts obtained from the PSO and the DE algorithms. It is presented that the two Pareto fronts are showing good match with each other, proving that the same optimal designs have been found by both optimizers.

It takes 34 minutes and 22 seconds on a MacBook with 2.8GHz Intel Core i7 processor and 16GB memory to conclude this process. The time consumption is higher than the PSO process due to the increased number of designs to be analyzed in this DE optimization procedure. Such increment comes from the selection of a large population and the sufficient number of iterations, which are essential for converging to the final Pareto front, while increasing the time consumption at the same time. Consequently, the population size and number of iterations should be carefully chosen in both PSO and DE optimizations in order to obtain the optimal Pareto front while reduce the time consumption.

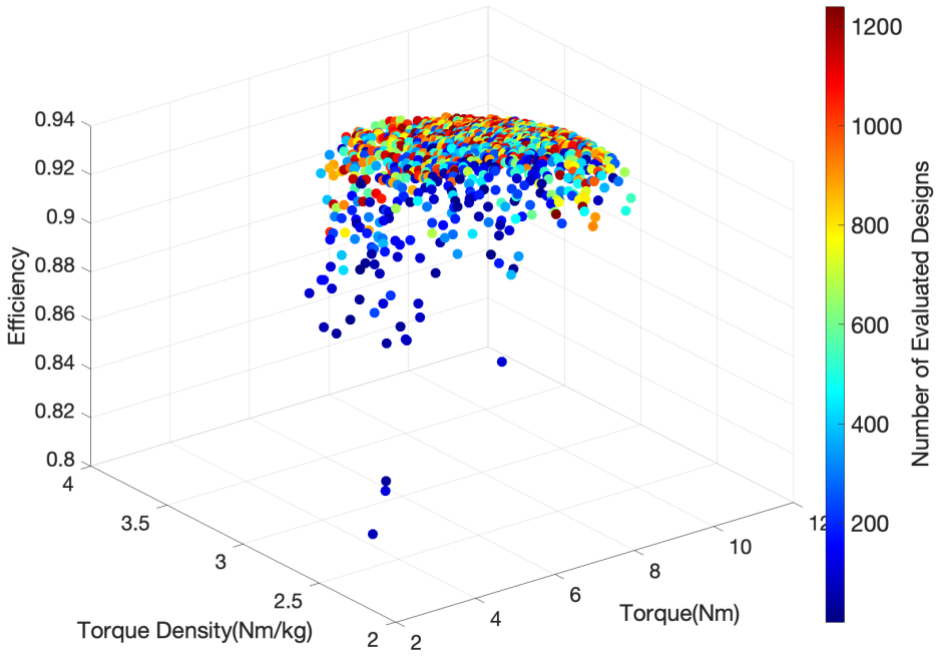

Figure 4.3 Collection of the designs emerged during the multi-objective DE.

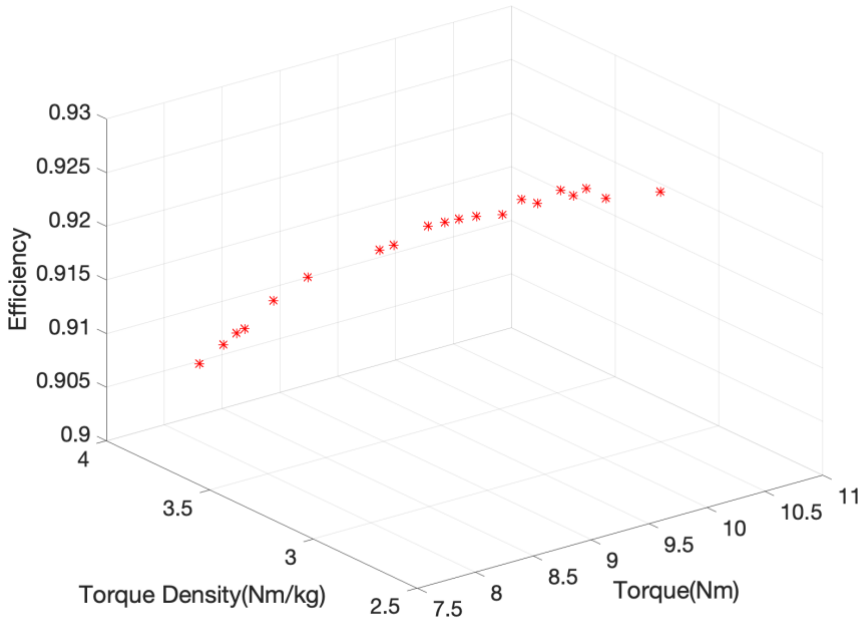

Figure 4.4 The Pareto front obtained by the multi-objective DE.

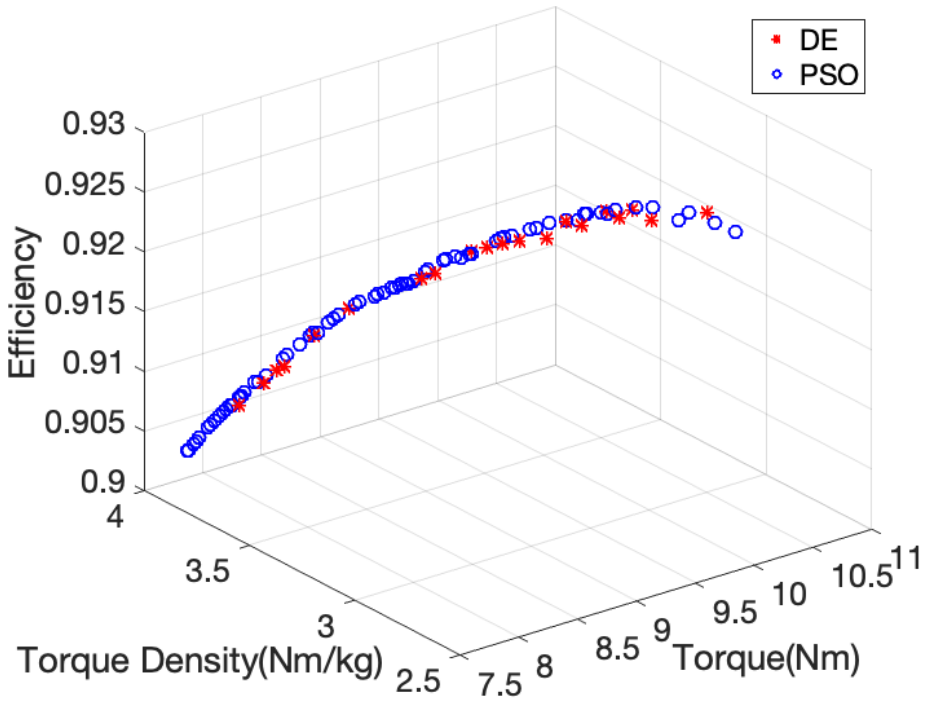

Figure 4.5 Comparison of the Pareto fronts.

The tradeoff between the computational efficiency and the quality of the Pareto front can be evaluated by conducting multiple optimizations with different numbers of iterations and different sizes of population. The PSO and DE are both conducted with the following combinations: 1) 10 individuals, 10 iterations: 100 designs to be evaluated; 2) 20 individuals, 15 iterations: 300 designs to be evaluated; 3) 20 individuals, 30 iterations: 600 designs to be evaluated. The corresponding Pareto fronts are plotted in Figure 4.6, where the Pareto front generated by PSO with 20 individuals and 30 iterations (marked as PSO600 in Figure 4.6) is considered as the reference, indicating the real Pareto front. The time consumptions of each optimizer under each combination are compared in Table 4.2.

The following conclusions can be made by observing Figure 4.6 and Table 4.2:

1) Increasing the population size and number of iterations will increase the time consumption while create a better Pareto front in both PSO and DE.

2) With the same population size and number of iterations, the PSO generally creates a better Pareto front than the DE in this SynRM design optimization problem.

3) Although the DE600 and PSO 300 Pareto fronts are both close with the PSO600 Pareto front, the last one is chosen as the set of optimal designs since its time consumption is well acceptable.

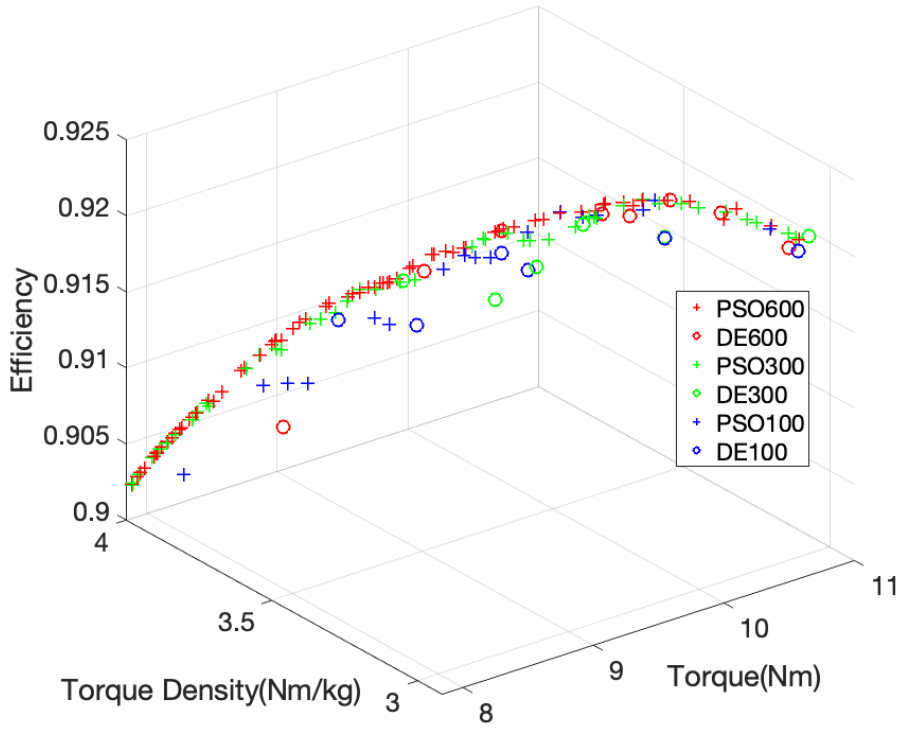

Figure 4.6 Comparison of the Pareto fronts obtained under different numbers of iterations and different sizes of population.

Table 4.2 The time consumption for creating each Pareto front.

Pareto Front	Time Consumption
PSO100	2 minutes 26 seconds
DE100	2 minutes 45 seconds
PSO300	7 minutes 35 seconds
DE300	8 minutes 10 seconds
PSO600	14 minutes 53 seconds
DE600	14 minutes 5 seconds

Two designs on the PSO600 Pareto front (also plotted in Figure 4.2) are chosen for further validation. Design I focuses on improving the average toque and the efficiency, while Design II aims at increasing the torque density, which generally reduces the weight of the SynRM. The two designs are both marked on the Pareto front in Figure 4.7.

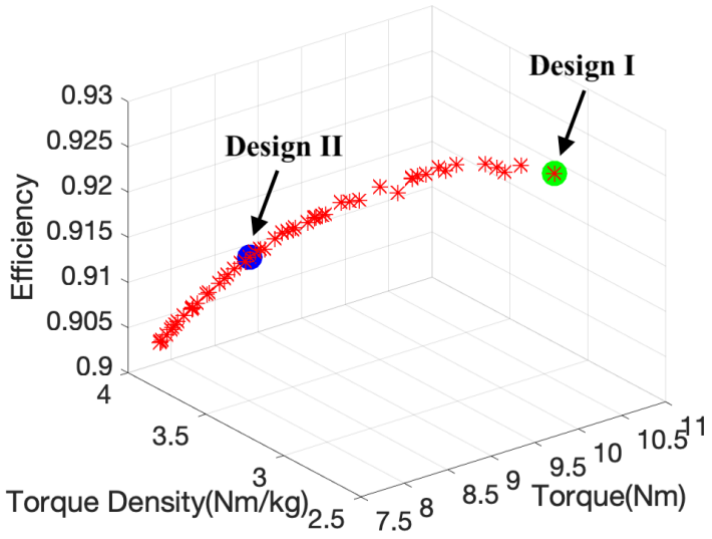

Figure 4.7 The two chosen designs on the Pareto front.

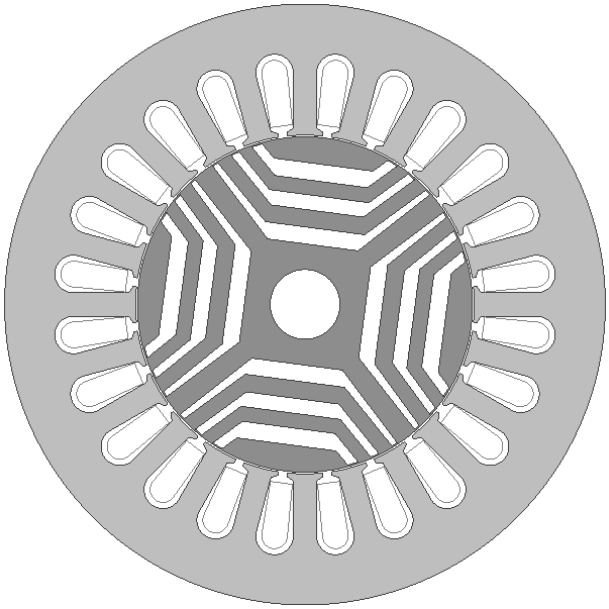

Figure 4.8 Geometry of the SynRM Design I.

The SynRM geometry of Design I is presented in Figure 4.8. FEA simulation is operated on this design to calculate the PIs, and the results are listed in Table 4.3. It can be concluded that the PIs calculated by the analytical model and the FEA simulation show good match with each other, and the optimized Design I outweighs the original design in terms of the average torque and the efficiency. Detailed parameters of Design I are provided in Table 4.4, while parameters of the original design are listed in Table 3.1.

Table 4.3 Design I performance indices calculated by FEA and analytical model, compared with the original design.

	Analytical	**FEA**	**Error**	***Original Design***
Average Torque	10.63Nm	10.03Nm	6.0%	*9.58Nm*
Torque Density (Average Torque/Rotor Weight)	3.0Nm/kg	2.84Nm/kg	5.6%	3.53Nm/kg
Efficiency	92.2%	92.1%	0.1%	*91.7%*

Table 4.4 Parameters of Design I.

Parameters	Value	Parameters	Value
Stator outer radius R_{sout}	100mm	l_{r1} indicated in Figure 3.5	50.55mm
Stator inner radius R_{sin}	56.4mm	l_{r2} indicated in Figure 3.5	58.54mm
Rotor outer radius R_{rout}	55.8mm	l_{r3} indicated in Figure 3.5	74.59mm
Stack length l_{stack}	68mm	l_{r4} indicated in Figure 3.5	88mm
α_1 indicated in Figure 3.5	45.4°	t_1 indicated in Figure 3.5	8.82mm
α_2 indicated in Figure 3.5	8.4°	t_2 indicated in Figure 3.5	4.85mm
α_3 indicated in Figure 3.5	8.1°	t_3 indicated in Figure 3.5	5.71mm
α_4 indicated in Figure 3.5	11.7°	t_4 indicated in Figure 3.5	10.2mm
β_1 indicated in Figure 3.5	26.9°	Stator yoke thickness	16mm
β_2 indicated in Figure 3.5	8.25°	Stator tooth width	7.85mm
β_3 indicated in Figure 3.5	8.25°	Stator slot opening	3.1°
b_1 indicated in Figure 3.5	5.72mm	Phase current peak value	4A
b_2 indicated in Figure 3.5	5.0mm	Slots per pole per phase q	2
b_3 indicated in Figure 3.5	5.6mm	Number of turns per coil	105
l_1 indicated in Figure 3.5	51mm	Rotational speed	1000 rpm
l_2 indicated in Figure 3.5	69.5mm	Electrical angular speed	$200\pi/3$
l_3 indicated in Figure 3.5	86.6mm	Copper wire area	$\sqrt{2}/2\text{mm}^2$

Table 4.5 Design II performance indices calculated by FEA and analytical model, compared with the original design.

	Analytical	**FEA**	**Error**	***Original Design***
Average Torque	8.72Nm	9.2Nm	5.2%	*9.58Nm*
Torque Density (Average Torque/Rotor Weight)	3.90Nm/kg	4.11Nm/kg	5.4%	3.53Nm/kg
Efficiency	91.0%	91.5%	0.5%	*91.7%*

Table 4.5 compares the analytical and FEA calculation results of Design II, with the PIs of the original design listed in the last column. It is again proved that the analytical calculation results match well with the FEA simulation, and the torque density of Design II outweighs the original design as expected. The geometry of Design II and the detailed parameters are presented in Figure 4.9 and Table 4.6 respectively.

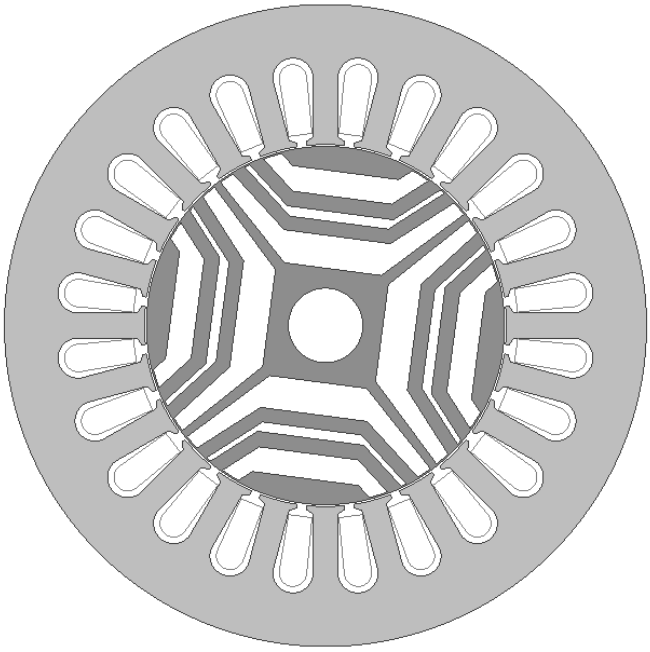

Figure 4.9 Geometry of the SynRM Design II.

Table 4.6 Parameters of Design II.

Parameters	Value	Parameters	Value
Stator outer radius R_{sout}	100mm	l_{r1} indicated in Figure 3.5	50.55mm
Stator inner radius R_{sin}	56.4mm	l_{r2} indicated in Figure 3.5	58.54mm
Rotor outer radius R_{rout}	55.8mm	l_{r3} indicated in Figure 3.5	74.59mm
Stack length l_{stack}	68mm	l_{r4} indicated in Figure 3.5	88mm
α_1 indicated in Figure 3.5	52.5°	t_1 indicated in Figure 3.5	7.74mm
α_2 indicated in Figure 3.5	8.4°	t_2 indicated in Figure 3.5	4.73mm
α_3 indicated in Figure 3.5	8.1°	t_3 indicated in Figure 3.5	4.41mm
α_4 indicated in Figure 3.5	4.4°	t_4 indicated in Figure 3.5	7.9mm
β_1 indicated in Figure 3.5	30.45°	Stator yoke thickness	16mm
β_2 indicated in Figure 3.5	8.25°	Stator tooth width	7.85mm
β_3 indicated in Figure 3.5	6.25°	Stator slot opening	3.1°
b_1 indicated in Figure 3.5	7.9mm	Phase current peak value	4A
b_2 indicated in Figure 3.5	3.1mm	Slots per pole per phase q	2
b_3 indicated in Figure 3.5	10.2mm	Number of turns per coil	105
l_1 indicated in Figure 3.5	51mm	Rotational speed	1000 rpm
l_2 indicated in Figure 3.5	69.5mm	Electrical angular speed	$200\pi/3$
l_3 indicated in Figure 3.5	86.6mm	Copper wire area	$\sqrt{2}/2\text{mm}^2$

4.4 Chapter Summary

This chapter conducts both PSO and DE in order to achieve optimal designs of the SynRM based on the analytical model proposed in CHAPTER 3. Performance indices including the average torque, torque density and efficiency are considered. The multi-objective optimization converges to the Pareto front, which is a set of multiple optimal designs. It is shown that the number of iterations and the size of the population affects the Pareto front when using PSO and DE optimizers. Such relation is then presented and discussed in this chapter.

Two optimal designs focusing on different PIs are chosen from the Pareto front as feasible optimal design candidates. Their PIs are validated by FEA simulation, which again proves the accuracy of the analytical SynRM model.

CHAPTER 5. DESIGN OPTIMIZATION OF THE SINGLE-PHASE INDUCTION MACHINES

Similar to the design optimization of the SynRMs, analytical models are also desired during the design optimization process of the single-phase induction machines (IMs), as introduced in Chapters 1 and 2. The evolutionary algorithms can be used to find the optimal designs based on the fast-solving analytical model, after which the more time-consuming FEA simulations can be performed to refine the final optimal design.

This chapter starts with an introduction of the working principles and the common types of the single-phase IMs. The equivalent circuit model is then presented in order to calculate the performance indices (PIs) of the capacitor-run single-phase IM. The particle swarm optimization (PSO) algorithm is conducted based on the equivalent circuit model, so as to obtain the optimal designs. Two optimal designs focusing on improving different PIs are finally chosen for validation by the FEA simulations, which proves the improvement of the PIs and the reliability of the design optimization method.

5.1 Basic Principles of the Single-Phase Induction Machines

The 2-D geometry of a single-phase IM with a caged rotor is presented in Figure 5.1, and it can be observed that the single-phase IMs have very similar geometries as the three-phase IMs. The rotor of the single-phase IM can be either caged or wire-wound, same as the three-phase IM, while the AC power fed into the stator windings should have only a single phase. The single-phase AC current is directly fed into the stator main winding, creating a pulsing magnetic field, which can be decomposed into a forward-rotating field

and a backward-rotating field. The two rotating fields can then create a forward and a backward torque on the rotor with short-circuit windings, in the same way as the three-phase IMs. Consequently, the torque-speed curve of the single-phase IM can be plotted by superposing the forward and backward torque-speed curves of the three-phase IM, as presented by the solid curve in Figure 5.2 [100].

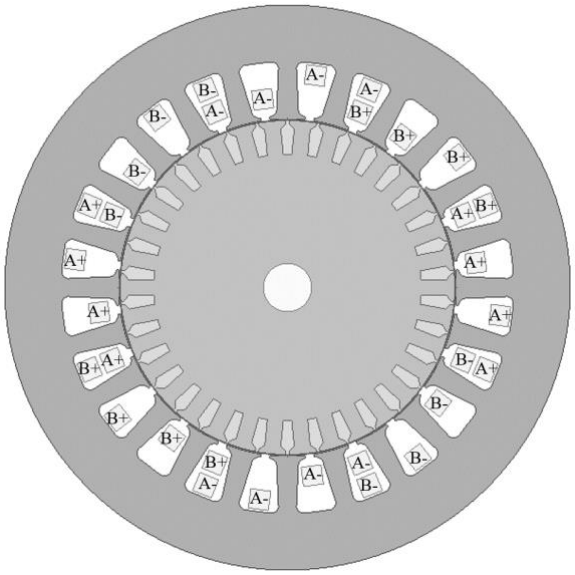

Figure 5.1 2-D geometry of a typical single-phase IM.

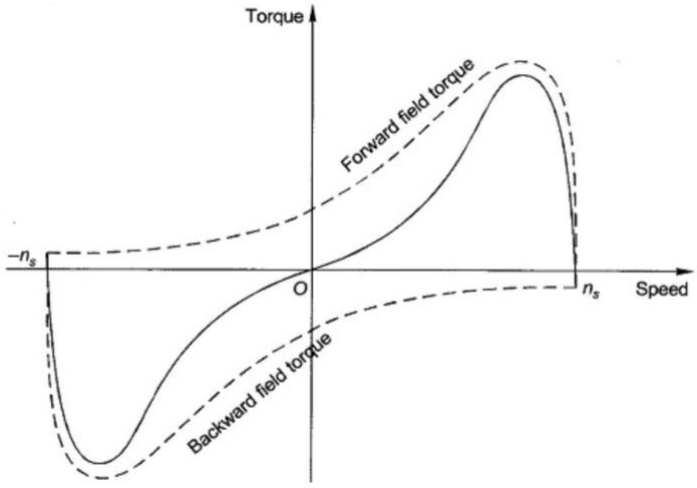

Figure 5.2 Torque-speed curve of the single-phase IM [100].

It is obvious from the torque-speed curve in Figure 5.2 that the starting torque of the single-phase IM is zero. In order to make the machine have self-start ability, the auxiliary winding is usually added in the stator. The auxiliary winding is orthogonal with the main winding, and is connected in series with a phase-shifting capacitor. The capacitor shifts the phase angle of the magnetomotive force (MMF) produced by the auxiliary winding, even though the power supply connected to the machine has only one single phase. Consequently, the orthogonal windings with MMFs in different phases will create a rotating magnetic field in the air-gap, which would produce the starting torque on the rotor.

The auxiliary winding together with the capacitor can be cut off from the power supply when the rotor reaches a certain speed, making a capacitor-start single-phase IM. Such machines usually have high starting torque, since the auxiliary winding and the capacitor value are optimized in order to improve the starting performance. The auxiliary winding and the capacitor can also be connected at all times from start to normal operation, making a capacitor-run single-phase IM. Such machine may not have a very high starting torque, but usually has a higher efficiency and better torque performance during normal operation. A capacitor-start-capacitor-run single-phase IM can be made by using different capacitor values during the start and normal operation statuses. Such machines can achieve good starting torque as well as high efficiency, but are subject to more complicated design procedures.

This chapter focuses on modeling and optimizing the capacitor-run single-phase IMs. Consequently, the average torque, efficiency and the power factor are the essential performance indices (PIs) during the design optimization process.

5.2 The Analytical Model of the Capacitor-Run Machines

This section describes the analytical model of the capacitor-run single-phase IMs that have two sets of working windings during normal operation. Each winding generates a pulsing MMF that can be decomposed into a forward rotating wave and a backward rotating wave. Consequently, the single-phase IM can be modeled with four equivalent circuits [101], two of which represent the forward and backward components of the main phase, while the other two represent the forward and backward components of the auxiliary phase. The equivalent circuits can be used to analyze the PIs of the single-phase IM, and the parameters of the equivalent circuits can be calculated from the machine design parameters. The analytical model should be able to calculate the machine PIs from the design parameters, so as to be used during the design optimization process for finding the optimal designs.

5.2.1 The Equivalent Circuits of the Single-Phase Induction Machines

The aforementioned four equivalent circuits are presented in Figure 5.3. The circuits shown in Figure 5.4 are equivalent to the circuits in Figure 5.3, after one combines their impedances. It is obvious that R_{1m}, X_{1m}, R_{2m}, and X_{2m} represent the resistances and the leakage reactances of the main phase, where R_{2m} and X_{2m} are the equivalent rotor values that can be seen from the stator. X_u represents the magnetizing reactance of the main phase whose resistance is neglected. Similarly, R_{1a}, X_{1a}, R_{2a}, X_{2a} and X_{ua} represent the parameters of the auxiliary phase, and R_C and X_C are the resistance and the reactance of the capacitor. The next section will introduce the performance calculation of the SPIM, based on the equivalent circuits.

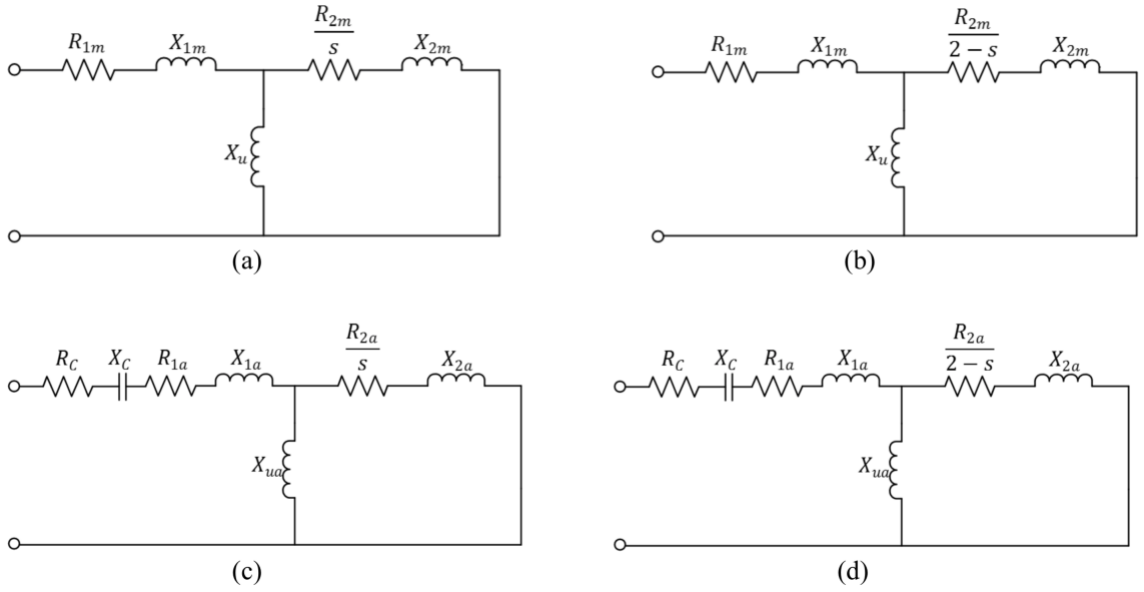

Figure 5.3 The equivalent circuits of the single-phase IM: (a) Main phase forward; (b) Main phase backward; (c) Auxiliary phase forward; (d) Auxiliary phase backward.

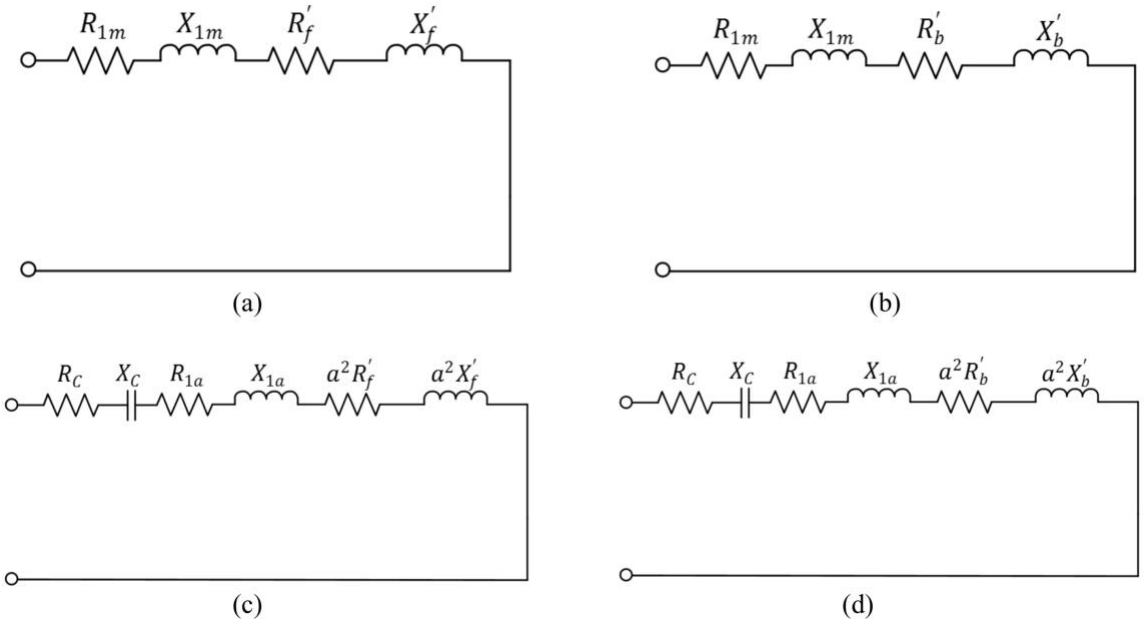

Figure 5.4 The simplified equivalent circuits of the single-phase IM: (a) Main phase forward; (b) Main phase backward; (c) Auxiliary phase forward; (d) Auxiliary phase backward.

5.2.2 Performance Calculation Based on the Equivalent Circuits

The equivalent circuits presented in Figure 5.4 are used for deriving the PIs of the capacitor-run single-phase IM in this section, following the procedures in [101]. The following values are defined in order to simplify the equations during the performance calculation:

$$R_f = 0.5R_f' \tag{5.1}$$

$$X_f = 0.5X_f' \tag{5.2}$$

$$R_b = 0.5R_b' \tag{5.3}$$

$$X_b = 0.5X_b' \tag{5.4}$$

The main phase voltage can be expressed as:

$$\dot{U} = \dot{U}_m^+ + \dot{U}_m^- = \dot{I}_m(R_T + jX_T) - j\dot{I}_a\left[a\left(R_f - R_b\right) + ja\left(X_f - X_b\right)\right] \tag{5.5}$$

where $\dot{U}_m^+$ and $\dot{U}_m^-$ are the forward and backward components of the main phase voltage, $\dot{I}_m$ and $\dot{I}_a$ are the current in the main winding and the auxiliary winding respectively, a is the turns ratio between the auxiliary winding and the main winding, and:

$$R_T = R_{1m} + R_f + R_b \tag{5.6}$$

$$X_T = X_{1m} + X_f + X_b \tag{5.7}$$

The auxiliary phase voltage can be expressed as:

$$\dot{U} = \dot{U}_a^+ + \dot{U}_a^- = \dot{I}_a(R_{Ta} + jX_{Ta}) + j\dot{I}_m\left[a\left(R_f - R_b\right) + ja\left(X_f - X_b\right)\right] \quad (5.8)$$

where $\dot{U}_a^+$ and $\dot{U}_a^-$ are the forward and backward components of the auxiliary phase voltage, and:

$$R_{Ta} = a^2 R_T + R_C \quad (5.9)$$

$$X_{Ta} = a^2 X_T - X_C \quad (5.10)$$

Solving (5.5) and (5.8) yields:

$$\dot{I}_m = R_5 + jX_5 \quad (5.11)$$

where R_5 and X_5 are representing the real and imaginary values of $\dot{I}_m$, and their values are calculated as follows:

$$R_5 = R_4\left[R_{Ta} - a\left(X_f - X_b\right)\right] + X_4\left[X_{Ta} + a\left(R_f - R_b\right)\right] \quad (5.12)$$

$$X_5 = R_4\left[X_{Ta} + a\left(R_f - R_b\right)\right] - X_4\left[R_{Ta} - a\left(X_f - X_b\right)\right] \quad (5.13)$$

$$R_4 = \frac{R_3 U}{R_3^2 + X_3^2} \quad (5.14)$$

$$X_4 = \frac{X_3 U}{R_3^2 + X_3^2} \quad (5.15)$$

$$R_3 = (R_T R_{Ta} - X_T X_{Ta}) - a^2\left[\left(R_f - R_b\right)^2 - \left(X_f - X_b\right)^2\right] \quad (5.16)$$

$$X_3 = (R_T X_{Ta} - X_T R_{Ta}) - 2a^2(R_f - R_b)\big(X_f - X_b\big) \tag{5.17}$$

$\dot{I}_a$ can be similarly expressed as:

$$\dot{I}_a = R_6 + jX_6 \tag{5.18}$$

where

$$R_6 = R_4\big[R_T + a\big(X_f - X_b\big)\big] + X_4\big[X_T - a\big(R_f - R_b\big)\big] \tag{5.19}$$

$$X_6 = R_4\big[X_T - a\big(R_f - R_b\big)\big] - X_4\big[R_T + a\big(X_f - X_b\big)\big] \tag{5.20}$$

Hence, the input power can be calculated as:

$$P_1 = U_1(R_5 + R_6) + P_{Fe1} \tag{5.21}$$

where U_1 is the phase voltage, and P_{Fe1} represents the iron loss in the stator.

The output power can be derived and simplified into the following equation:

$$\begin{aligned} P_2 = \big\{[I_m^2 + (aI_a)^2]\big(R_f - R_b\big) + 2a(R_5X_6 - X_5R_6)\big(R_f + R_b\big)\big\}(1 - s) \\ - (P_{mech} + P_{Fe2}) \end{aligned} \tag{5.22}$$

where P_{mech} is the mechanical loss, and P_{Fe2} is the rotor iron loss.

It is now obvious that the efficiency and the torque of the motor can be calculated as:

$$\eta = \frac{P_2}{P_1} \tag{5.23}$$

$$T_{out} = \frac{P_2}{\omega_m} \tag{5.24}$$

where ω_m is the rotational speed of the rotor.

Other performance indices (PIs) of the single-phase IM, including the rated slip, the rated power factor, the weight, the starting torque and the maximum torque, can all be calculated from the equivalent circuits as introduced in [101]. The procedure can be summarized in the flow chart presented in Figure 5.5. The calculations start from specifying the given design requirements and the basic machine parameters. The design requirements usually include the output power, the phase voltage, the number of poles and the efficiency. The basic machine parameters such as the bore diameter, the air-gap length, the rotor/stator slot numbers, the core length and the type of steel should also be selected at the beginning of the design process. All the other machine geometric parameters such as the slot, tooth and yoke geometries can then be calculated from these values.

The air-gap flux density B_δ and the saturation index K_S should then be assumed so as to calculate the total number of turns of the main winding with the following equation:

$$Z_m = \frac{U_1 K_E}{K_{WM} K_B \varphi} \tag{5.25}$$

where K_{WM} represents the winding factor, φ is the flux per pole, K_E stands for the distortion index of the voltage waveform, and K_B stands for the distortion index of the flux density waveform.

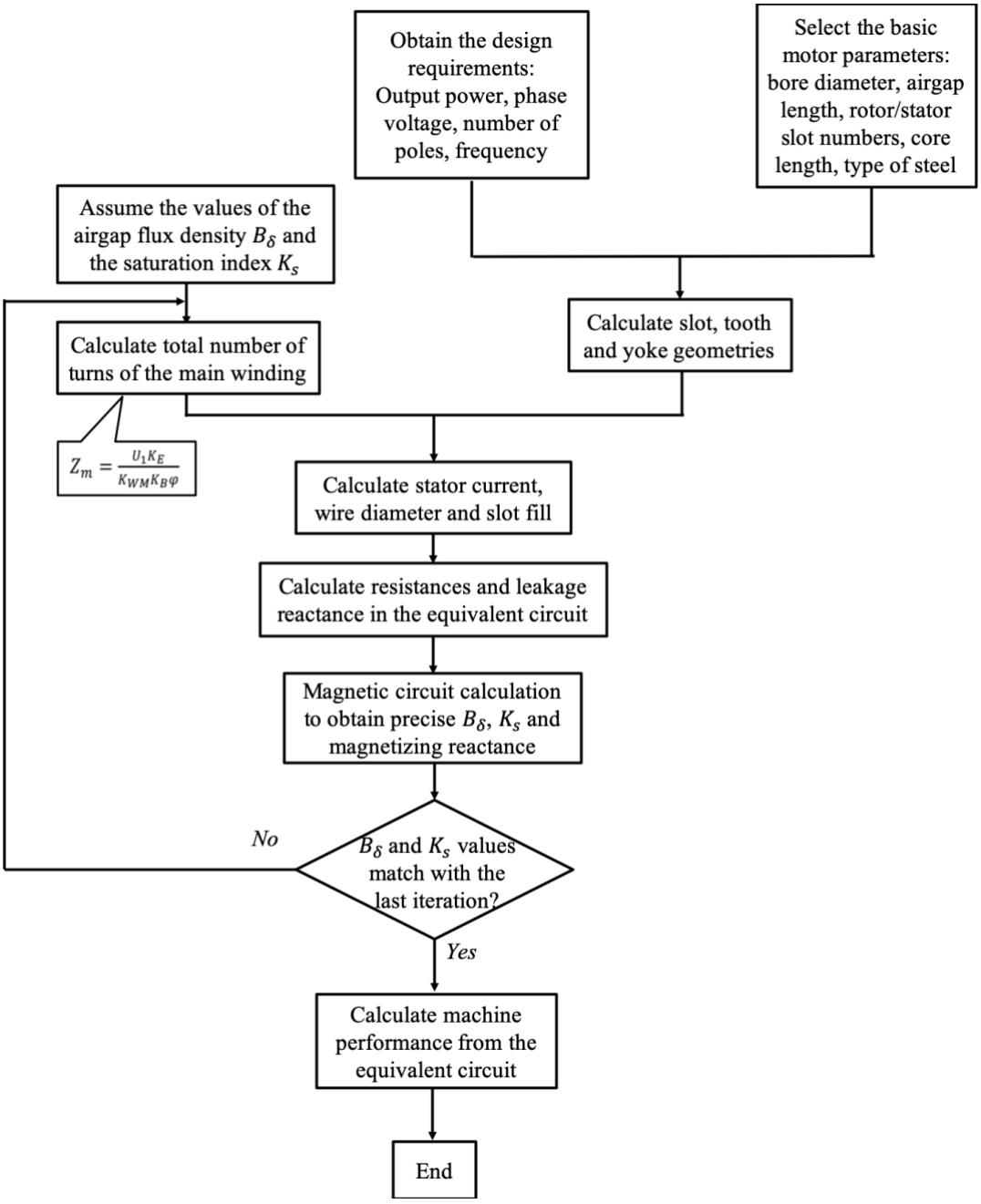

Figure 5.5 Design procedure of the single-phase IM.

Other main winding parameters such as the stator current, the wire diameter, and the slot fill can be calculated after the number of turns has been obtained. The resistances and the leakage reactance in the equivalent circuit of the main winding can thus be calculated from the main winding parameters.

The next step will be a non-linear magnetic circuit calculation, where the saturation effect is considered in order to obtain precise results. The precise B_δ and K_S values can be obtained by solving the magnetic circuit iteratively. The iteration will continue if the B_δ and K_S values calculated in the current step are having large discrepancies with the values in the last iteration, as presented by the loop in Figure 5.5. The magnetizing current and the magnetizing reactance are also calculated in this step.

After all of the parameters in the equivalent circuit have been obtained, the machine performance can be finally calculated. The PIs including the maximum torque, the rated efficiency, the rated power factor and the machine weight are chosen as the design objectives to be improved during the design optimization process.

5.3 Multi-Objective Design Optimization for Single-Phase Induction Machines

An original rough design of the capacitor-run single-phase IM can be created following the procedures presented above, which are detailed in [101]. The design objectives and the variables are then chosen for the optimization process. The particle swarm optimization (PSO) is adopted as the optimizer in order to conduct a multi-objective optimization to improve the PIs of the original machine. The objective function is defined as a weighted sum of the chosen PIs, which allows the designer the freedom to adjust the coefficients to cast more weight on one or more PIs. Two optimal designs focusing on

improving different PIs are created from the optimization process, and their PIs are then validated through FEA simulation.

5.3.1 The Original Capacitor-Run Design

The 2-D geometry of the rough design of a four-pole capacitor-run single-phase IM is presented in Figure 5.1. The rated voltage is 110V and the rated speed is 1620rpm. The main winding and the auxiliary winding are designed to be identical, marked as phase A and phase B in Figure 5.1. The windings are designed to be sinusoidal [101], so as to create a more sinusoidal magnetomotive force (MMF) in the air-gap. Consequently, the number of turns is different for each coil, and it is calculated that the coils with the coil pitch of 5 slots should have 69 turns, and the coils with the coil pitch of 3 coils should have 50 turns. The winding diagram of the machine is presented in Figure 5.6, and the design parameters are listed in Table 5.1.

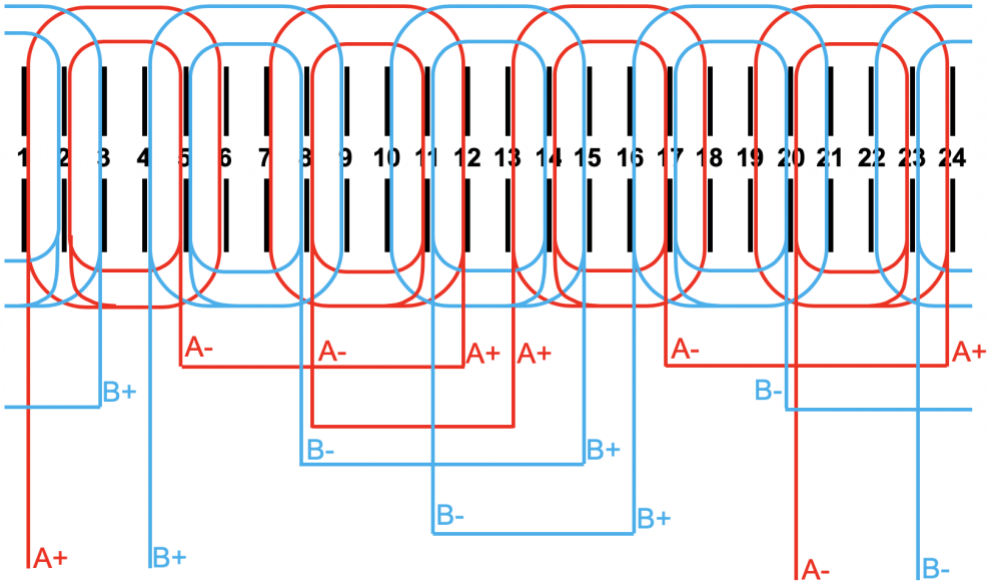

Figure 5.6 The winding diagram of the single-phase IM.

Table 5.1 Design parameters of the original single-phase IM.

Stator Parameters	Value	Rotor Parameters	Value
Stator outer diameter	117.3mm	Rotor outer diameter	69.4mm
Stator inner diameter	70.0mm	Shaft diameter	10mm
Number of stator slots	24	Number of rotor slots	34
Stator slot height	8.1mm	Rotor slot height	5.3mm
Average stator slot width	6.75mm	Average rotor slot width	2.31mm
Stator slot opening	1.9mm	Rotor slot opening	0.6mm
Rated voltage	110V	End ring height	8.5mm
Run capacitance	6μF	End ring width	3.2mm

5.3.2 Design Optimization of the Capacitor-Run Single-Phase IM

The design variables must be chosen at the very beginning of the optimization process. The outer diameter of the stator is fixed, since such parameter is usually specified in the design requirements due to the space limitation. The stator winding design and the current density are also unchanged in this research. Consequently, the stator inner diameter and rotor outer diameter are both fixed in order to not change the original saturation level of the stator and rotor yoke. The number of slots in the stator and rotor are usually chosen following the empirical combinations, thus are also not to be changed.

Based on the discussions above, the stator slot height, rotor slot height, end ring height, end ring width and the run capacitor value are chosen as the design variables, which are to be optimized in order to improve the PIs of the machine. The upper and lower limits of the design variables are listed in Table 5.2.

Table 5.2 Limits of the single-phase IM design variables.

Design Variables	**Limits**
Stator slot height	7.5mm~12mm
Rotor slot height	1mm~15mm
End ring height	5mm~10mm
End ring width	2mm~10mm
Run capacitance	3μF~40μF

The design objective is represented by a function that is the weighted sum of various machine performance indices (PIs), including maximum torque (T_{max}, in Nm), rated efficiency (*Eff*, in %), rated power factor (*pf*), and weight (*Wt*, in kilograms) at the rated working point. An example of such design objective function is shown as:

$$objective = -5 \cdot T_{max} + 10 \cdot (1 - Eff) + 5 \cdot (1 - pf) + 1 \cdot Wt \qquad (5.26)$$

The coefficients before each performance index should be chosen in such a way that each term in the objective function has approximately the same order of magnitude. Designers can also adjust these coefficients to cast more weight on one or more performance indices.

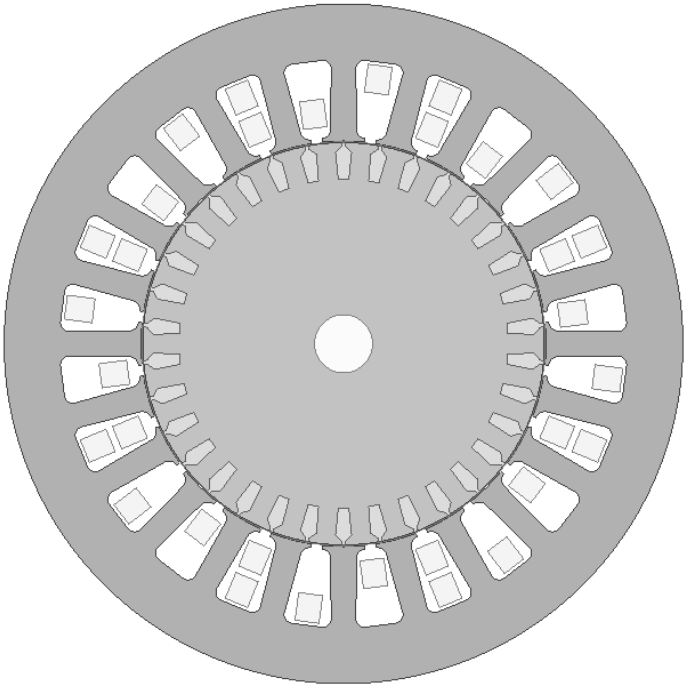

Figure 5.7 The 2-D geometry of design A.

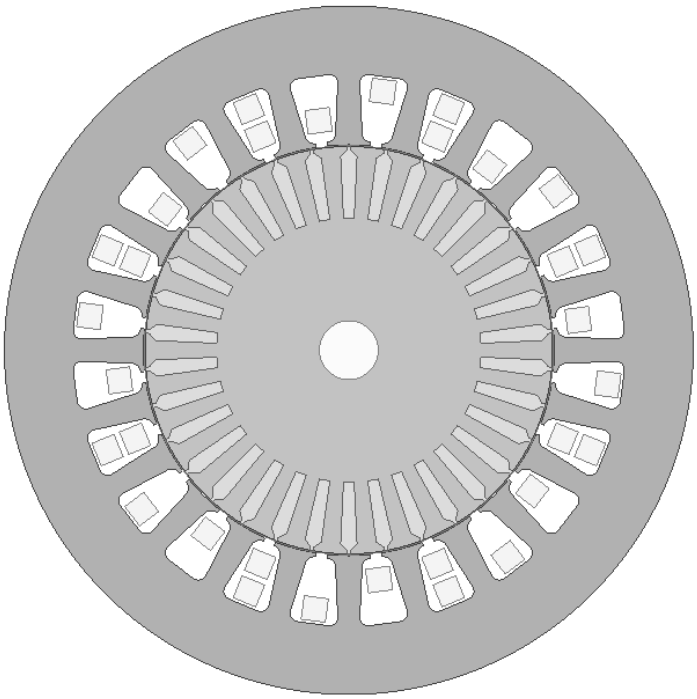

Figure 5.8 The 2-D geometry of design B.

The PSO is then performed with a swarm of 20 particles, and 30 iterations are established to yield the optimal designs. The objective function is defined as shown in (5.26), and the coefficients are adjusted in order to emphasize different PIs for each machine design. Two designs focusing on different PIs are obtained. The design A focuses more on improving the maximum torque, and design B casts more weight on improving the rated efficiency. Table 5.3 lists the values of the design variables of the two designs, compared with the original design. The calculated PIs of the three designs are also listed and compared in Table 5.3. The 2-D geometries of design A and design B are presented in Figure 5.7 and Figure 5.8 respectively.

Table 5.3 Values of the design variables and the calculated performance indices.

	Design A	**Design B**	**Original Design**
Stator slot height	10.2mm	8.2mm	8.1mm
Rotor slot height	4.6mm	10.5mm	5.3mm
End ring height	3.1mm	9.7mm	8.5mm
End ring width	5.7mm	8.8mm	3.2mm
Run capacitance	38μF	27μF	6μF
Maximum torque	1.5Nm	1.45Nm	0.92Nm
Rated efficiency	43.4%	47.5%	43.1%
Rated power factor	0.94	0.87	0.82
Weight	2.37kg	2.43kg	2.44kg

It can be observed from Table 5.3 that the maximum torque of design A is improved by 63% compared with the original design. The design B, which is expected to have improved efficiency, has an efficiency increment of 4.4% compared with the efficiency of the original design. The maximum torque of design B is also improved by 57.6% compared with the original design.

The FEA simulations are then conducted on all the three designs in order to verify the accuracy of the calculated PIs. The FEA simulation results are compared with the previously calculated values as listed in Table 5.4, whose last column presents the errors. It is shown that the analytical results are having errors of around 10% compared with the FEA simulation results, which is majorly due to the large uncertainty in core loss estimation and the working point prediction. It is also observed from the FEA results that the maximum torque of design A is improved when compared with the original design, while design B has improvements in both efficiency and maximum torque. Such improvements are the same as expected by the analytical calculations, proving the effectiveness of the proposed design optimization method.

Figure 5.9 shows the torque profiles of the three designs at their respective speeds of maximum torque. It is notable that the maximum torque PIs shown in Table 5.4 are calculated by taking the averages of the torque waveforms, and it can be seen from Figure 5.9 that both design A and design B are showing improvement on the maximum torque value compared with the original design.

Table 5.4 Comparison of the design indices calculated by the analytical model and the FEA simulations.

	PI	Analytical	FEA	Error
Original Design	Maximum torque	0.92Nm	0.85Nm	8.2%
	Rated efficiency	43.1%	52.2%	9.1%
	Rated power factor	0.82	0.74	10.8%
Design A	Maximum torque	1.5Nm	1.32Nm	13.6%
	Rated efficiency	43.4%	54.5%	11.1%
	Rated power factor	0.94	0.85	10.6%
Design B	Maximum torque	1.45Nm	1.29Nm	12.4%
	Rated efficiency	47.5%	58.3%	10.8%
	Rated power factor	0.87	0.8	8.8%

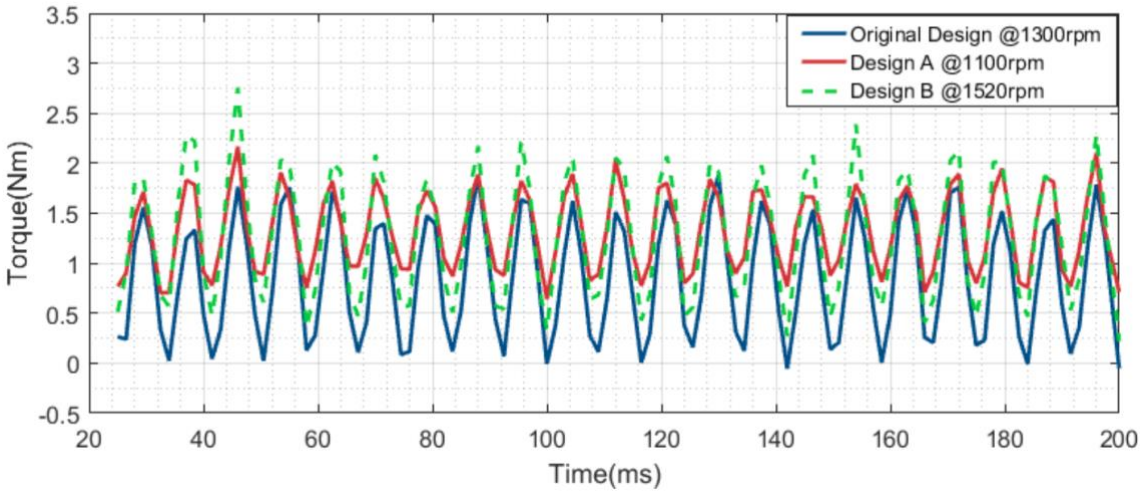

Figure 5.9 The torque profiles of the designs at their respective maximum torque working points.

It takes approximately 90 seconds to evaluate the 600 designs and generate an optimal design on the MacBook with 2.8GHz Intel Core i7 processor and 16GB memory. Such time cost can be hours or days when conducting the design optimization with FEA tools.

5.4 Chapter Summary

This chapter illustrates the design optimization process of a capacitor-run single-phase induction machine. The equivalent circuit model is adopted to analyze the single-phase IM, so that the machine performance indices can be calculated from the design parameters. The PSO algorithm is then performed with the purpose of finding the optimal design parameters in order to improve the machine performance. Such design optimization scheme saves significant amount of time compared with using FEA for finding the optimal design. FEA simulations are performed for verification at the very end to validate the optimal designs generated by the proposed procedure.

CHAPTER 6. CONCLUSIONS, CONTRIBUTIONS, AND FUTURE WORK DIRECTIONS

This chapter concludes this dissertation by summarizing the work presented in the previous chapters and showing the contributions of the concluded research. Recommendations for future work are also given in the final section of this chapter.

6.1 Conclusions

The objective of the proposed research, as stated in Section 1.2, is to develop the analytical electro-magnetic (EM) models for synchronous reluctance machines (SynRMs) and single-phase induction machines (IMs), so as to generate the optimal designs to improve their performances.

6.1.1 Analytical Model of Synchronous Reluctance Machines

It is demonstrated in this dissertation that the analytical model is a time-efficient machine design tool compared with the prevalent finite element analysis (FEA) method. Consequently, an accurate analytical model is desired for analyzing the machine performance during the design optimization process.

For the SynRM, the analytical model can be built based on either the magnetic equivalent circuit (MEC) or the Maxwell's equations. The former one is more mathematically simple while requires lots of assumptions, and the latter one has more certainty while becomes more complicated in computation. This dissertation presents an analytical model based on the Maxwell's equations in order to solve the air-gap flux density

of the SynRM. A nonlinear MEC model is also built in order to analyze the saturation effect in the machine iron. Such combination of the two modeling tools takes advantage of the accuracy of the Maxwell's equations when calculating the air-gap flux density profile, while keeps the computational complexity at the minimum level by adopting the MEC model for the saturation analysis. The nonlinear MEC model is solved iteratively and converges to the working point on the B-H curve of the iron, after which the magnetic potential on the rotor outer surface can be calculated and will be used as one of the boundary conditions for solving the potential equations. The slotted boundaries of the air-gap are simplified through conformal mapping before the potential equations can be solved and the air-gap flux density profile can be calculated.

The performance indices (PIs) of the SynRM can then be computed from the calculation results of the MEC model and the potential equations. The average torque is calculated from the magnetizing inductances of the *d* and *q* axes, which are derived from the air-gap flux densities calculated by the potential equations. The iron losses are predicted from the flux densities in the iron regions, which can be calculated from the MEC model. Calculation of the copper loss and machine weight can be conducted by straightforward analytical operations. The proposed analytical model is thus able to provide the PIs from the given design parameters of the SynRM in a time-efficient way, which is desired in the design optimization process.

The accuracy of the analytical model is verified by FEA simulations on two SynRMs with different rotor geometries. Both a SynRM with the C-shaped flux barriers and another SynRM with the circular flux barriers, able to represent most SynRM designs, are presented and analyzed through the analytical model and FEA simulations. The air-gap

flux density profiles as well as the PIs are all calculated by the analytical model, and are all showing good match with the FEA results.

6.1.2 Design Optimization of Synchronous Reluctance Machines

The evolutionary algorithms are adopted to create a fast design optimization procedure of the SynRMs based on the novel analytical model. The SynRM with C-shaped flux barriers on the rotor is chosen for optimization. Four design variables related to the geometry of the rotor flux barriers are specified as the design variables, and three PIs, including the average torque, torque density (defined as torque divided by weight) and efficiency, are chosen to be optimized during the multi-objective optimization.

Two evolutionary algorithms, the particle swarm optimization (PSO) and the differential evolution (DE), are applied as optimizers for finding the optimal designs. The optimization process should converge to the Pareto front, which consists of all the optimal designs. The performance of the two optimizers as well as the impacts of the population size and the number of iterations to the Pareto front are discussed in Section 4.3. It is concluded that the PSO algorithm with 20 particles and 30 iterations is an ideal optimizer for the proposed design optimization problem of the SynRM.

Two optimal designs of the SynRM focusing on optimizing different PIs are chosen from the Pareto front for final validation with the FEA simulations. The PIs of the two designs are calculated through the FEA method, then compared with the results calculated by the analytical model. The errors are all within the acceptable range, proving the effectiveness of the design optimization method.

Using the PSO algorithm with 20 particles and 30 iterations, the multi-objective design optimization problem can be solved in only 14 minutes and 53 seconds on a MacBook with 2.8GHz Intel Core i7 processor and 16GB memory, thanks to the proposed fast-solving analytical model of the SynRM. Such optimization process could take hours or even days if the FEA tool is applied for evaluating the 600 designs.

6.1.3 Design Optimization of Single-Phase Induction Machines

The design optimization procedure of the capacitor-run single-phase IMs is introduced in CHAPTER 5. The analytical model based on the equivalent circuits is adopted in order to calculate the PIs of the single-phase IM from the design variables. One initial design is created based on the analytical model and the past experience.

Further optimization of the original design is conducted by the PSO algorithm. Five design variables and four PIs are chosen for design optimization following the discussions in Section 5.3.2. The objective function is defined as the weighted sum of the chosen PIs, and is to be minimized through the PSO. Two different optimal single-phase IM designs focusing on improving different PIs are generated by adjusting the weights of the objective function. The FEA simulations are conducted on the original design and the two optimal designs in order to verify the accuracy of the calculated PIs. It is shown that all the errors are within the range of acceptance, and the improvement of the PIs in the two optimal designs is proved through the FEA simulations.

Such design optimization process takes approximately 90 seconds on the MacBook with 2.8GHz Intel Core i7 processor and 16GB memory, compared with hours or days when conducting the design optimization with FEA tools.

6.2 Contributions

The contributions of this dissertation are summarized as follows:

1) A novel analytical model for the SynRM is proposed. Such analytical model is majorly based on the Maxwell's equations in order to minimize the uncertainties that usually lie behind the MEC models. The complex geometry of the air-gap region is transformed into a simple shape by taking use of the conformal mapping technique, which reduces the effort needed to find the boundary conditions and solve the potential equations. Although the saturation effect is analyzed by an MEC model with the purpose of reducing the computational complexity, the proposed analytical model is still more reliable and universal compared with the MEC-based models in the literature. The proposed analytical model maintains its accuracy on the SynRMs with common flux barrier geometries including the C-shape and circular shape, and has the potential to analyze all the SynRM designs.
2) The proposed analytical model of the SynRM is able to calculate both the radial and the tangential components of the air-gap flux density vectors at any time point and any spatial position in the air-gap region. Such model thus has the potential to calculate the instantaneous torque profile of the SynRM based on the Maxwell stress tensor, which requires values of the air-gap flux density on both radial and tangential directions. As the flux lines in the air-gap region are usually assumed to be radial in the MEC models of the SynRMs, it is hard for the MEC model to calculate the amplitude of the tangential component of the air-gap flux density.

3) The two evolutionary algorithms, PSO and DE, are conducted based on the proposed analytical model of the SynRM, producing a general multi-objective design optimization method. The time consumption of such design optimization method is significantly reduced compared with the FEA-based methods, thanks to the accuracy and the time efficiency of the SynRM analytical model. Such design optimization method can be used as an effective tool at the beginning of the SynRM design process, and the optimal designs can be obtained through the proposed optimization procedure for further tuning with the FEA tool.
4) The performance of the PSO and DE algorithms in solving the SynRM design optimization problem is discussed in this dissertation. The size of population and the number of iterations are identified as two important parameters that need to be carefully chosen when applying both the two optimizers. Different combinations of the population size and the number of iterations are selected for generating the Pareto fronts, which are then compared with each other. It is concluded that the PSO algorithm with a swarm of 20 particles and 30 iterations can converge to the best Pareto front with acceptable time consumption. Such choices of the parameters can be used as the guidance and the starting point for parameter selection in order to solve other SynRM design optimization problems.
5) A design optimization procedure for the capacitor-run single-phase induction machine is proposed. Such optimization method adopts the equivalent circuit model for calculating the machine PIs from the design parameters. The objective function is configured as the weighted sum of the PIs, and the PSO

algorithm is applied for finding the optimal design. The proposed design optimization method is an excellent time saver compared with the FEA-based approaches, and is more scientific in providing the optimal design parameters, compared with the long-existing empirical design procedure of the induction machines.

6.3 Publications

The research work presented in this dissertation has resulted in several publications, listed as follows:

1) **H. Shao**, S. Li and T. G. Habetler, "Calculating the unsaturated direct and quadrature axes magnetizing inductances of synchronous reluctance machines based on Maxwell's equations and magnetic equivalent circuit," *2017 North American Power Symposium (NAPS)*, Morgantown, WV, 2017, pp. 1-6.
2) **H. Shao**, S. Li and T. G Habetler, "Analytical calculation of the air-gap flux density and magnetizing inductance of synchronous reluctance machines," *2018 IEEE Energy Conversion Congress and Exposition (ECCE)*, Portland OR, 2018, pp. 5408-5413.
3) **H. Shao**, S. Li and T. G. Habetler, "Multi-objective design optimization of synchronous reluctance machines based on the analytical model and the evolutionary algorithms," *2019 North American Power Symposium (NAPS)*, submitted.

4) **H. Shao**, S. Li and T. G. Habetler, "A general analytical model of the synchronous reluctance machines based on the Maxwell's equations and magnetic equivalent circuits," will be submitted on *IEEE Transactions*.
5) **H. Shao**, S. Li and T. G. Habetler, "Design optimization of a capacitor-run single-phase induction motor," will be submitted on *2020 IEEE Energy Conversion Congress and Exposition (ECCE)*.
6) S. Li, S. Zhang, C. Gong, **H. Shao**, G. Luo, L. He, R. G. Harley, T. G. Habetler, "An enhanced active dc-flux injection based approach for thermal monitoring of induction machines with closed-loop control schemes", will be submitted on *IEEE Transactions*.
7) C. Zhong, A. P. Sakis Meliopoulos, B. Xie, J. Xie, K. Liu, **H. Shao**, "Detailed multiphysics modeling of air-conditioned house," *2019 IEEE PES Innovative Smart Grid Technologies Conference N.A. (ISGT N.A.)*, Washington, DC, 2019, accepted.

6.4 Future Work Directions

The following directions are recommended for future research that may extend the scope of the work presented in this dissertation

6.4.1 Instantaneous Torque Calculations of Synchronous Reluctance Machines

The air-gap flux density profile of the SynRMs can be accurately calculated with the analytical model introduced in this dissertation. Such analytical model is able to calculate both the radial and the tangential magnitudes of the flux density vector in the air-gap region, which are the essential values for calculating the instantaneous torque of the

SynRM via the Maxwell stress tensors. An accurate calculation of the instantaneous torque will allow designers to analyze the torque ripple of the machine, which is an important performance index (PI) to be minimized during the machine design optimization process.

The main challenge of the instantaneous torque calculation is the precise calculation of the radial and tangential magnitudes of the flux density vector. Although the flux density values on the radial direction calculated from the proposed analytical model have been proved as accurate by comparing with FEA simulation results, it is still challenging to calculate the tangential flux density values precisely with analytical models. One possible approach to perfect the analytical calculation results is to create a larger MEC model with more vertices that represent the different geometrical locations within the SynRM. Such an MEC model would take longer to solve while increase the accuracy of the magnetic potential calculation, which will yield more accurate flux density calculation results.

6.4.2 Develop New Optimization Algorithms

The PSO and DE algorithms are adopted as optimizers in this dissertation for finding the optimal SynRM and single-phase IM designs. The two evolutionary algorithms both show good convergence speed in solving the corresponding machine design optimization problems. However, larger time consumption may occur when more design variables are introduced, and it is necessary to adopt or develop other optimization algorithms for faster convergence speed. The particle velocity calculation method in the PSO as well as the crossover and mutation rules in the DE algorithm can be modified to improve the performance of the optimizer. Performance of other evolutionary algorithms, such as the genetic algorithm (GA), can also be tested and compared with PSO and DE.

6.4.3 Additional Design Variables

The geometric parameters of the SynRMs and the single-phase IMs are chosen as the design variables in the design optimization problems presented in this dissertation. More machine design parameters such as the stator dimensions, the number of turns of the stator windings, as well as the lamination material can also be included as variables in the machine design optimization problems. Such addition of the design variables will create more complex optimization problems that take longer to converge, but would provide the designers with more freedom in adjusting the design parameters, which may lead to further performance improvement of the optimal design.

REFERENCES

[1] P. Bertoldi and B. Atanasiu, "Electricity consumption and efficiency trends in the enlarged European Union," *IES–JRC. European Union,* 2007.

[2] Y. Duan, "Method for design and optimization of surface mount permanent magnet machines and induction machines," Georgia Institute of Technology, 2010.

[3] R. Gabriel, W. Leonhard, and C. J. Nordby, "Field-oriented control of a standard ac motor using microprocessors," *IEEE transactions on industry applications,* no. 2, pp. 186-192, 1980.

[4] T. G. Habetler, F. Profumo, M. Pastorelli, and L. M. Tolbert, "Direct torque control of induction machines using space vector modulation," *IEEE Transactions on industry applications,* vol. 28, no. 5, pp. 1045-1053, 1992.

[5] J. Holtz, "Sensorless control of induction motor drives," *Proceedings of the IEEE,* vol. 90, no. 8, pp. 1359-1394, 2002.

[6] C. Gong and T. Habetler, "Constant volts per hertz control of ultra-high speed switched reluctance machines," in *IECON 2017-43rd Annual Conference of the IEEE Industrial Electronics Society*, 2017: IEEE, pp. 1868-1873.

[7] C. Gong, T. Habetler, J. Restrepo, and B. Soderholm, "Direct position control for ultra-high speed switched reluctance machines based on non-contact optical sensors," in *2017 IEEE International Electric Machines and Drives Conference (IEMDC)*, 2017: IEEE, pp. 1-6.

[8] C. Gong, S. Li, T. Habetler, J. Restrepo, and B. Soderholm, "Direct Position Control for Ultrahigh-Speed Switched-Reluctance Machines Based on Low-Cost Nonintrusive Reflective Sensors," *IEEE Transactions on Industry Applications,* vol. 55, no. 1, pp. 480-489, 2018.

[9] O. Wasynczuk *et al.*, "A maximum torque per ampere control strategy for induction motor drives," 1998.

[10] P. Chapman, S. Sudhoff, and C. Whitcomb, "Optimal current control strategies for surface-mounted permanent-magnet synchronous machine drives," *IEEE Transactions on Energy Conversion,* vol. 14, no. 4, pp. 1043-1050, 1999.

[11] D. L. Logue and P. T. Krein, "Machine efficiency optimization using ripple correlation control," in *APEC 2001. Sixteenth Annual IEEE Applied Power Electronics Conference and Exposition (Cat. No. 01CH37181)*, 2001, vol. 1: IEEE, pp. 642-648.

[12] R. Major and C. Orrock, "High saturation ternary cobalt-iron basalt alloys," *IEEE Transactions on Magnetics,* vol. 24, no. 2, pp. 1856-1858, 1988.

[13] S. Noodleman, "Method of manufacturing rare earth permanent magnet rotor," ed: Google Patents, 1976.

[14] G. Snitchler, B. Gamble, and S. S. Kalsi, "The performance of a 5 MW high temperature superconductor ship propulsion motor," *IEEE Transactions on Applied Superconductivity,* vol. 15, no. 2, pp. 2206-2209, 2005.

[15] P. Pillay and R. Krishnan, "Modeling, simulation, and analysis of permanent-magnet motor drives. II. The brushless DC motor drive," *IEEE transactions on Industry applications,* vol. 25, no. 2, pp. 274-279, 1989.

[16] S. Muller, M. Deicke, and R. W. De Doncker, "Doubly fed induction generator systems for wind turbines," *IEEE Industry applications magazine,* vol. 8, no. 3, pp. 26-33, 2002.

[17] T.-H. Liu, J.-R. Fu, and T. A. Lipo, "A strategy for improving reliability of field-oriented controlled induction motor drives," *IEEE transactions on industry applications,* vol. 29, no. 5, pp. 910-918, 1993.

[18] Y. Chin and J. Soulard, "A permanent magnet synchronous motor for traction applications of electric vehicles," in *IEEE International Electric Machines and Drives Conference, 2003. IEMDC'03.*, 2003, vol. 2: IEEE, pp. 1035-1041.

[19] T. A. Lipo, "Synchronous reluctance machines-a viable alternative for ac drives?," *Electric Machines and Power Systems,* vol. 19, no. 6, pp. 659-671, 1991.

[20] P. Lawrenson, J. Stephenson, P. Blenkinsop, J. Corda, and N. Fulton, "Variable-speed switched reluctance motors," in *IEE Proceedings B (Electric Power Applications)*, 1980, vol. 127, no. 4: IET, pp. 253-265.

[21] C. Gong, "Design and Control of Ultra-High Speed Switched Reluctance Machines over 1 Million rpm," Georgia Institute of Technology, 2019.

[22] C. Gong and T. Habetler, "A novel rotor design for ultra-high speed switched reluctance machines over 1 million rpm," in *2017 IEEE International Electric Machines and Drives Conference (IEMDC)*, 2017: IEEE, pp. 1-6.

[23] C. Gong and T. Habetler, "Electromagnetic design of an ultra-high speed switched reluctance machine over 1 million rpm," in *2017 IEEE Energy Conversion Congress and Exposition (ECCE)*, 2017: IEEE, pp. 2368-2373.

[24] C. Gong, S. Li, and T. G. Habetler, "Analysis of Rotor Robustness of Ultra-high Speed Switched Reluctance Machines over 1 Million rpm Using Cohesive Zone Model," in *2018 IEEE Energy Conversion Congress and Exposition (ECCE)*, 2018: IEEE, pp. 2401-2406.

[25] I. Boldea and S. A. Nasar, *The induction machine handbook*. CRC press, 2010.

[26] E. Castagnaro, G. Bacco, and N. Bianchi, "Rotor Iron Losses in High-Speed Synchronous Reluctance Motors," in *2018 XIII International Conference on Electrical Machines (ICEM)*, 2018: IEEE, pp. 1310-1316.

[27] J.-H. Park, J.-H. Seo, C.-H. Cha, and J. Lee, "Characteristics analysis of 15kW industrial machine using Synchronous Reluctance Motor for high efficiency," in *2013 International Conference on Electrical Machines and Systems (ICEMS)*, 2013: IEEE, pp. 139-142.

[28] J. H. Lee, "Efficiency evaluations of synchronous reluctance motor using coupled FEM and Preisach modeling," *IEEE transactions on magnetics*, vol. 39, no. 5, pp. 3271-3273, 2003.

[29] P. Niazi, H. A. Toliyat, D.-H. Cheong, and J.-C. Kim, "A low-cost and efficient permanent-magnet-assisted synchronous reluctance motor drive," *IEEE Transactions on Industry Applications*, vol. 43, no. 2, pp. 542-550, 2007.

[30] R. R. Moghaddam, F. Magnussen, and C. Sadarangani, "Novel rotor design optimization of synchronous reluctance machine for high torque density," 2012.

[31] S. J. Mun, Y. H. Cho, and J. H. Lee, "Optimum design of synchronous reluctance motors based on torque/volume using finite-element method and sequential unconstrained minimization technique," *IEEE Transactions on Magnetics*, vol. 44, no. 11, pp. 4143-4146, 2008.

[32] D. Staton, T. Miller, and S. Wood, "Maximising the saliency ratio of the synchronous reluctance motor," in *IEE Proceedings B (Electric Power Applications)*, 1993, vol. 140, no. 4: IET, pp. 249-259.

[33] K.-C. Kim, J. S. Ahn, S. H. Won, J.-P. Hong, and J. Lee, "A study on the optimal design of SynRM for the high torque and power factor," *IEEE Transactions on Magnetics*, vol. 43, no. 6, pp. 2543-2545, 2007.

[34] M. Sanada, K. Hiramoto, S. Morimoto, and Y. Takeda, "Torque ripple improvement for synchronous reluctance motor using an asymmetric flux barrier arrangement," *IEEE Transactions on Industry Applications*, vol. 40, no. 4, pp. 1076-1082, 2004.

[35] J. Tsuchiya, K. Mishima, and G. Kimura, "A study on torque ripple reduction of synchronous reluctance motor," in *4th IEEE International Conference on Power Electronics and Drive Systems. IEEE PEDS 2001-Indonesia. Proceedings (Cat. No. 01TH8594)*, 2001, vol. 2: IEEE, pp. 452-455.

[36] N. Bianchi, S. Bolognani, D. Bon, and M. Dai Pre, "Rotor flux-barrier design for torque ripple reduction in synchronous reluctance and PM-assisted synchronous reluctance motors," *IEEE Transactions on Industry Applications*, vol. 45, no. 3, pp. 921-928, 2009.

[37] N. Bianchi, S. Bolognani, D. Bon, and M. Dai Pre, "Rotor flux-barrier design for torque ripple reduction in synchronous reluctance motors," in *Conference Record of the 2006 IEEE Industry Applications Conference Forty-First IAS Annual Meeting*, 2006, vol. 3: IEEE, pp. 1193-1200.

[38] S. Li, C. Gong, L. Du, J. R. Mayor, R. G. Harley, and T. G. Habetler, "Fast calculation of the magnetic field and loss distributions in the stator core end packets and finger plates of large synchronous generators," in *2018 IEEE Energy Conversion Congress and Exposition (ECCE)*, 2018: IEEE, pp. 822-828.

[39] S. Li, C. Gong, N. A. Gallandat, J. R. Mayor, and R. G. Harley, "Implementation of surface impedance boundary conditions in the quasi three-dimensional finite-difference simulations of generator end regions," in *2017 IEEE International Electric Machines and Drives Conference (IEMDC)*, 2017: IEEE, pp. 1-7.

[40] W. Yao, J.-M. Jin, and P. T. Krein, "A highly efficient domain decomposition method applied to 3-D finite-element analysis of electromechanical and electric machine problems," *IEEE Transactions on Energy Conversion,* vol. 27, no. 4, pp. 1078-1086, 2012.

[41] P. Zhou, B. He, C. Lu, D. Lin, and N. Chen, "Transient simulation of electrical machines using time decomposition method," in *2017 IEEE International Electric Machines and Drives Conference (IEMDC)*, 2017: IEEE, pp. 1-6.

[42] D. M. Ionel and M. Popescu, "Finite-element surrogate model for electric machines with revolving field—Application to IPM motors," *IEEE Transactions on Industry Applications,* vol. 46, no. 6, pp. 2424-2433, 2010.

[43] A. Tessarolo, "Modeling and analysis of synchronous reluctance machines with circular flux barriers through conformal mapping," *IEEE Transactions on Magnetics,* vol. 51, no. 4, pp. 1-11, 2015.

[44] S. Cai, H. Hao, M.-J. Jin, and J.-X. Shen, "A simplified method to analyze synchronous reluctance machine," in *2016 IEEE Vehicle Power and Propulsion Conference (VPPC)*, 2016: IEEE, pp. 1-6.

[45] H. Mahmoud and N. Bianchi, "Eccentricity in synchronous reluctance motors—Part I: Analytical and finite-element models," *IEEE Transactions on Energy Conversion,* vol. 30, no. 2, pp. 745-753, 2015.

[46] H. Mahmoud, A. Al-Timimy, M. Degano, M. Di Nardo, N. Bianchi, and C. Gerada, "Axial eccentric SynRel and SPM motors analytical models validation using 3D finite element," in *2017 IEEE 11th International Symposium on Diagnostics for Electrical Machines, Power Electronics and Drives (SDEMPED)*, 2017: IEEE, pp. 38-44.

[47] A. Tessarolo, C. Bruzzese, M. Degano, and L. Branz, "Analytical modeling of split-phase synchronous reluctance machines," in *IECON 2014-40th Annual Conference of the IEEE Industrial Electronics Society*, 2014: IEEE, pp. 3190-3196.

[48] A. Tessarolo, M. Degano, and N. Bianchi, "On the analytical estimation of the airgap field in synchronous reluctance machine," in *2014 International Conference on Electrical Machines (ICEM)*, 2014: IEEE, pp. 239-244.

[49] H. Mahmoud, N. Bianchi, G. Bacco, and N. Chiodetto, "Nonlinear analytical computation of the magnetic field in reluctance synchronous machines," *IEEE Transactions on Industry Applications*, vol. 53, no. 6, pp. 5373-5382, 2017.

[50] H. Mahmoud and N. Bianchi, "Nonlinear analytical model of eccentric synchronous reluctance machines considering the iron saturation and slotting effect," *IEEE Transactions on Industry Applications*, vol. 53, no. 3, pp. 2007-2015, 2017.

[51] G. Bacco, N. Bianchi, and H. Mahmoud, "A nonlinear analytical model for the rapid prediction of the torque of synchronous reluctance machines," *IEEE Transactions on Energy Conversion*, vol. 33, no. 3, pp. 1539-1546, 2018.

[52] Z. Zhu and D. Howe, "Analytical prediction of the cogging torque in radial-field permanent magnet brushless motors," *IEEE transactions on magnetics*, vol. 28, no. 2, pp. 1371-1374, 1992.

[53] Z. Zhu and D. Howe, "Analytical prediction of the airgap field distribution in permanent magnet motors accounting for the effect of slotting," *COMPEL-The international journal for computation and mathematics in electrical and electronic engineering*, vol. 11, no. 1, pp. 197-200, 1992.

[54] D. Zarko, D. Ban, and T. A. Lipo, "Analytical solution for cogging torque in surface permanent-magnet motors using conformal mapping," *IEEE Transactions on Magnetics*, vol. 44, no. 1, pp. 52-65, 2008.

[55] D. Zarko, D. Ban, and T. A. Lipo, "Analytical calculation of magnetic field distribution in the slotted air gap of a surface permanent-magnet motor using complex relative air-gap permeance," *IEEE Transactions on Magnetics*, vol. 42, no. 7, pp. 1828-1837, 2006.

[56] D. Zarko, D. Ban, and T. A. Lipo, "Analytical solution for electromagnetic torque in surface permanent-magnet motors using conformal mapping," *IEEE transactions on magnetics*, vol. 45, no. 7, pp. 2943-2954, 2009.

[57] A. Radun, "Analytical calculation of the switched reluctance motor's unaligned inductance," *IEEE Transactions on Magnetics*, vol. 35, no. 6, pp. 4473-4481, 1999.

[58] A. Radun, "Analytically computing the flux linked by a switched reluctance motor phase when the stator and rotor poles overlap," *IEEE Transactions on magnetics,* vol. 36, no. 4, pp. 1996-2003, 2000.

[59] S. Li, S. Zhang, J. Dang, T. G. Habetler, and R. G. Harley, "Calculating the unsaturated inductance of 4/2 switched reluctance motors at arbitrary rotor positions based on partial differential equations of magnetic potentials," in *2015 North American Power Symposium (NAPS)*, 2015: IEEE, pp. 1-8.

[60] S. Li, S. Zhang, T. G. Habetler, and R. G. Harley, "Fast and accurate analytical calculation of the unsaturated phase inductance profile of 6/4 switched reluctance machines," in *2016 IEEE Energy Conversion Congress and Exposition (ECCE)*, 2016: IEEE, pp. 1-8.

[61] S. Li, S. Zhang, C. Gong, T. G. Habetler, and R. G. Harley, "An Enhanced Analytical Calculation of the Phase Inductance of Switched Reluctance Machines," *IEEE Transactions on Industry Applications*, vol. 55, no. 2, pp. 1392-1407, 2018.

[62] M. Yousefian, H.-R. Mosaddegh, and H. A. Zarchi, "Optimal Design of a Single-Phase Two-Value Capacitor Induction Motor With Fan Load," in *Electrical Engineering (ICEE), Iranian Conference on*, 2018: IEEE, pp. 1298-1303.

[63] K. Y. Jang, K. S. Kim, K. B. Kim, and J. Lee, "Design of premium efficiency level single induction motor by parameter analysis," in *2009 International Conference on Electrical Machines and Systems*, 2009: IEEE, pp. 1-4.

[64] M. Syatirah *et al.*, "Design and modeling of 1-phase induction motor using Opera 2D software based on copper material," in *2011 5th International Power Engineering and Optimization Conference*, 2011: IEEE, pp. 193-196.

[65] G. H. Jang and S. Park, "Characterization of a single-phase induction motor due to the effect of slot opening," *IEEE transactions on magnetics,* vol. 40, no. 4, pp. 2065-2067, 2004.

[66] Y. L. Karnavas and I. D. Chasiotis, "On the neural network single phase induction motor efficiency estimation as a design tool," in *2016 XXII International Conference on Electrical Machines (ICEM)*, 2016: IEEE, pp. 1942-1948.

[67] X. Wang, C. Zhu, R. Zhang, R. Tang, and H. Song-Yop, "Performance analysis of single-phase induction motor based on voltage source complex finite-element analysis," *IEEE transactions on magnetics*, vol. 42, no. 4, pp. 587-590, 2006.

[68] N. Tong, F. Zhang, and J. Wang, "Analysis of single-phase induction motor by using circuit-coupled finite element method," in *2008 International Conference on Electrical Machines and Systems*, 2008: IEEE, pp. 4127-4130.

[69] J. Duncan, "Linear induction motor-equivalent-circuit model," in *IEE Proceedings B-Electric Power Applications*, 1983, vol. 130, no. 1: IET, pp. 51-57.

[70] D. Lin, P. Zhou, and N. Lambert, "Starting winding optimization in single-phase induction motor design," in *The XIX International Conference on Electrical Machines-ICEM 2010*, 2010: IEEE, pp. 1-6.

[71] H. Zhong, X. Wang, D. Wang, and D. Qiao, "Analysis and Design of a New Type High-efficiency Single-phase Induction Motor Based on Negative Sequence Magnetic Field Compensation," in *2008 International Conference on Electrical Machines and Systems*, 2008: IEEE, pp. 3962-3966.

[72] H. Huang, E. Fuchs, and J. White, "Optimal placement of the run capacitor in single-phase induction motor designs," *IEEE transactions on energy conversion*, vol. 3, no. 3, pp. 647-652, 1988.

[73] R. W. Fei and J. D. Lloyd, "Design and test analysis of single-phase induction motors with 4-8 pole common winding," *IEEE Transactions on Industry Applications*, vol. 31, no. 6, pp. 1437-1440, 1995.

[74] S. Sobhani, H. Yaghobi, and M. Samakoosh, "Optimize efficiency and torque in the single-phase induction motor by adjusting the design parameters," in *2013 12th International Conference on Environment and Electrical Engineering*, 2013: IEEE, pp. 237-241.

[75] T.-U. Jung, C.-H. Yun, H.-R. Cha, M.-G. Chae, and H.-M. Kim, "Improved design for driving characteristics in single phase induction motor with concentrated winding," in *2007 IEEE Power Electronics Specialists Conference*, 2007: IEEE, pp. 2418-2422.

[76] Z. Rui, W. Qunjing, L. Guoli, P. Cong, and F. Guanghui, "Optimal design of single-phase induction motor based on MAXWELL 2D Rmxprt," in *2010 International Conference on Electrical Machines and Systems*, 2010: IEEE, pp. 1367-1370.

[77] V. Hrabovcova, L. Kalamen, P. Sekerak, and P. Rafajdus, "Determination of single phase induction motor parameters," in *SPEEDAM 2010*, 2010: IEEE, pp. 287-292.

[78] S. Abdollahi, M. Mirzaei, and H. Lesani, "Rotor optimization of a segmented reluctance synchronous motor utilizing genetic algorithm," in *2009 International Conference on Electrical Machines and Systems*, 2009: IEEE, pp. 1-4.

[79] T. Mohanarajah, J. Rizk, A. Hellany, M. Nagrial, and A. Klyavlin, "Torque Ripple Improvement in Synchronous Reluctance Machines," in *2018 2nd International Conference On Electrical Engineering (EECon)*, 2018: IEEE, pp. 44-50.

[80] Z. Li, L. Xiao, and C. Bi, "Optimization Design of a Novel Synchronous Reluctance Motor with Frequency Domain Finite Element Method," in *2018 Asia-Pacific Magnetic Recording Conference (APMRC)*, 2018: IEEE, pp. 1-2.

[81] M. E. H. Zaim, "High-speed solid rotor synchronous reluctance machine design and optimization," *IEEE Transactions on Magnetics*, vol. 45, no. 3, pp. 1796-1799, 2009.

[82] R. Constancias, I. Rasoanarivo, N. Takorabet, and F. M. Sargos, "Design and optimization of a synchronous reluctance machine with salient poles and flux barriers," in *2010 IEEE Energy Conversion Congress and Exposition*, 2010: IEEE, pp. 2672-2678.

[83] K. Tang, L. Zhou, J. Wang, Y. Xiao, and S. Wang, "Rotor design and optimization of the single-phase line-start synchronous reluctance motor," in *2017 20th International Conference on Electrical Machines and Systems (ICEMS)*, 2017: IEEE, pp. 1-4.

[84] E. Howard and M. J. Kamper, "Weighted factor multi-objective design optimisation of a reluctance synchronous machine," in *2015 IEEE International Electric Machines & Drives Conference (IEMDC)*, 2015: IEEE, pp. 1781-1789.

[85] Y. Wang, D. M. Ionel, V. Rallabandi, M. Jiang, and S. J. Stretz, "Large-scale optimization of synchronous reluctance machines using CE-FEA and differential evolution," *IEEE Transactions on Industry Applications*, vol. 52, no. 6, pp. 4699-4709, 2016.

[86] Y. S. Kim and I. H. Park, "Topology optimization of rotor in synchronous reluctance motor using level set method and shape design sensitivity," *IEEE Transactions on Applied Superconductivity*, vol. 20, no. 3, pp. 1093-1096, 2010.

[87] H. Mahmoud, M. Degano, G. Bacco, N. Bianchi, and C. Gerada, "Synchronous reluctance motor iron losses: Analytical model and optimization," in *2018 IEEE Energy Conversion Congress and Exposition (ECCE)*, 2018: IEEE, pp. 1640-1647.

[88] J.-X. Shen, S. Cai, H. Shao, and H. Hao, "Evaluation of low-cost high-performance synchronous motors for ventilation application," in *2015 International Conference on Sustainable Mobility Applications, Renewables and Technology (SMART)*, 2015: IEEE, pp. 1-6.

[89] R. H. Park, "Two-reaction theory of synchronous machines generalized method of analysis-part I," *Transactions of the American Institute of Electrical Engineers*, vol. 48, no. 3, pp. 716-727, 1929.

[90] M. Di Nardo, G. L. Calzo, M. Galea, and C. Gerada, "Design optimization of a high-speed synchronous reluctance machine," *IEEE Transactions on Industry Applications*, vol. 54, no. 1, pp. 233-243, 2018.

[91] T. Matsuo and T. A. Lipo, "Rotor design optimization of synchronous reluctance machine," *IEEE Transactions on Energy Conversion*, vol. 9, no. 2, pp. 359-365, 1994.

[92] B. Nikbakhtian, S. Talebi, P. Niazi, and H. A. Toliyat, "An analytical model for an N-flux barrier per pole permanent magnet-assisted synchronous reluctance motor," in *2009 IEEE International Electric Machines and Drives Conference*, 2009: IEEE, pp. 129-136.

[93] T. Driscoll, "Schwarz-Christoffel Toolbox Users Guide: Version 2.3, 2002," *Department of Mathematical Sciences, University of Delaware, Newark, DE*.

[94] T. A. Driscoll and L. N. Trefethen, *Schwarz-christoffel mapping*. Cambridge University Press, 2002.

[95] D. Lin, P. Zhou, W. Fu, Z. Badics, and Z. Cendes, "A dynamic core loss model for soft ferromagnetic and power ferrite materials in transient finite element analysis," *IEEE Transactions on magnetics*, vol. 40, no. 2, pp. 1318-1321, 2004.

[96] K. Wang, Z. Zhu, G. Ombach, M. Koch, S. Zhang, and J. Xu, "Optimal slot/pole and flux-barrier layer number combinations for synchronous reluctance machines," in *2013 Eighth International Conference and Exhibition on Ecological Vehicles and Renewable Energies (EVER)*, 2013: IEEE, pp. 1-8.

[97] S. Zhang, S. Li, J. Dang, R. G. Harley, and T. G. Habetler, "Multi-objective design and optimization of generalized switched reluctance machines with particle swarm intelligence," in *2016 IEEE Energy Conversion Congress and Exposition (ECCE)*, 2016: IEEE, pp. 1-7.

[98] A. Fatemi, D. M. Ionel, N. A. Demerdash, and T. W. Nehl, "Fast multi-objective cmode-type optimization of pm machines using multicore desktop computers," *IEEE Transactions on Industry Applications*, vol. 52, no. 4, pp. 2941-2950, 2016.

[99] K. Price, R. M. Storn, and J. A. Lampinen, *Differential evolution: a practical approach to global optimization*. Springer Science & Business Media, 2006.

[100] "Single Phase Induction Motors." http://www.eeeguide.com/single-phase-induction-motors/ (accessed June 19, 2019).

[101] L. Li, D. Zhu, and Y. Hu, *Principles and design of single-phase electrical machines*. Beijing: Tsinghua University Press, 1984.